

2006

## The development of an all-DNA-based electro-optic waveguide modulator

Emily Marie Heckman  
*University of Dayton*

Follow this and additional works at: [https://ecommons.udayton.edu/graduate\\_theses](https://ecommons.udayton.edu/graduate_theses)

---

### Recommended Citation

Heckman, Emily Marie, "The development of an all-DNA-based electro-optic waveguide modulator" (2006). *Graduate Theses and Dissertations*. 3227.  
[https://ecommons.udayton.edu/graduate\\_theses/3227](https://ecommons.udayton.edu/graduate_theses/3227)

This Dissertation is brought to you for free and open access by the Theses and Dissertations at eCommons. It has been accepted for inclusion in Graduate Theses and Dissertations by an authorized administrator of eCommons. For more information, please contact [mschlange1@udayton.edu](mailto:mschlange1@udayton.edu), [ecommons@udayton.edu](mailto:ecommons@udayton.edu).

THE DEVELOPMENT OF AN ALL-DNA-BASED  
ELECTRO-OPTIC WAVEGUIDE  
MODULATOR

Dissertation

Submitted to

The School of Engineering of the  
UNIVERSITY OF DAYTON

in Partial Fulfillment of the Requirements for

The Degree

Doctor of Philosophy in Electro-Optics

by

Emily Marie Heckman

UNIVERSITY OF DAYTON

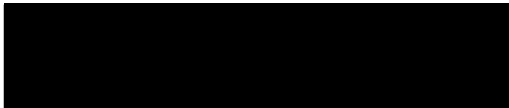
Dayton, Ohio

May 2006

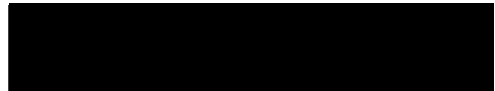
THE DEVELOPMENT OF AN ALL-DNA-BASED ELECTRO-OPTIC WAVEGUIDE  
MODULATOR

*Heckman -  
Please Do Not*

APPROVED BY:



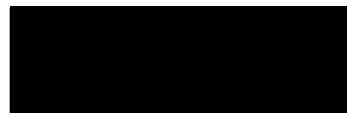
Perry P. Yaney, Ph.D.  
Advisory Committee Chairman  
Professor Emeritus, Physics  
Department and Electro-Optics  
Program



James G. Grote, Ph.D.  
Committee Member  
Senior Electronics Research  
Engineer, Air Force Research  
Laboratory



Andrew Sarangan, Ph.D.  
Committee Member  
Associate Professor, Electro-  
Optics Program



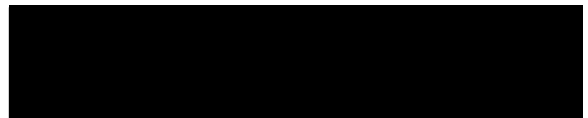
Guru Subramanyam, Ph.D.  
Committee Member  
Associate Professor, Electrical  
and Computer Engineering  
Department



Todd Smith, Ph.D.  
Committee Member  
Assistant Professor, Physics  
Department



Donald L. Moon, Ph.D.  
Associate Dean  
Graduate Engineering Programs & Research  
School of Engineering



Joseph E. Saliba, Ph.D., P.E.  
Dean, School of Engineering

Remove Old Note!

Original

100-11-100-1

© Copyright by

Emily Marie Heckman

All rights reserved

2006

## ABSTRACT

### THE DEVELOPMENT OF AN ALL-DNA-BASED ELECTRO-OPTIC WAVEGUIDE MODULATOR

Name: Heckman, Emily Marie  
University of Dayton

Advisor: Dr. Perry P. Yaney

Marine-based deoxyribonucleic acid (DNA) has been identified as a promising new biopolymer in the field of nonlinear optic materials for electro-optic, optical memory and optical amplifier applications. DNA has demonstrated low optical loss at the communications wavelengths, is an abundant and inexpensive green material, is temperature stable up to 200 °C, and has a unique double helical structure that may aid in chromophore alignment for poled polymer applications. The DNA is purified from salmon roe and milt sacs, waste products of the Japanese fishing industry. To be compatible with photonics applications, the water soluble DNA is precipitated with a surfactant complex, cetyltrimethyl-ammonium chloride (CTMA), to form a water insoluble complex, DNA-CTMA, for application as a nonlinear optical material. Several novel processes have been developed specifically for using this biopolymer in photonics applications.

In order to fabricate an all-DNA-CTMA waveguide (using DNA-CTMA for both the core and cladding layers), it is necessary to crosslink the DNA-CTMA films.

Crosslinking makes the films resistant to their initial solvent; this permits spin-coating of successive DNA-CTMA layers without solvent damage. A chromophore dye is added to the core layer to allow for an electro-optic coefficient to be induced through contact poling. The dye also provides the index of refraction difference between the core and cladding layers to meet waveguiding conditions. Through contact poling, an electro-optic (EO) coefficient comparable to that in other polymers was demonstrated in crosslinked DNA-CTMA films with the chromophore dye Disperse Red 1. This EO effect allows for the creation of an all-DNA EO waveguide modulator.

DNA was successfully developed into a useful polymer material for application in an all-DNA-based EO waveguide modulator. This research demonstrated several *firsts* with this material: the *first* example of a poled DNA-based chromophore film was demonstrated, the *first* three-layer all-DNA-based waveguide was demonstrated, and the *first* three-layer all-DNA based EO modulating device was demonstrated. Additionally, many unique processing and fabrication techniques were developed specifically for integration of DNA into a photonics device. This research demonstrates that the DNA-based biopolymer can successfully be integrated into photonics applications.

For Alex and Perry  
Two men without whom this work would not be possible

And Vivian  
Who always believed in me



## ACKNOWLEDGMENTS

There are so many people who have contributed to this work that I know I cannot hope to thank them all; however, I will try! First and foremost I must profusely thank my advisor, mentor, and dear friend, Dr. Perry Yaney. Truly a rare breed, a physicist jack-of-all trades, I feel honored to have had the opportunity to work with and learn from this exceptional scientist. Together we have persevered through problems and challenges too numerous to count.

I must also thank my research advisor at AFRL/MLPS, Dr. Jim Grote, for his guidance and support. Jim had the vision to foresee a future of DNA-based photonics and the determination to make it possible. Thanks also go to my committee members, Dr. Andrew Sarangan, Dr. Guru Subramanyam and Dr. Todd Smith, if for no other reason than actually reading my entire dissertation!

I would like to thank Dr. Melanie Tomczak and Ms. Sharon Jones of AFRL/MLPJ for their expertise and vast knowledge of molecular biology protocols. Thanks also go to Dr. Mike Durstock of AFRL/MLBP for his help with the thermal characterization of DNA. Special thanks go to Mr. Gerry Landis, Mr. Dan Shallenberger and Mr. Steve Fenstermaker of the University of Dayton Research Institute for their technical assistance. I would also like to thank Antonio Davis, Joshua Hagen and Carrie Bartsch, fellow graduate students that helped share the load and lighten the burden.

I would like to thank Dr. Naoya Ogata of the Chitose Institute of Science and Technology (CIST) for making the DNA material available, and Dr. Amane Watanuki for her technical expertise. I would like to gratefully acknowledge the support of the Air Force Research Laboratory, Materials and Manufacturing Directorate (AFRL/ML), the Asian Office of Advanced Research and Development (AOARD), the Dayton Area Graduate Studies Institute (DAGSI), Anteon Corporation, and the National Science Foundation (NSF).

Finally, I would like to thank my friends and family for their unwavering support, even when they didn't fully understand what it was I was doing. To my parents Vivian and Steve K. and Steve L., to my grandmothers Pauline and Joan, to my grandfather Ed, to my brothers and sisters, and to my in-laws, thank you. And above all, I must thank my best friend, my support, my everything, my husband. To Alex.

## DISSERTATION OVERVIEW

Chapter	Overview	Published Papers	Conference Presentations
<b>1 Introduction</b>	The development of an all-DNA-based electro-optic (EO) waveguide modulator for photonics applications is the objective of this work. This involves developing the DNA biopolymer into a material for optical waveguide applications and characterizing its applicable properties.	<i>Mol. Cryst. Liq. Cryst.</i> , <b>426</b> , (2005) <sup>b</sup> <i>J. Phys. Chem. B</i> , <b>108</b> (25), (2004) <sup>b</sup>	
<b>2 Background and Motivation</b>	The related research on polymers and polymer waveguide devices is reviewed and the challenges of fabricating an all-DNA-based waveguide modulator are introduced. An overview of the research tasks is presented.	<i>SPIE Proc.</i> : <b>5990</b> , (2005) <sup>b</sup> <b>5934</b> , (2005) <sup>b</sup> <b>5724</b> , (2005) <sup>b</sup>	
<b>3 Theory</b>	Overview of the theories relevant to this research, including the EO effect, EO modulators, optical waveguides, optical losses, and prism coupling.		
<b>4 DNA Processing</b>	Detailed description of the unique processing techniques required to develop DNA into a biopolymer for photonics applications.	<i>APL</i> <b>87</b> (12), (2005) <sup>a</sup>	
<b>5 DNA-CTMA Characterization</b>	Characterization of the DNA-CTMA biopolymer pertinent to the development of an all DNA-based EO waveguide modulator. These include the structure and temperature stability of the DNA-CTMA films, refractive indices, optical losses, resistivity, and dielectric constant.	<i>SPIE Proc.</i> : <b>5516</b> , (2004) <sup>a</sup> <b>6117</b> , (2006) <sup>b</sup> <i>Microwave and Opt. Tech. Lett.</i> , <b>46</b> (3), (2005) <sup>b</sup> <i>IEEE Microwave Letters</i> , <b>15</b> (4), (2005) <sup>b</sup>	<i>SPIE-GLPS</i> (2004)
<b>6 EO Coefficient Measurements</b>	Description of the poling technique and measurement of the EO coefficient. The poling results and achieved EO coefficients as a function of DNA molecular weight, crosslinker concentration and poling technique are presented.	<i>SPIE Proc.</i> <b>5934</b> , (2005) <sup>a</sup>	<i>APS-Ohio Sec.</i> (2005) <i>SPIE-Annual Meeting</i> (2005)
<b>7 All-DNA-Based EO Waveguide Modulator</b>	Development of an all-DNA-based waveguide and an all-DNA-based EO waveguide modulator. Design considerations including fabrication technique and material selection are discussed. Measurement and testing of the EO modulator and the performance of the device are discussed.	<i>SPIE Proc.</i> <b>6117</b> , (2006) <sup>a, d</sup>	<i>SPIE-Photonics West</i> (2006) <sup>d</sup> <i>SPIE-GLPS</i> (2006) <sup>c, d</sup> <i>SPIE Europe-Optics/Photonics</i> (2006) <sup>e</sup>
<b>8 Summary and Conclusions</b>	The first ever all-DNA-based three-layer waveguide and EO waveguide modulator were demonstrated.		

a) First-author publications, b) Contributing-author publications, c) Accepted for presentation,

d) Invited speaker/paper, e) Submitted for presentation

## LIST OF FIGURES

Figure 2.1. Structure of B form DNA.....	16
Figure 2.2. (a) DNA-CTMA film on glass substrate after 0.2 $\mu\text{m}$ filtration, and (b) free-standing DNA-CTMA film with no filtration.....	18
Figure 3.1. (a) Typical MZ Configuration, and (b) Push-Pull MZ Configuration.....	26
Figure 3.2. Schematic of an external MZ planar waveguide modulator.....	30
Figure 3.3. Image of two parallel beams for use in an external MZ planar waveguide modulator.....	30
Figure 3.4. Transverse EO phase modulator.....	31
Figure 3.5. Experimental set-up of Teng and Man technique for measuring the EO coefficient of a poled polymer film.....	33
Figure 3.6. Schematic of a planar slab waveguide.....	38
Figure 3.7. Illustration of geometrical relationships between the angles involved for prism coupling into a thin film using a right-angle prism.....	42
Figure 3.8. Illustration of relationship between the position of a mirror a horizontal distance $x_l$ away, with vertical height $h$ and the angle of incidence $\theta_i$ required to couple into waveguide mode $\beta_m$ .....	44
Figure 3.9. Schematic of prism coupling setup.....	46
Figure 3.10. Image of prism coupling setup with close-up of prism in the foreground....	47
Figure 3.11. Index of refraction of SF11 prism used for prism coupling.....	48
Figure 4.1. Molecular weight of DNA as a function of total sonication energy.....	52
Figure 4.2. 1 Kbp DNA ladder.....	54

Figure 4.3. A 1 Kbp DNA ladder standard is compared to a picture of the results of an agarose gel electrophoresis run.....	56
Figure 4.4. Illustration of formation of DNA-CTMA complex.....	58
Figure 4.5. Schematic of profilometer measurement technique to factor out thickness variations in glass substrate.....	62
Figure 4.6. Thickness of 200 kDa DNA-CTMA film with spinning parameters of 1000 rpm for ten seconds with a five second ramp.....	63
Figure 4.7. Thickness of 200 kDa DNA-CTMA film with spinning parameters of 1000 rpm for ten seconds with no ramp.....	63
Figure 4.8. Thickness of 5,000 kDa DNA-CTMA film with spinning parameters of 1000 rpm for ten seconds with a five second ramp.....	64
Figure 4.9. Thickness of 5,000 kDa DNA-CTMA film with spinning parameters of 1000 rpm for ten seconds with no ramp.....	64
Figure 5.1. Absorbance of DNA from CIST and Aldrich.....	73
Figure 5.2. CD spectra of DNA in water and DNA-CTMA in butanol at room temperature.....	75
Figure 5.3. Melting curves for DNA from different species.....	76
Figure 5.4. Melting curves of DNA in water and complexed DNA-CTMA in butanol...	77
Figure 5.5. Metricon index data for a DNA-CTMA film.....	80
Figure 5.6. Index of refraction with Cauchy fit of DNA-CTMA for three different molecular weights.....	81
Figure 5.7. Absorption loss spectrum of a 356 $\mu\text{m}$ thick film of noncrosslinked DNA-CTMA.....	83
Figure 5.8. Photo of the ruler used to calculate the dispersion in pixels/cm.....	85
Figure 5.9. Graph corresponding to Fig. 5.8 of the tick marks of the ruler.....	85
Figure 5.10. Noncrosslinked DNA-CTMA loss data with fit at 690 nm.....	87
Figure 5.11. Crosslinked DNA-CTMA loss data with fit at 690 nm for 10 wt% PPIF....	87

Figure 5.12. Crosslinked DNA-CTMA loss data with fit at 690 nm for 15 wt% PPIF....	88
Figure 5.13. Crosslinked DNA-CTMA loss data with fit at 690 nm for 20 wt% PPIF....	88
Figure 5.14. TGA curves for DNA specimens.....	90
Figure 5.15. DSC curves for DNA specimens.....	91
Figure 5.16. Expanded view of the electrode configuration connected for volume resistivity measurements using a guarded electrode.....	93
Figure 5.17. (a) Equivalent circuit for resistivity measurement, (b) Typical alternating polarity data.....	96
Figure 5.18. Resistivity as a function of temperature of crosslinked DNA-CTMA films with and without DR1 chromophore.....	98
Figure 5.19. Resistivity as a function of inverse temperature of crosslinked DNA-CTMA films with and without DR1.....	98
Figure 6.1. Schematic of the poling system.....	103
Figure 6.2. Image of the poling system.....	103
Figure 6.3. Sample Configuration for Poling.....	104
Figure 6.4. The Teng and Man ellipsometric technique for measuring the EO coefficient $r_{33}$ .....	109
Figure 6.5. Agarose gel result for laboratory-produced and mass-produced DNA material from CIST.....	112
Figure 6.6. Poling data profiles for selected samples.....	117
Figure 7.1. First example of an all-DNA-based three-layer waveguide.....	125
Figure 7.2. Indices of the core and cladding layers with Cauchy fit for the first all-DNA-based three layer waveguide.....	126
Figure 7.3. Eigenvalue equation plot for the TE modes of a symmetric three-layer all-DNA-based waveguide.....	128
Figure 7.4. Illustration of relationship between the position of a mirror a horizontal distance $x_l$ away, with vertical height $h$ and the angle of incidence $\theta_i$ required to couple into waveguide mode $\beta_m$ .....	128

Figure 7.5. Indices with Cauchy fit of proposed core and cladding materials for 3-layer DNA-based waveguide modulator.....	131
Figure 7.6. Schematic of 3-layer DNA-based waveguide modulator.....	132
Figure 7.7. Fundamental mode for a 3-layer symmetric waveguide.....	134
Figure 7.8. Poling profile data for 3-layer waveguide sample <i>W2</i> .....	139
Figure 7.9. Poling profile data for 3-layer waveguide sample <i>W6</i> .....	140
Figure 7.10. Poling profile data for 3-layer waveguide sample <i>W10</i> .....	141
Figure 7.11. Two beams propagating through single layer DNA film for use in Mach Zehnder external interferometer.....	143
Figure 7.12. Two beams propagating through three-layer poled DNA-based waveguide for use in Mach Zehnder external interferometer.....	144
Figure 7.13. DC modulation of an all-DNA-based EO modulator.....	150
Figure 7.14. DC modulation of an all-DNA-based EO modulator, extended view.....	150
Figure 7.15. Modulated TE signal for input elliptically polarized light for an applied 200 V dc as a function of the superimposed applied ac voltage.....	152
Figure 7.16. Modulated TE signal for input elliptically polarized light for a fixed applied 7.0 V rms ac voltage as a function of the applied dc voltage.....	153
Figure 7.17. Oscilloscope picture of ac modulation of all-DNA-based EO modulator...	153
Figure B.1. Ray paths of <i>s</i> -wave and <i>p</i> -wave within the polymer film.....	162
Figure C.1. Chemical structure of CTMA.....	171
Figure C.2. Chemical structure of DR1.....	171
Figure C.3. Chemical structure of DR13.....	171
Figure C.4. Chemical structure of PPIF.....	171
Figure. D.1. Flowchart of waveguide design considerations.....	176
Figure D.2. (a) Mode propagation and (b) power confinement of a three-layer single-mode waveguide. The core thickness is 1.0 $\mu\text{m}$ , and the index difference is 0.025.....	177

Figure D.3. (a) Mode propagation and (b) power confinement of a three-layer multi-mode waveguide. The core thickness is  $2.0\text{ }\mu\text{m}$ , and the index difference is 0.025.....178

Figure D.4. (a) Mode propagation and (b) power confinement of a three-layer multi-mode waveguide. The core thickness is  $3.8\text{ }\mu\text{m}$ , and the index difference is 0.025.....179



## LIST OF TABLES

Table 4.1. Film thickness of spin-coated DNA-CTMA films.....	68
Table 5.1. Refractive indices of various DNA-CTMA core and cladding materials.....	81
Table 5.2. Waveguide loss for varying concentrations of PPIF crosslinker in DNA-CTMA films.....	86
Table 6.1. Summary of poling results for DNA-based films.....	115
Table 6.2. Comparison of poling results between noncrosslinked and crosslinked DNA-based films.....	120
Table 6.3. EO coefficient for crosslinked films as a function of poling field.....	121
Table 6.4. EO coefficient as a function of poling technique.....	122
Table 6.5. EO coefficient as a function of crosslinker concentration.....	122
Table 7.1. Summary of waveguide modes for a 3-layer crosslinked DNA-CTMA waveguide.....	129
Table 7.2. Dimensions of selected three-layer waveguides.....	136
Table 7.3. Waveguide modes and angles of incidence for three-layer waveguides.....	142

## TABLE OF CONTENTS

ABSTRACT.....	iii
DEDICATION.....	v
ACKNOWLEDGMENTS.....	vi
DISSERTATION OVERVIEW.....	viii
LIST OF FIGURES.....	ix
LIST OF TABLES.....	xiv
CHAPTER	
1. INTRODUCTION.....	1
1.1. DNA-Derived Biopolymer for Photonics Applications.....	4
2. BACKGROUND AND MOTIVTION.....	8
2.1. Polymer EO Modulators.....	8
2.1.1. Poling.....	10
2.1.2. Fabrication.....	12
2.2. Development of DNA-Based EO Waveguide Modulator.....	13
2.2.1. Why DNA?.....	14
2.2.2. Overview of DNA.....	15
2.2.3. Optical Waveguide Quality Material.....	17
2.2.4. Poling.....	19
2.2.5. Waveguide Properties.....	20
2.2.6. Fabrication Issues.....	21
3. THEORY.....	22
3.1. The Electro-Optic Effect.....	22
3.2. Transverse Electro-Optic Modulator.....	25
3.2.1. Mach Zehnder 2D Waveguide Modulator.....	25

3.2.2. External Mach Zehnder Planar Waveguide Modulator.....	28
3.2.3. Transverse Planar Waveguide Phase Modulator.....	31
3.3. Measuring the Electro-Optic Coefficient.....	33
3.4. Waveguide Theory.....	37
3.5. Waveguide Loss.....	40
3.6. Prism Coupling.....	41
4. DNA PROCESSING.....	49
4.1. DNA Purification.....	49
4.2. Molecular Weight.....	50
4.2.1. Lowering Molecular Weight.....	51
4.2.2. Measuring Molecular Weight.....	53
4.3. Precipitation with CTMA Surfactant.....	57
4.4. Preparation of DNA-CTMA Films.....	60
4.4.1. Spin Parameters.....	60
4.4.2. Noncrosslinked DNA-CTMA Films.....	65
4.4.3. Crosslinked DNA-CTMA Films.....	66
4.4.4. DNA-CTMA-Chromophore Films.....	68
4.4.5. Thick films for Absorption Measurements.....	69
5. DNA-CTMA CHARACTERIZATION.....	71
5.1. DNA Purity.....	72
5.2. DNA-CTMA Structure.....	73
5.3. Index of Refraction.....	78
5.4. Waveguide Loss.....	82
5.4.1. Absorption Loss.....	82
5.4.2. Waveguide Loss.....	84
5.5. Thermal Studies.....	89
5.5.1. Thermogravimetric Analysis (TGA).....	90
5.5.2. Differential Scanning Calorimetry (DSC).....	91
5.6. Resistivity.....	92
5.7. Dielectric Constant.....	99
6. ELECTRO-OPTIC COEFFICIENT MEASUREMENTS.....	100
6.1. Contact Poling.....	101
6.1.1. Technique.....	101
6.1.2. DNA-Specific Poling Challenges.....	106
6.2. Measuring the Electro-Optic Coefficient.....	108
6.3. Results.....	110
6.3.1. Effect of Molecular Weight.....	111
6.3.2. Noncrosslinked DNA-CTMA films.....	115
6.3.3. Crosslinked DNA-CTMA films.....	118

6.3.4. Summary.....	123
7. ALL-DNA-BASED EO WAVEGUIDE MODULATOR.....	124
7.1. All DNA-Based Three-Layer Waveguide.....	124
7.1.1. Fabrication.....	124
7.1.2. Prism Coupling.....	126
7.2. All DNA-Based Three-Layer Waveguide Modulator Device Design.....	129
7.2.1. Core and Cladding Materials.....	129
7.2.2. Physical Dimensions.....	132
7.2.3. Fabrication.....	134
7.2.4. Poling.....	137
7.3. Device Testing.....	141
7.3.1. Prism Coupling.....	141
7.3.2. External Mach Zehnder Testing Configuration.....	142
7.3.3. Crossed Polarizer Testing Configuration.....	145
7.3.3.1. Results.....	147
7.3.4. AC Modulation.....	151
8. SUMMARY AND CONCLUSIONS.....	154
8.1. Contributions.....	154
8.2. Future Work.....	155
APPENDICES	
A. Calculations of Molar Concentration and Mole Percent.....	157
B. Measuring the EO Coefficient.....	161
C. Chemical Summary.....	170
D. Waveguide Design.....	172
BIBLIOGRAPHY.....	180

## CHAPTER 1

### INTRODUCTION

Escalating demands in the communications industry require the ability to transfer information at increasingly higher rates. Currently, inorganic crystals, specifically lithium niobate, used in electro-optic (EO) devices have been the material of choice to meet these demands. EO devices using lithium niobate, however, have several limitations: 1) they are expensive to make due to demanding fabrication requirements and difficult to incorporate into integrated optics devices, 2) they have high dielectric constants ( $\epsilon = 30$ ) which limit their bandwidth (length-bandwidth product  $\sim 7 \text{ GHz}\cdot\text{cm}$ ), 3) they have high refractive indices ( $n = 2.2$ ) which limit their coupling efficiency, and 4) they have an electro-optic (EO) coefficient limited to 30 pm/V at the communications wavelengths, which for an active device length of 1 cm, places a lower limit of 5 V on the voltage required to operate the device.<sup>1,2</sup>

In the past decade, polymeric electro-optic materials have emerged as a promising new class of materials well-suited for a broad range of applications from telecommunications to radio frequency (RF) photonics. Polymer EO materials have several distinct advantages over their inorganic counterparts: 1) they are comparatively

easy to fabricate and their flexible processing requirements allow straightforward incorporation with integrated optical systems, 2) they have relatively low dielectric constants ( $\epsilon = 3-4$ ) and therefore are capable of large bandwidths (length-bandwidth product  $>100 \text{ GHz}\cdot\text{cm}$ ), 3) they have low refractive indices ( $n = 1.6-1.7$ ) for improved coupling efficiency, and 4) they have demonstrated EO coefficients of  $>100 \text{ pm/V}$  allowing operating voltages of 1-2 V for an active device length of 1 cm.<sup>2-6</sup> Demonstrated polymer EO devices include phased array radar, laser beam steering, optical gyroscopes, ultrafast analog/digital converters, polarization dependent and independent modulation, Mach Zehnder modulators, and directional coupler modulators, to name a few.<sup>4, 7-14, 21</sup>

The key to the success of electro-active polymer devices, found in the last several years, stems from the introduction of chromophores with high molecular hyperpolarizability.<sup>2-6</sup> The polymer acts as a host material for these chromophore dyes, which have permanent electric dipole moments. The chromophores are preferentially aligned with the application of a strong electric field (typically on the order of  $100 \text{ V}/\mu\text{m}$ ) through a process known as electric field poling; this chromophore alignment is responsible for the high degree of nonlinearity within the now-poled polymer. In the past few years these chromophores have allowed polymer devices to achieve EO coefficients  $>100 \text{ pm/V}$  at the communications wavelengths and even higher values of  $>300 \text{ pm/V}$  are expected to be realized in the next few years.<sup>2-6, 15-18</sup> These high EO coefficients in turn allow for low operating voltages due to the inversely proportional relationship between the EO coefficient and the operating voltage. To date, several EO polymer devices have been demonstrated with operating voltages  $\leq 1 \text{ V}$ .<sup>3, 6, 18-21</sup> These sub-volt operating

voltages are essential for many applications in RF photonics and highly desired in other communications applications.<sup>6</sup>

Among one of the most attractive advantages of polymer devices over inorganic crystal devices is that of bandwidth. Intrinsic material bandwidths for polymers are on the order of 350 GHz due to their low and relatively frequency-independent dielectric constants and refractive indices.<sup>2-6</sup> Electro-optic polymer modulators with bandwidths as high as 113 GHz and 150 GHz have been demonstrated.<sup>15,22</sup> Another appealing advantage of polymer devices is their processability.<sup>2-6</sup> Polymer films can be prepared through spin-coating, dip-coating or a variety of other deposition methods including Molecular Beam Epitaxy (MBE) and vacuum evaporation. These methods are quick, easy, inexpensive, allow precise control of film thickness, and can be integrated with semiconductor circuitry by coating the polymer films directly on top of circuit wafers.<sup>5</sup> Organic polymer devices can also be fabricated to be conformal and flexible.<sup>5</sup>

Common polymer materials with proven success in EO poled-polymer device applications include poly(methyl methacrylate), or PMMA, and amorphous polycarbonate, or APC.<sup>5,23-25</sup> The selection of the host polymer, while important, is not nearly as crucial as that of the chromophore dye for achieving a high EO coefficient. Host polymer selection depends on several factors, which may be specific to the design considerations of the intended device. These include optical loss, glass-transition temperature, thermal stability, and index of refraction. The chromophores responsible for the high EO coefficients of >100 pm/V are not commercially available and are exclusively manufactured by research groups headed by Larry Dalton of the University of Washington.<sup>2-6</sup> These chromophores include the Cheng-Larry-Dalton, or CLD, series and

several other groups of as-yet unnamed chromophores.<sup>2-6</sup> There are several commercial EO chromophores, such as Disperse Red 1 (DR1), Disperse Red 13 (DR13), Disperse Red 19 (DR19), and Disperse Orange 25 (DO25), available from Sigma-Aldrich and other chemical supply companies.<sup>26</sup> However, these have significantly lower molecular hyperpolarizabilities than the CLDs. For example, EO coefficients of only 12-13 pm/V are typically reported for DR1/PMMA systems with a loading of 30% by weight of DR1 to PMMA at  $\lambda=1300$  nm.<sup>17,25</sup> Although the performance of these commercially available chromophores cannot compare with the CLD series made by Dalton and collaborators, they can serve as a useful standard since they are well known within the polymer community. Specifically, DR1/PMMA systems are regarded as a standard by which the performance of a poled-polymer can be judged.<sup>17,24,25</sup>

### 1.1 DNA-Derived Biopolymer for Photonics Applications

In the past five years, a promising new biopolymer, marine-based deoxyribonucleic acid (DNA), has been identified for EO polymer applications.<sup>27-42</sup> There are several reasons why DNA is being explored for application in photonics devices: 1) the DNA currently available is processed from salmon roe and milt sacs, which are waste products of the Japanese fishing industry, and are, therefore, abundant and inexpensive,<sup>27-31</sup> 2) it has a low ( $\epsilon \sim 4$ ) dielectric constant typical of many polymers and therefore has the promise of high bandwidth,<sup>32</sup> 3) many promising applications of DNA have already been demonstrated, including enhanced third harmonic generation (THG) and a strong enhancement of fluorescence emission,<sup>33,34</sup> 4) its unique double helical structure may aid in chromophore alignment in poled polymer applications,<sup>28,34</sup> 5) DNA has optical losses  $<1$  dB/cm at the communications wavelengths,<sup>29-31,35</sup> and 6) DNA



appears to be a stable material at high temperature with no visible degradation of films up to 200°C.<sup>31,35</sup> Additionally DNA is a green material, i.e. a non-fossil fuel derived material.<sup>29-31</sup>

This research focuses on integrating a DNA-based biopolymer, for the first time, as both the cladding and core layers of an EO polymer waveguide modulator. The central thesis of the work on this device is that it will seed important advances in the field of photonics research. It introduces a new, bio-derived material with many potential performance enhancements over current polymer materials. As a core EO polymer layer, the DNA was doped with the EO chromophore DR1 and poled to induce an EO coefficient. This result was the first and only known example of a poled DNA-based polymer film.<sup>35,36</sup> The first-ever all-DNA-based three-layer optical waveguide was also demonstrated. The waveguide used a DNA-based film for both cladding layers and an unpoled DNA-DR1-based film for the core layer.<sup>36</sup>

Research on using DNA as a biopolymer for photonics applications is in its infancy. One of the earliest publications suggesting possible optical applications of a bulk DNA-based film was published in 2000 by Kawabe et al. who investigated spontaneous emission in dye-doped DNA-surfactant films.<sup>34</sup> The DNA used by these researchers was derived from salmon and purchased commercially from Aldrich where the current price is ~\$400 USD per 10 grams of material. Shortly thereafter, one of Kawabe's collaborators, Naoya Ogata from the Chitose Institute of Science and Technology (CIST) in Japan, sponsored by the Air Force Office of Scientific Research Asian Office of Aerospace Research and Development, developed a proprietary method of processing large quantities (on the order of kilograms) of DNA from waste products of

the Japanese fishing industry in Chitose, Japan. The Materials and Manufacturing Directorate of the Air Force Research Laboratory at Wright-Patterson Air Force Base in Dayton, OH was one of the first to receive this newly processed DNA due to a prior relationship with CIST. Although other researchers are beginning to express an interest in this material, our group at Wright Patterson AFB and Ogata's group in Japan remain the major players in this research initiative. In fact, the research contained here constitutes a significant portion of all existing research in this field.<sup>27-42</sup>

Yet, despite its short history, DNA is already starting to make its mark in the field of photonics materials research.<sup>27-42</sup> Since our group's involvement in this research starting in 2000, we have been able to demonstrate many applications of this material, including: enhanced poling efficiency using DNA as a conductive cladding layer for poled polymer EO modulators,<sup>38,39</sup> enhanced performance of organic LEDs using DNA as an electron-blocking layer,<sup>40</sup> a poled DNA-DR1-based film,<sup>35,36</sup> an all-DNA-based waveguide,<sup>35,36</sup> and a DNA-based chemical sensor.<sup>41,42</sup>

The goal of the research contained here was to develop this exciting new biopolymer as a unique alternative to common organic polymers used in photonics applications by fabricating an all-DNA-based EO polymer waveguide modulator. This required extensive material and optical characterization of the DNA including optical loss, refractive indices, thermal properties, resistivity and dielectric properties, material hardness, and resistance to its environment. It also required the development of many additional processing techniques to make the DNA an optical waveguide quality material suitable for photonics devices. Initially, the DNA received from CIST is water-soluble, which is incompatible with fabrication requirements for photonics devices. It must be

precipitated with a surfactant, hexadecyltrimethylammonium-chloride (CTMA), to form the now water-insoluble complex DNA-CTMA. Additionally, the molecular weight of the DNA received from CIST is extremely high ( $> 5000$  kDa, 1 kiloDalton (kDa) = 1 kg/mol) which complicates many of the processing procedures. We have found it necessary to lower the molecular weight to  $<1000$  kDa to meet certain requirements of this research. Furthermore, we have found it necessary to crosslink the DNA-CTMA materials used in the layers of the waveguide to make them resistant to the initial solvents, which allows spin-coating of multiple layers. The crosslinking is done chemically through the addition of poly(phenyl isocyanate-co-formaldehyde), PPIF. A further benefit of this crosslinking is the hardening of the DNA films, which improves the mechanical properties of the films.

The primary goal of this research was to show that DNA can be integrated into an EO polymer waveguide modulator as both the core and cladding layers. A secondary goal was to evaluate its potential with respect to current polymers such as APC and PMMA; however, enhanced performance was not an issue due to the limits on the available chromophores for this work. This work demonstrated that DNA can be successfully integrated into optical applications – an application never before pursued for this material.

## CHAPTER 2

### BACKGROUND AND MOTIVATION

#### 2.1 Polymer EO Modulators

Nonlinear optical (NLO) polymer thin films hold the promise of being a low-cost, high-performance alternative to inorganic crystals currently being used in EO modulating devices.<sup>2-6</sup> As previously mentioned, polymer films are typically fabricated by spin-coating; this makes them easier and less expensive to fabricate than inorganic crystals, which must be grown in a time-intensive and costly process.<sup>5</sup> It also allows for easy integration into electronic circuitry.<sup>2-6</sup> Polymers also have low dielectric constants ( $\epsilon \sim 3$ -4) which allows for high speed ( $>100$  GHz) modulation.<sup>2-6</sup> Polymer modulators have already been demonstrated with bandwidths of up to 150 GHz.<sup>15,22</sup> Additionally, due to recent introduction of chromophore dyes with high molecular hyperpolarizability, EO coefficients  $>100$  pm/V have been demonstrated in chromophore doped polymer films.<sup>2-6</sup> This has allowed for EO modulators with operation voltages of  $\leq 1$  V.<sup>3,6,15,18-21</sup>

The initial design goal for an EO polymer modulator is to perform at a modulation rate of 100 GHz with  $\leq 1$  V input and a propagation loss of  $\leq 1$  dB/cm.<sup>2-4,43</sup> The

modulation voltage  $V_\pi$ , or half-wave voltage, required to achieve the desired  $\pi$ -phase retardation for an EO modulator is given by<sup>44,46,70</sup>

$$V_\pi = \frac{\lambda d}{n_e^3 r_{33} L} \quad (2.1)$$

where  $\lambda$  ( $\mu\text{m}$ ) is the wavelength,  $d$  ( $\mu\text{m}$ ) is the thickness of the EO material,  $n$  is the index of the EO material,  $r_{33}$  (pm/V) is the EO coefficient of the material, and  $L$  (m) is the length of the interaction region. Because  $V_\pi$  is inversely proportional to  $r_{33}$ , materials with higher EO coefficients will be capable of having lower modulation voltages. As previously mentioned, EO coefficients in polymers of  $>100$  pm/V have been achieved, but even higher coefficients of  $\sim 300$  pm/V have been predicted; allowing the modulation voltages of these devices to be reduced even more.<sup>5</sup>

The key to developing low- $V_\pi$  modulators is developing materials with high EO coefficients. This has been achieved by doping amorphous polymers with chromophores that have a high molecular hyperpolarizability and improved molecular alignment properties, and preferentially orienting them with electric field poling techniques to increase the material's nonlinearity.<sup>2-6</sup> Several different molecular design approaches are used to incorporate the molecular dipoles into the polymer matrix. In guest/host systems, the NLO dipoles are simply dissolved in the host polymer. With side-chain polymers, the NLO dipoles are chemically bonded to the backbone of the polymer, and in main-chain polymers the dipoles are part of the main polymer chain.<sup>44</sup>

Chromophore concentration is an important factor in developing a guest/host poled polymer film. The limited solubility of the dye dipoles in the polymer matrix restricts the concentration of dipoles that can be incorporated into the polymer matrix.<sup>44</sup>

Additionally, high chromophore concentration is limited by dipole-dipole interactions that make it impossible to achieve a high degree of noncentrosymmetric order.<sup>3</sup> Recently, new chromophores have been engineered that overcome this limitation, allowing higher concentrations of dipoles and achieving higher EO coefficients ( $r_{33} > 100$  pm/V).<sup>2-6,15</sup>

Although the results achieved thus far with polymers are impressive, there are still several areas which require improvement. To be competitive, polymer materials must meet or beat the current standards set forth by lithium niobate.<sup>2</sup> As previously mentioned, a large EO coefficient on the order of 100 pm/V is required to achieve a modulation voltage  $\leq 1$  V. This high EO coefficient typically requires a high concentration of chromophore dye.<sup>2-6</sup> Inevitably, these polymers designed with higher EO coefficients, i.e. with higher concentrations of chromophores, may have increased optical loss due to the absorption and scattering by the chromophores.<sup>45</sup> To be competitive with lithium niobate, total polymer waveguide loss (loss due to scattering and absorption) should be  $\leq 1$  dB/cm.<sup>2,4</sup> Increased optical loss can limit the interaction length (electrode length), which in turn increases the drive voltage,  $V_\pi$ . Thus, the trade-offs between bandwidth, optical loss, and drive voltage must be considered.<sup>2</sup> Other areas that must be simultaneously considered for poled polymers are the thermal and temporal stability of both the polymer and the chromophore alignment.<sup>2-6</sup>

### **2.1.1 Poling**

Poling, as used here, refers to the process of preferentially orienting “guest” molecular dipoles (chromophores) within a “host” polymer by an applied electric field to introduce optical nonlinearity in the material. The degree of this nonlinearity is

characterized by the EO coefficient. When an amorphous polymer film containing dipolar species (chromophores) is heated to a sufficiently high temperature (typically just below the glass transition temperature,  $T_g$ ) and subjected to a strong electric field ( $\sim 1\text{MV/cm}$ ), the average orientation of the dipolar species is perturbed and a polar axis (parallel to the direction of poling) is induced.<sup>44,46</sup> This is an infinite rotational axis with an infinite number of mirror planes. The molecules are distributed cylindrically about the z-axis, which are frozen in place after cooling while the field is applied, giving a symmetry that is similar to that of a monoclinic system.

There are several methods of poling including contact poling, corona poling, photothermal poling and photoinduced poling.<sup>44</sup> Contact and corona poling are the two most popular poling methods for poling thin films perpendicular to the film plane. Proponents of corona poling argue that there is less chance of catastrophic breakdown in the film, while proponents of contact poling point out that with corona poling the precise poling field is unknown and that crashing of corona ions on the exposed film surface can cause damage to the film.<sup>47</sup> Contact poling uses electrodes to directly apply an electric field to the doped polymer material that has been heated to just below  $T_g$ . Compared to corona poling, contact poling uses a lower poling voltage, offers precise control of the poling voltage, allows a selective poling area, and provides a uniform poling voltage and therefore better film quality.<sup>25</sup> For these reasons and its ease of implementation, contact poling was the method used in this research.

Poling is an extensively researched process and many references on poling techniques and results are available.<sup>48-57</sup> In principle poling is a straight-forward process; however, in practice, there are subtle issues that can affect poling efficiency. One

unresolved issue in the poling community is whether to apply the temperature first and then the field, as is the traditional method, or to apply them in the reverse order. There have been several groups who have investigated this issue with no clear consensus reached.<sup>24,46,47,58</sup> The heating and cooling rates of the polymer as well as the dwelling time at the poling temperature can also affect poling efficiency.<sup>24</sup>

For an actual waveguide device, the polymer core material is poled between two cladding layers in a three-layer structure. The addition of the cladding layers can dramatically reduce the poling efficiency if the resistivities of the cladding layers are higher than that of the polymer core layer.<sup>47,59</sup> For a symmetric three-layer waveguide, the voltage applied across the core,  $V_{core}$ , due to the total applied voltage across the stack,  $V_{app}$ , depends on the resistivities of the core and cladding,  $\rho_{core}$  and  $\rho_{clad}$ , according to

$$V_{core} = V_{app} \frac{1}{1 + 2(\rho_{clad} / \rho_{core})(d_{clad} / d_{core})} \quad (2.2)$$

where  $d_{core}$  and  $d_{clad}$  are the corresponding thicknesses of the symmetrical waveguide core and cladding layers, respectively.<sup>47,59</sup> For equal thicknesses of the layers and  $\rho_{core} \geq 20 \rho_{clad}$ , then >90% of the applied voltage appears across the core polymer region. The EO coefficient of a polymer thin film is measured using a straight-forward ellipsometric technique, which is described in detail in Sec. 3.3.

### 2.1.2 Fabrication

A major challenge in developing a three-layer polymer waveguide stack is sequentially spinning the multiple layers (core and cladding). The first effort is to search for suitable cladding and core materials that have mutually exclusive solvents, thereby allowing each layer to be spin coated directly on top of the preceding layer. If this cannot



be done, a common technique is to apply a buffer or passivation layer to the first layer (e.g., bottom cladding) to protect the first layer from the solvent used in the second (e.g., core) layer.<sup>60,61</sup>

There are many other fabrication issues in developing a three-layer polymer EO modulator. Spin parameters must be determined that yield films of a uniform thickness of a desired value (typically 2-4  $\mu\text{m}$ ). Additionally, to provide confinement of the light in both the horizontal and vertical directions, a channel waveguide must be fabricated in the core region. Several different techniques have been reported that provide successful fabrication of channel polymer waveguides. Typically, a mask outlining a channel waveguide is produced using photolithography. Then reactive ion etching (RIE) or photobleaching is used to fabricate the channel structure.<sup>62</sup> The fabrication of a channel waveguide using a laser ablation technique that uses conventional photolithography techniques to form the channel pattern and then uses ablation until the bottom buffer layer is exposed has also been reported.<sup>60</sup> Another technique uses simultaneous direct laser writing and electric poling of arbitrary channel waveguides that have EO properties.<sup>63</sup>

## **2.2 Development of a DNA-Based EO Waveguide Modulator**

The term deoxyribonucleic acid, or DNA, almost immediately invokes the image of the fundamental building blocks of nature, the blueprint for all organic life. The simplest definition of DNA, however, is that of a polymer: a long molecule of repeated subunits. In the case of DNA, these subunits are the nucleotides adenine, guanine, cytosine, and thymine. Extracting DNA from its natural state and removing all extraneous proteins leaves the remaining DNA as an organic polymer chain not unlike

other organic polymers being used in a variety of scientific and technical applications. Recognizing this identity of DNA as a polymer chain has led us to pursue the development of a DNA-based biopolymer for optical waveguide applications.

The primary goal of this research was to develop DNA as a biopolymer for application in an all-DNA-based EO waveguide modulator. This consists of using the DNA material as the basis for the core and cladding materials for the optical waveguide layers. It is a *DNA-based* design and not a *DNA-only* design, because it was found that purified DNA alone is not a suitable material for optical waveguide fabrication.<sup>27,34</sup> DNA is initially water-soluble, which is incompatible with optical device fabrication. It is, therefore, necessary to precipitate it at a 1:1 molar ratio with a cationic surfactant, hexadecyltrimethylammonium-chloride (CTMA), to make it water-insoluble. Additionally, we have determined the need to crosslink the DNA-CTMA material with the chemical poly(phenyl isocyanate-co-formaldehyde), PPIF. Crosslinking was required to make the material insoluble to the initial solvents, thereby allowing spin-coating of multiple layers. It also renders a significantly harder and more durable film than noncrosslinked DNA-CTMA and is better able to withstand demanding fabrication requirements.

The following sections present a brief overview of DNA and the progression of this research for the development of an all-DNA-based optical waveguide device.

### **2.2.1 Why DNA?**

In Hokkaido, Japan, over 200,000 tons of salmon is fished each year, from which 15,000 tons of waste products in the form of the salmon roe and milt sacs are discarded. With support from the Air Force Office of Scientific Research Asian Office of Aerospace

Research and Development, the Chitose Institute of Science and Technology (CIST) in Hokkaido has developed a process for purifying this waste on a large scale into a material that can be used for optical applications.<sup>27</sup> This has created an abundant and inexpensive resource of relatively pure DNA. Early research on this material has indicated that it may be well-suited for photonics applications: DNA provides a strong enhancement of fluorescence over other polymers when doped with hemicyanine dyes;<sup>34</sup> nonlinear optical (NLO) chromophore dyes show an increased binding to the DNA biopolymer;<sup>41</sup> the DNA has high thermal stability;<sup>35</sup> amplified stimulated emission has been observed from dye-doped DNA,<sup>27</sup> and it has been shown that the DNA double helix may provide enhanced alignment when doped with NLO dyes.<sup>27</sup>

In addition to the potential for enhanced performance over other polymer materials, DNA is an attractive material because it is a green, non-fossil fuel-based material. Moreover, DNA can be found in every living organism on Earth and could also potentially be processed from plant waste products in addition to marine waste products. DNA holds the potential to become an inexpensive, non-fossil fuel-based alternative to current polymers used in photonics applications.

### **2.2.2 Overview of DNA**

In 1868, a substance called *nuclein*, considered to be characteristic to the nucleus of a cell, was isolated from the nucleus of pus cells by Friederich Miescher.<sup>64</sup> This substance was later shown to be a mixture of a basic protein and a phosphorous-containing organic acid, now called *nucleic acid*. The major nucleic acid in the nucleus of cells is *deoxyribonucleic acid* (DNA). DNA is a polymer with repeating subunits of nucleotides (thymine, cytosine, adenine, and guanine). In the DNA structure, strands of

adenine are paired to strands of thymine, and strands of guanine are paired to strands of cytosine in what is known as base pairing. The ratio of adenine and thymine pairs to guanine and cytosine is nearly unity.<sup>64</sup> These base pairs form the rungs in the DNA-double helix ladder structure and hydrogen bonds form between the opposing bases within a pair. Watson and Crick were the first to incorporate a model for DNA base pairing between complementary strands in 1953. As seen in Fig. 2.1, the spacing between each base pair is 0.34 nm. In the most common form of the DNA double helix, the B form, there is one complete twist of the helix every 10 base pairs, or every 3.4 nm.<sup>64</sup>

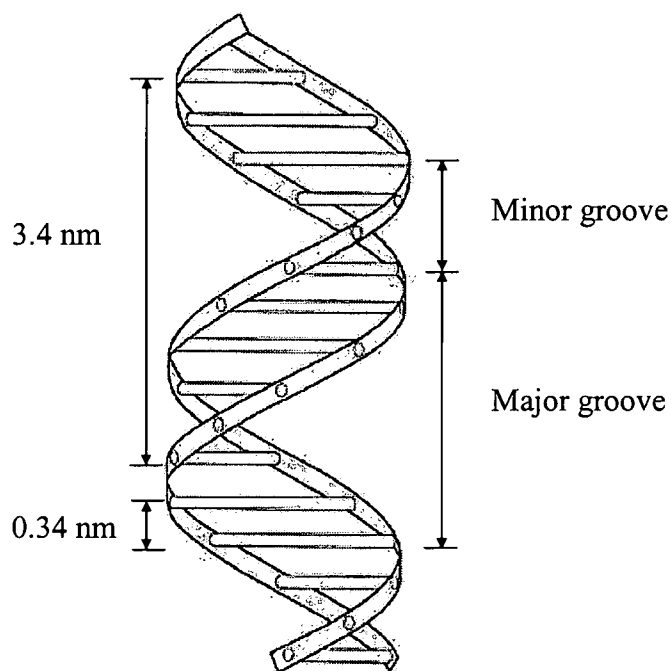


Fig. 2.1. Structure of B form DNA. [From Reference No. 64]

Because the DNA double helix is a relatively long molecule ( $\sim 4 \mu\text{m}$  long for a 12,000 base pair strand), it has a high viscosity in solution. As a DNA solution is heated to  $\sim 95^\circ\text{C}$ , its viscosity markedly drops due to the collapse of the double helix structure.<sup>64</sup> This collapse, known as denaturation, is accompanied by separation of the duplex into its single strands. Upon cooling, these strands will recombine to form the double stranded helix once again; this is referred to as renaturation. The molecular weight of DNA per base pair is  $\sim 660 \text{ g/mol/base pair (bp)}$ , or  $660 \text{ Dalton/bp (Da bp}^{-1}\text{)}$ .<sup>65</sup>

### ***2.2.3 Optical Waveguide Quality Material***

The first task of this research was to process the DNA into an optical material compatible with optical waveguide device fabrication. The primary fabrication issue for DNA is the determination of the processing needed to make an optical waveguide quality film of suitable hardness that is resistant to the cladding solvents and insensitive to humidity. Early batches of DNA obtained from CIST had a measured molecular weight of the purified DNA of  $\text{MW} = 6500 \text{ kDa}$  with a purity measured assay of 96% and a measured protein content of 2%. Initially, the DNA is soluble only in water, which is clearly incompatible with optical waveguide fabrication. The DNA was precipitated with a surfactant, CTMA, through an ion exchange reaction that replaces the sodium cation of the DNA.<sup>31,33</sup> The resulting DNA-CTMA complex is water insoluble and more mechanically stable due to the long alkyl chain of the CTMA. This complex is soluble in ethanol, methanol, butanol or a chloroform/alcohol blend, making it more compatible with device fabrication.

To create an optical waveguide quality DNA-CTMA film, the DNA-CTMA is dissolved in butanol and filtered through a  $0.2 \mu\text{m}$  filter to remove any particulates. The

filtered solution is spin-coated onto a substrate to achieve an optical quality film for waveguide purposes. Filtering provides a great enhancement in optical clarity by removing microscopic debris. Figure 2.2 shows a qualitative comparison between two DNA-CTMA films, one made with filtered DNA-CTMA and one made with unfiltered DNA-CTMA.

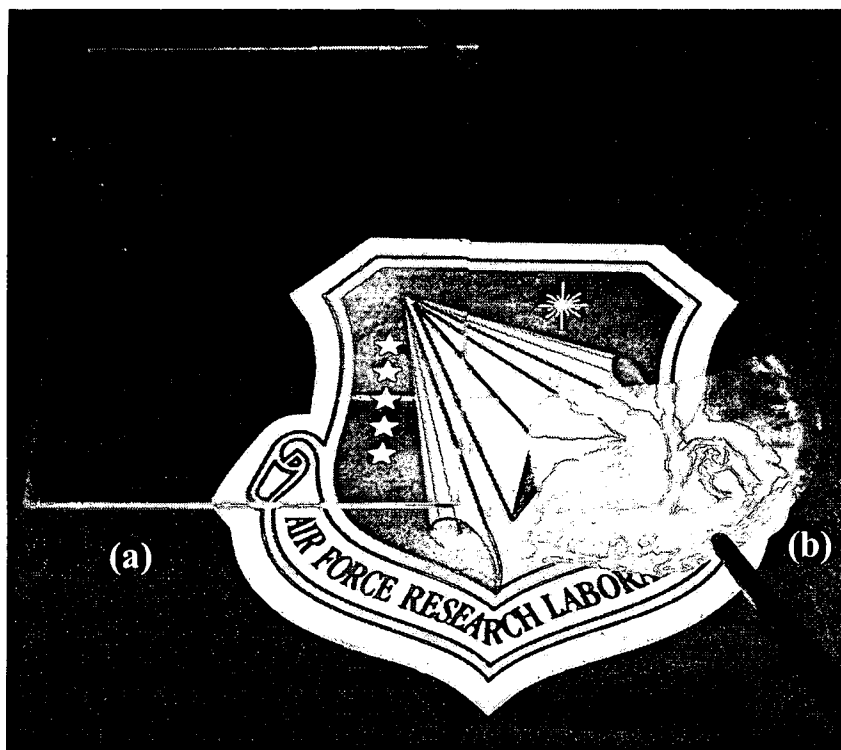


Fig 2.2. (a) DNA-CTMA film on glass substrate after 0.2  $\mu\text{m}$  filtration, and (b) free-standing DNA-CTMA film with no filtration.

### 2.2.4 Poling DNA Films

The next goal of this research was to achieve the highest possible degree of nonlinearity through electric field poling. Our prior research had already demonstrated that a single film layer of DNA-CTMA-DR1 can be successfully poled.<sup>35</sup> A 60 V/ $\mu\text{m}$  field was applied at a poling temperature of 60°C in a nitrogen environment to a DNA-CTMA film with 8 wt% DR1. The EO coefficient was measured to be  $r_{33} = 2.8$  pm/V at 633 nm using an ellipsometric technique. This is comparable to that of DR1 in PMMA, where for a similar loading results of 3-4 pm/V have been reported.<sup>24</sup>

Because DNA is such a unique material, it presents special poling challenges not seen with other polymers. A clear  $T_g$  could not be measured for DNA using differential scanning calorimetry (DSC); therefore, standard poling procedures do not directly apply to DNA. Another challenge DNA presents is its apparent susceptibility to water adsorption. Although the DNA-CTMA film is water insoluble, it is still vulnerable to slight water adsorption from the atmosphere. This water adsorption appears to be the cause of recurrent shorts during poling. Additionally, DNA is a unique material in that it can have a wide variety of molecular weights. Thus, the effect of molecular weight on the poling process had to be explored.

The DNA-CTMA-chromophore films were poled using contact poling. The electrodes used are transparent indium tin oxide (ITO) on the bottom and gold on the top. The poling station was nitrogen purged to ensure an inert atmosphere for poling. The EO coefficient was measured using the ellipsometric technique developed by Teng and Man.<sup>66-68</sup>

Several factors were involved in optimizing the poling process to achieve the highest possible EO coefficient. In addition to varying the poling parameters such as temperature, voltage and poling duration, the chromophore concentration in the DNA-CTMA film had to be optimized. The addition of cladding layers presented another challenge in poling. Although the cladding layers should aid in reducing the number of shorts by providing buffer layers, as discussed in Sec. 2.1.1, relatively high resistivity of the cladding layers can reduce the poling efficiency.<sup>47,59</sup> The resistivity for each waveguide layer will be measured using an alternating polarity technique described in detail in Sec. 5.6.

#### ***2.2.5 Waveguide Properties***

In developing DNA as both a core and cladding polymer waveguide material, there were optical, electrical and fabrication issues that required thorough investigation. The needed optical waveguide properties include the indices of refraction and optical waveguide losses. The index of the core layer must be higher than that of the cladding layer to support a guided wave (Sec. 3.4). It was found that the addition of the chromophore dye raises the index of the core layer by an amount suitable to meet waveguiding requirements. As different films of DNA-CTMA were fabricated with variations in crosslinker and chromophore concentration, the indices of refraction were measured using a Metricon 2010 wave-coupling instrument (Sec. 5.3).

Optical spectrophotometer measurements provided the necessary preliminary data needed to evaluate the performance of the material in waveguide applications. The optical transmission spectra for the various DNA-CTMA films (crosslinked, noncrosslinked, doped, undoped) were measured to obtain the minimum possible losses



at the communications wavelengths of 800 nm, 1300 nm, and 1550 nm. For waveguide applications, total losses  $\leq 1$  dB/cm are typically desired.<sup>2,4</sup>

The optical transmission spectra for various films of DNA-CTMA with different chromophore and/or crosslinker concentrations were measured with a Hitachi 4001 spectrophotometer. Although these results are not the final loss of the waveguide itself, a transmission loss measurement provides a measure of the minimum loss that can be expected when the material is integrated into a waveguide device. The overall optical loss of the waveguide was measured once the waveguide fabrication was complete. This process involved coupling light into a finished planar, one-dimensional waveguide and measuring the rate of decay of the propagating light versus distance.

#### ***2.2.6 Fabrication Issues***

The primary fabrication issue to overcome was how to spin multiple DNA-based layers on top of each other without the solvent attacking the previous layer. The chemical PPIF was used to crosslink the material, which then made the crosslinked DNA-CTMA layers resistant to the initial solvents. The crosslinker, PPIF, has the additional benefit of hardening the DNA-CTMA film. For most device applications, fabricating an NLO polymer device requires that the polymer layer withstand standard cutting and polishing procedures. DNA-CTMA is a very soft material, which is damaged by these procedures. A fingernail scratched lightly across the surface, for example, leaves a mark. A DNA-CTMA film crosslinked with PPIF is significantly harder than a noncrosslinked film. A fingernail scratched lightly on the surface of a crosslinked DNA-CTMA film does not leave a mark. Crosslinking of DNA-CTMA films is discussed in greater detail in Sec. 4.4.3.

## CHAPTER 3

### THEORY

#### 3.1 Electro-Optic Effect

The electro-optic (EO) effect, also known as the Pockels effect, refers to a change in the refractive index of a material due to an applied DC electric field. In certain materials, this change can be significant and can be used to change the relative phases of a wave propagating in the material. The polarization  $\mathbf{P}$  of a linear, isotropic dielectric medium by an electric field  $\mathbf{E}$  can be expressed as

$$\mathbf{P} = \epsilon_0 \tilde{\chi} \mathbf{E} \quad (3.1)$$

where  $\epsilon_0$  is the vacuum permittivity and  $\tilde{\chi}$  is the susceptibility. The susceptibility is a tensor quantity and can be expressed by the power series

$$\tilde{\chi} = \chi_0 + \tilde{\chi}_1 \mathbf{E} + \tilde{\chi}_2 \mathbf{E}^2 + \dots \quad (3.2)$$

For many materials, the higher order terms of the susceptibility are negligible. A meaningful effect in the first order term is produced by the presence of an effective dipolar distribution in the solid. For crystals, such as lithium niobate, this is due to the strong axial symmetry of the crystal structure, and in polymers, it is due to the alignment of the dipolar dye molecules.

Substituting the nonlinear susceptibility Eq. (3.2) into Eq. (3.1) gives

$$\mathbf{P} = \varepsilon_0 (\chi_0 \mathbf{E} + \tilde{\chi}_1 \mathbf{E}^2 + \tilde{\chi}_2 \mathbf{E}^3 + \dots) \quad (3.3)$$

where the first term represents the linear polarization, and the higher order terms are the nonlinear polarization tensor terms. These higher order terms in the polarization give rise to higher order terms in the index of refraction<sup>69</sup>

$$\frac{1}{n^2} = \frac{1}{n_o^2} + \tilde{r} \mathbf{E} + \tilde{R} \mathbf{E}^2 \quad (3.4)$$

where  $\tilde{r}$  and  $\tilde{R}$  are the linear and quadratic electro-optic coefficient tensors, respectively, and  $n_o$  is the weak-field refractive index. The Pockels effect results from the linear term in Eq. (3.4), where the applied field  $\mathbf{E}$  is a DC field.

Generalizing Eq. (3.4), the change in the index of refraction due to the linear electro-optic effect is given by the equation<sup>70</sup>

$$\Delta \left( \frac{1}{n_{ij}^2} \right) = \sum_{k=1}^3 r_{ijk} E_k \quad (3.5)$$

where  $n_{ij}$  is the index of refraction,  $r_{ijk}$  is the EO coefficient (an element of the electro-optic tensor  $\tilde{r}$ ), and  $E_k$  is the component of the applied electric field. The EO coefficient tensor  $\tilde{r}$  is a third-rank tensor whose elements can be expressed in contracted notation ( $r_{ijk} = r_{ak}$ ) when permutation symmetry is present, as it is for poled polymers. In a poled polymer, the axis parallel to the poling direction (the  $z$ -axis) is an infinite rotational axis with an infinite number of mirror planes. In the absence of an applied field, there will be an index of refraction  $n_e$  in the  $z$ -direction, and an index  $n_o$  in the  $x$ - and  $y$ -directions. The molecules are distributed cylindrically about the  $z$ -axis and the symmetry is similar to

that of a monoclinic crystalline system. This symmetry yields the electro-optic tensor given in contracted notation<sup>46</sup>

$$\vec{r} = \begin{bmatrix} 0 & 0 & r_{13} \\ 0 & 0 & r_{13} \\ 0 & 0 & r_{33} \\ 0 & r_{13} & 0 \\ r_{13} & 0 & 0 \\ 0 & 0 & 0 \end{bmatrix} \quad (3.6)$$

If an electric field is applied along the z-axis, then the equation for the change in the index of refraction Eq.(3.5) becomes

$$\Delta \left( \frac{1}{n_{ij}^2} \right) = \begin{bmatrix} 0 & 0 & r_{13} \\ 0 & 0 & r_{13} \\ 0 & 0 & r_{33} \\ 0 & r_{13} & 0 \\ r_{13} & 0 & 0 \\ 0 & 0 & 0 \end{bmatrix} \begin{bmatrix} 0 \\ 0 \\ E \end{bmatrix} = \begin{bmatrix} r_{13}E \\ r_{13}E \\ r_{33}E \\ 0 \\ 0 \\ 0 \end{bmatrix} \quad (3.7)$$

From this, the index ellipsoid becomes<sup>70</sup>

$$\left( \frac{1}{n_o^2} + r_{13}E \right) x^2 + \left( \frac{1}{n_o^2} + r_{13}E \right) y^2 + \left( \frac{1}{n_e^2} + r_{33}E \right) z^2 = 1 \quad (3.8)$$

The refractive index in the z-direction is then

$$\frac{1}{n_z^2} = \frac{1}{n_e^2} + r_{33}E \quad (3.9)$$

or

$$n_z = n_e (1 + n_e r_{33} E)^{-1/2} \quad (3.10)$$

Using the binomial approximation, Eq. (3.10) can be written as

$$n_z = n_e - \frac{n_e^3 r_{33} E}{2} = n_e + \Delta n_z \quad (3.11)$$

A similar expression can be written for the indices in the  $x$ - and  $y$ -directions which differ from Eq. (3.11) only in their dependence on  $r_{13}$  as opposed to  $r_{33}$  and on having a refractive index  $n_o$  as opposed to  $n_e$ .

$$\begin{aligned} n_x &= n_o - \frac{n_o^3 r_{13} E}{2} = n_o + \Delta n_x \\ n_y &= n_o - \frac{n_o^3 r_{13} E}{2} = n_o + \Delta n_y \end{aligned} \quad (3.12)$$

Thus, an applied electric field in the  $z$ -direction changes the refractive index of the polymer along the  $z$ -axis by an amount  $\Delta n_z$  and along the  $x$ - and  $y$ -axes by an amount  $\Delta n_x$  and  $\Delta n_y$ , respectively.

## 3.2 Transverse Electro-Optic Modulator

### 3.2.1 Mach Zehnder 2D Waveguide Modulator

When an optical field polarized along the  $z$ -direction propagates through a one-dimensional waveguide made of an electro-optic active material in the  $x$ - $y$  plane (such as a thin, poled polymer film), and an external electric field  $E$  is applied parallel to the  $z$ -direction, then its output phase is changed as given by

$$\Delta\phi = -\frac{2\pi}{\lambda} L \Delta n_z = \frac{\pi L n_e^3 r_{33} V}{\lambda d} \quad (3.13)$$

where  $E=V/d$ ,  $V$  is the applied voltage,  $d$  is the film thickness and  $L$  is the optical path in the film over which the voltage is applied. If the desired phase change is  $\pi$ , Eq. (3.13) can be solved for  $V_\pi$ , the voltage required to induce a  $\pi$  phase shift, to find

$$V_\pi = \frac{\lambda d}{n_e^3 r_{33} L} \quad (3.14)$$

There is also a change in the refractive index along the  $x$ - and  $y$ -axes as well (Eq. (3.12)). However, these changes depend on  $r_{13}$ , unlike the change along the  $z$ -axis, which

depends on  $r_{33}$ . Polarization along the  $z$ -axis is preferable over the  $x$ - and  $y$ -axes because, using the isotropic material model,  $r_{33}$  is three times larger than  $r_{13}$ .<sup>71</sup> This allows  $V_\pi$  to be reduced by a factor of three for light polarized along the  $z$ -axis.

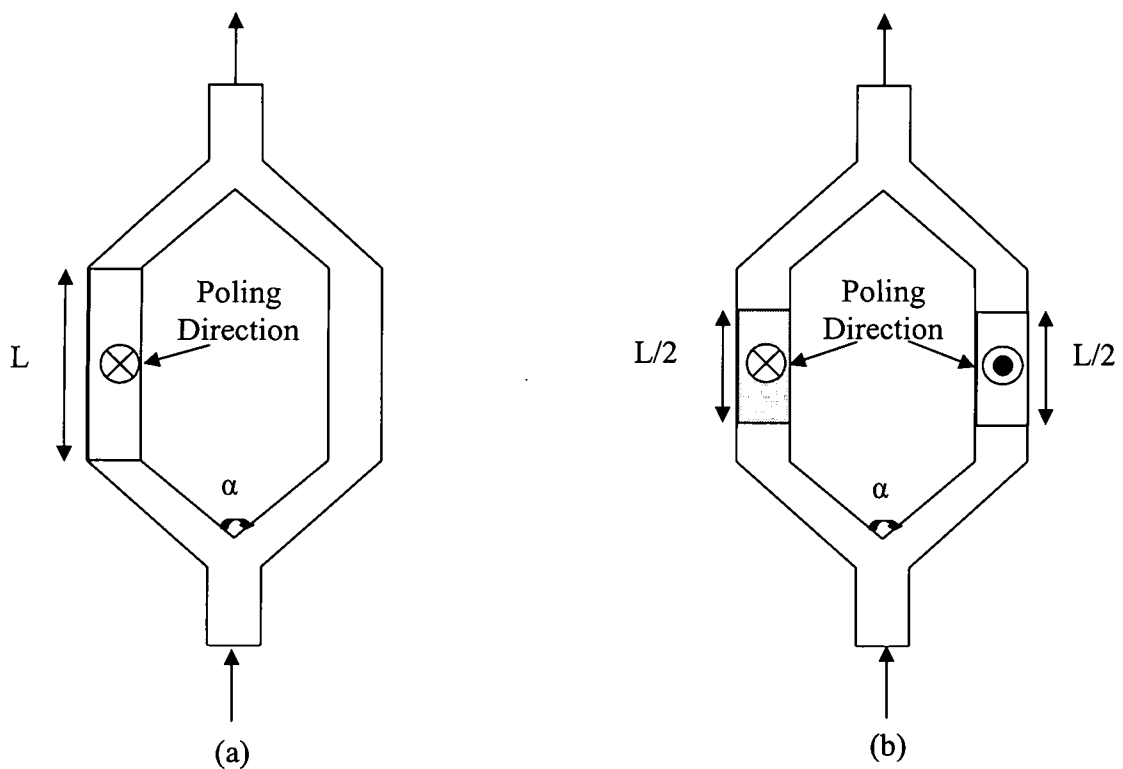


Fig. 3.1. (a) Typical MZ Configuration. With no voltage applied the light recombines after the two arms and constructively interferes, this is known as the “on” state. When the drive voltage  $V_\pi$  is applied across the poled region,  $L$ , a  $\pi$ -phase change is induced and the light destructively interferes upon recombination, this is known as the “off” state. (b) Push-Pull MZ Configuration. The two arms are poled in opposite directions. When the drive voltage  $V_\pi$  is applied across the oppositely poled arms, a  $\pi/2$  phase change is induced in each arm and the waves have a total phase difference of  $\pi$  upon recombination, causing them to destructively interfere and the device to be in an “off” state.

The expression for  $V_\pi$  in Eq. (3.14) is typically used to describe the performance of a Mach-Zehnder (MZ) type device. The MZ modulator is a two-dimensional (2D) waveguide device based on the principles of the interference of light waves. The MZ for a polymer device is typically formed by patterning the device in the core waveguide layer and then etching channels through reactive ion etch or another technique.<sup>62</sup> A light beam is split into two arms of equal physical length, each having half the amplitude of the original beam, and then is recombined. Assuming one arm is poled to make it electro-optic, when no voltage is applied to the poled arm of the MZ, the optical path lengths the two beams travel are exactly equal, and so when they recombine they constructively interfere to produce a beam with the original amplitude at the output, assuming no losses. This is known as the "on" state of the MZ. When the half-wave voltage in Eq. (3.14) is applied to the poled arm of the MZ, it introduces a  $\pi$  phase change in the beam of that arm. When the two beams recombine at the output, they now destructively interfere, and thus no light passes through the device. This is known as the "off" state.

A typical arrangement of a MZ device as described above is shown in Fig. 3.1(a). The arrangement of the MZ device shown in Fig. 3.1(b) is known as the push-pull configuration.<sup>20</sup> In the push-pull configuration, both arms of the MZ are poled at the same time, but in opposite directions. The positive terminal of the poling voltage is applied to the electrode on one arm and the negative terminal to the electrode on the other arm. Assuming there is a ground plane electrode between the substrate and the waveguiding film stack, this results in the alignment of the molecular dipoles in the two arms in opposite directions. From the poling viewpoint, this is equivalent to two identical capacitors in series. To modulate the device, the drive voltage  $V_\pi$  is applied to both arms

relative to the ground electrode, which introduces a  $\pi/2$  phase change in one arm and a  $-\pi/2$  phase change in the other arm. When the two recombine, the relative phase change is  $\pi$  and the two beams destructively interfere. The push-pull configuration is often desirable because it allows the length of the device to be cut in half. Alternatively, the same length  $L$  can be kept as in the original configuration and the modulating voltage  $V_\pi$  can be reduced by a factor of two.

A MZ EO modulator is ultimately the most useful application of a transverse EO modulator; however the 2D waveguide structures that are needed for this design would have required extensive development of etching and fabrication techniques to form these structures in the all-DNA-based films. Such a development can only be accomplished after the recipe for a successful all-DNA-based planar waveguide modulator has been determined, which has been a goal of this dissertation. To demonstrate the feasibility of an all-DNA-based modulator, a scheme utilizing a simple, planar waveguide structure will be utilized and tested using one of the two techniques described below.

### ***3.2.2 External Mach Zehnder Planar Waveguide Modulator***

Although a 2D MZ channel waveguide is beyond the scope of this work, the MZ concept can still be employed to test a planar waveguide modulator. This can be accomplished by splitting the incident beam and sending two, parallel beams through the waveguide device. One beam would propagate under the electrode (the poled area of the waveguide) and one would propagate next to the electrode (the unpoled area). The two beams are coupled out of the waveguide and brought together in a typical MZ arrangement, with care taken to ensure the two path lengths are approximately equal. A compensator is placed in one beam to adjust the relative phases of the two beams. It is



important to note that the amplitudes of the two beams must be equal at the detector. An attenuator in one of the beams can be used if the intensities are different. When no voltage is applied, the two beams are in-phase and constructively interfere. The compensator is then adjusted to achieve destructive interference. The path length for the beam propagating in the poled region (under the electrode) will change when a voltage is applied due to the electro-optically induced change in refractive index. This change, however small, will be detected by the corresponding change in the interference pattern between the two beams.

A schematic of this arrangement is shown in Fig. 3.2, and an image of the two parallel beams propagating through a single-layer planar waveguide is shown in Fig. 3.3. For this type of arrangement, either pure TE or pure TM light is used. If TE light is used, the  $V_\pi$  expression is the same as for the 2D MZ channel waveguide, given in Eq. (3.14). If TM light is used, the expression is nearly identical except that  $r_{33}$  is replaced by  $r_{13}$  due to polarization along the  $x$ -axis as opposed to the  $z$ -axis.

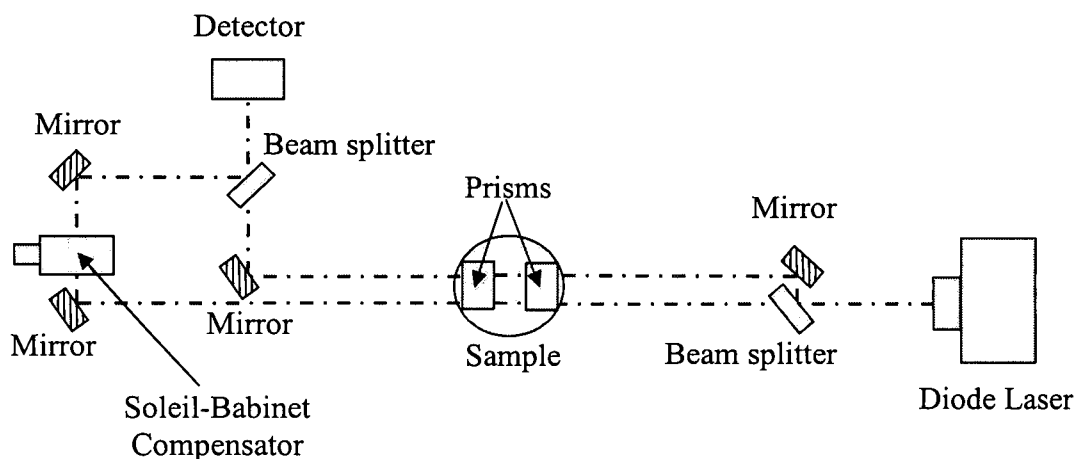


Fig. 3.2. Schematic of an external MZ planar waveguide modulator. The laser beam is split into two arms, each arm is prism coupled into and then out of the waveguide sample, and the two arms are then recombined onto a detector. A Soleil-Babinet compensator is used in one arm to adjust the relative phase between the two arms.

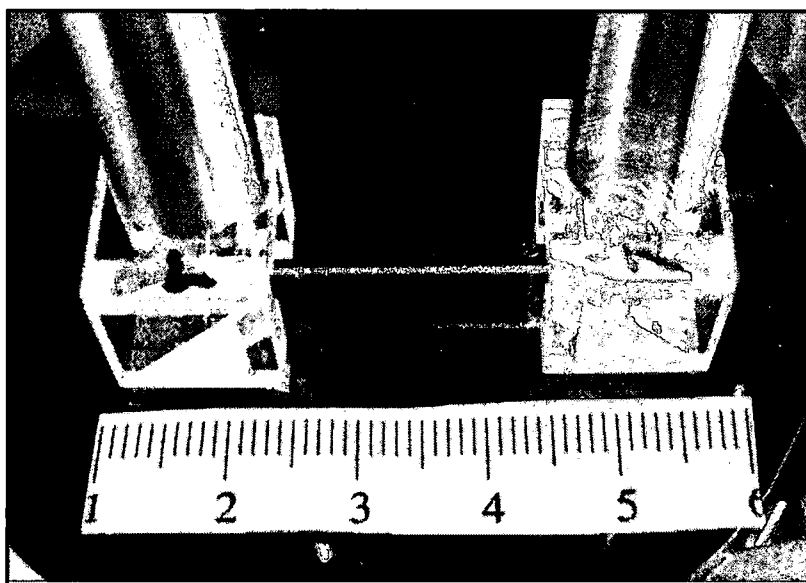


Fig. 3.3. Image of two parallel beams for use in an external MZ planar waveguide modulator. The beams are coupled in using the prism on the right and the prism on the left couples the beams out. The waveguide is a single layer DNA-CTMA film on an SiO<sub>2</sub> substrate.

### 3.2.3 Transverse Planar Waveguide Phase Modulator

A more classical technique for testing a planar EO waveguide structure is that of the transverse phase modulator. As with the external MZ planar waveguide, this device is also a simple, three-layer planar waveguide structure. Linearly  $45^\circ$  polarized light enters the device, a  $V_\pi$  is applied to change the polarization, and linearly polarized light at  $-45^\circ$  exits the device. By placing the modulator between crossed polarizers, this change in polarization can be easily detected.<sup>72</sup> With this configuration, the expression for the full-wave switching voltage  $V_\pi$  is changed somewhat from Eq. (3.14), due to components in both the z- and x-directions. The schematic for this testing arrangement is shown in Fig. 3.4.

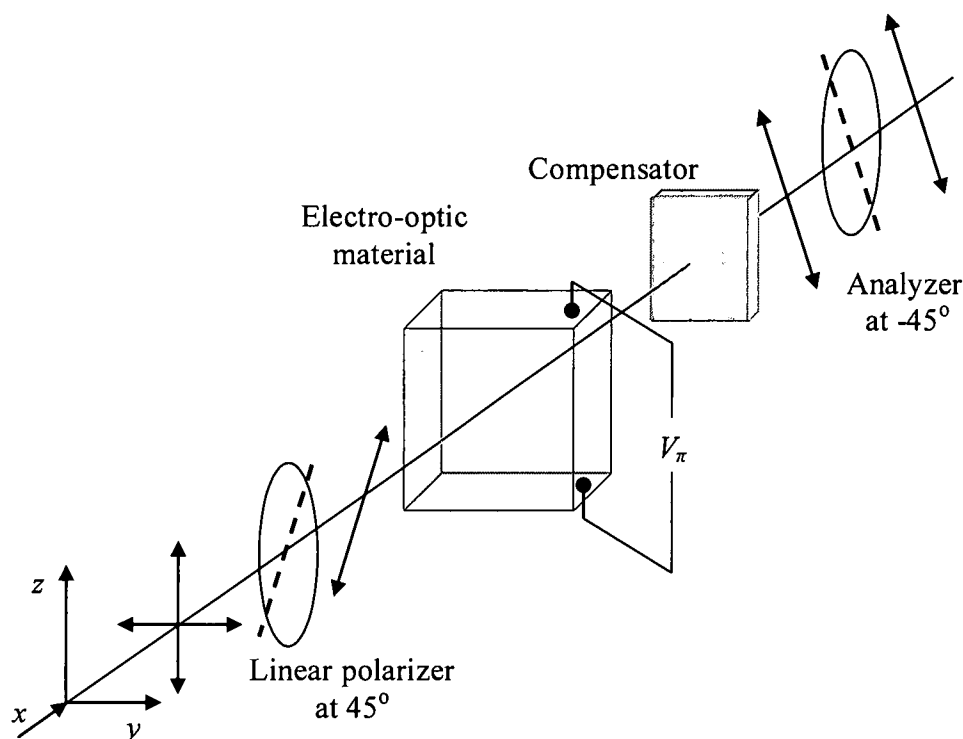


Fig. 3.4. Transverse EO phase modulator. The EO material is placed between crossed polarizers. A compensator is used to adjust the phase from elliptical to linear polarized light.

To detect a  $\pi$  phase shift in a one-dimensional EO modulator, light must enter the device with equal amounts of TE and TM polarization, assuming the modes are excited at nearly the same angle and that they propagate with nearly the same losses. With respect to Fig. 3.4, this means that the incident light must be polarized  $45^\circ$  with respect to the  $x$ - and  $z$ -axes. Therefore, since there is a component of polarization in the  $x$ -direction, the expression for  $V_\pi$  must be adjusted to account for this component. In addition, because the light exiting the modulator with no applied voltage has elliptical polarization due to different indices in the  $x$ - and  $z$ -directions, a compensator is needed to form linearly polarized light incident on the analyzer polarizer. This insures minimum light is passed by the analyzer in the absence of an applied voltage. Using Eqs. (3.12) and (3.13) in the weak poling limit,<sup>46</sup> which allows for the reasonable approximation that  $n_e \sim n_o \sim n$  the expression for the output phase becomes

$$\Delta\phi = -\frac{2\pi}{\lambda} L (\Delta n_z - \Delta n_x) = \frac{\pi L n^3 (r_{33} - r_{13}) V}{\lambda d} \quad (3.15)$$

Setting the phase change equal to  $\pi$ , gives a  $V_\pi$  of

$$V_\pi = \frac{\lambda d}{n^3 (r_{33} - r_{13}) L} \quad (3.16)$$

Again, using the isotropic material model where  $r_{33} = 3r_{13}$ , Eq. (3.16) can be simplified to

$$V_\pi = \frac{\lambda d}{n^3 \left( \frac{2}{3} r_{33} \right) L} \quad (3.17)$$

For this configuration only 2/3 of the maximum value of the EO coefficient can be utilized.

### 3.3 Measuring the Electro-Optic Coefficient

The EO coefficient of a polymer thin film is measured using an ellipsometric technique first described by Teng and Man.<sup>66</sup> The Teng and Man experimental set-up is shown in Fig. 3.5. The polymer film is spin-coated on a glass slide that is pre-coated with a layer of optically-clear, electrically-conductive indium tin oxide (ITO) with a gold electrode sputtered on top of the polymer. The EO coefficient  $r_{33}$  is measured with a laser source incident at an angle  $\theta$  on the glass side of the polymer film. The incident beam is polarized at  $45^\circ$  to the plane of incidence and the reflected beam is sent through an analyzer crossed at  $90^\circ$  with respect to the polarizer. The beam passes through the glass slide, ITO and polymer film, reflects off the gold, and passes back through the film, ITO and glass slide.

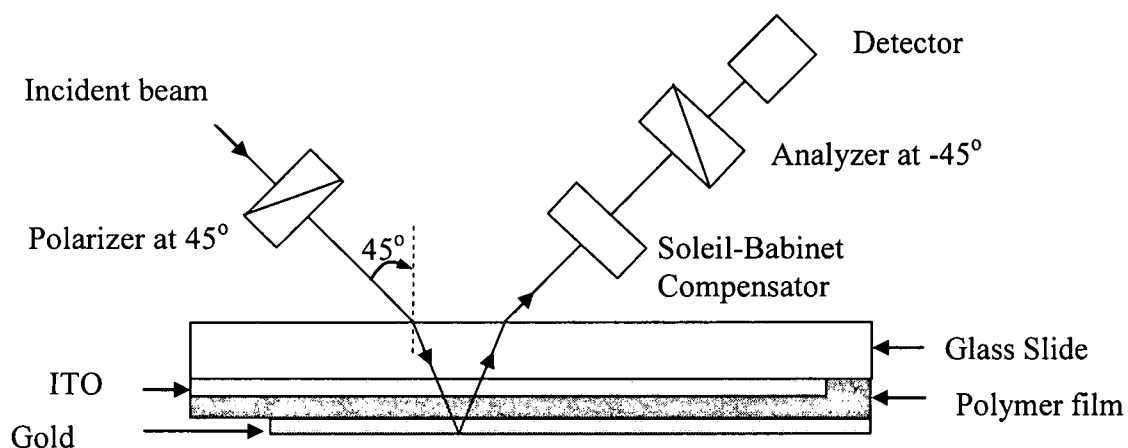


Fig. 3.6. Experimental set-up of Teng and Man technique for measuring the EO coefficient of a poled polymer film. [From Reference No. 67]

A Soleil-Babinet (SB) compensator is used to adjust the relative phase between the two components of the optical field, which changes the ellipticity of the polarization of the reflected beam. Changing the SB compensator changes the amplitude of the dc signal at the detector which varies in a sinusoidal pattern with wave shift. When a 1 kHz modulating voltage  $V_m$  is applied across the ITO and gold electrode, the film's refractive index is modulated. This produces an ac signal  $V_{ac}$  that is measured at the lock-in. The ratio,  $V_{ac}/V_{dc}$  is proportional to the derivative of the curve, which is related to the change in refractive index of the film induced by  $V_m$ . To maximize  $V_{ac}$ , the SB compensator is therefore set successively to the  $\pi/2$  and  $3\pi/2$  inflection points of the phase sinusoid. These inflection points are found by adjusting the compensator to find the maximum  $V_{max}$  and minimum  $V_{min}$  values.  $V_{dc}$  is then given by

$$V_{dc} = \frac{V_{max} - V_{min}}{2} + V_{min} \quad (3.18)$$

The compensator is then adjusted to one of these inflection points by finding the place where  $V_{dc}$  has the value found in Eq. (3.18). The modulating voltage  $V_m$  is applied across the electrodes and the resulting ac signal  $V_{ac}$  is measured. Theoretically, the signal values for  $V_{ac}$  at the  $\pi/2$  and  $3\pi/2$  inflection points have the same magnitude and vary only in their electrical phase signals; the phase will be positive at  $\pi/2$  and negative at  $3\pi/2$ . The expression for the EO coefficient  $r_{33}$  is given as

$$r_{33} = \frac{3\lambda}{4\pi n^2} \frac{\sqrt{n^2 - \sin^2 \theta}}{\sin^2 \theta} \frac{V_{ac}}{V_m V_{dc}} \quad (3.19)$$

where  $\lambda$  is the wavelength of the incident beam,  $n$  is the index of the polymer,  $V_m$  is the amplitude of the 1 kHz modulation voltage,  $V_{dc}$  is the dc signal when the SB is set to half

intensity, and  $V_{ac}$  is the measured ac signal at the lock-in due the modulation voltage.<sup>67</sup>

The expression for  $r_{33}$  in Eq. (3.19) is modified slightly from the original form as described by Teng and Man. A detailed derivation of this equation is presented in Appendix B.

As previously mentioned, the measured signal  $V_{ac}$  theoretically differs only by  $180^\circ$  electrical phase at the compensator optical phase settings of  $\pi/2$  and  $3\pi/2$  and should have zero amplitude at the optical phase setting of  $\pi$ . In reality, however, this situation only occurs for a transparent film with a purely real EO coefficient.<sup>67</sup> If there is an overlap between the measuring wavelength and the absorption band of the material, the Teng and Man measurements will be dependent on the inflection point used due to the electro-absorption effect (also called the electro-chromic or electro-reflectance effect).<sup>42</sup> In this case, the absorption effects can essentially be averaged out by averaging the  $V_{ac}$  values from the two phases, allowing a reasonable value for the EO coefficient to be obtained.

The averaging routine to eliminate the electro-absorption effects is dependent on the relative sizes of the EO effect compared to the electro-absorption effect. The ac signal value at  $\pi/2$ ,  $V_{\pi/2}$ , will always have a positive electrical phase and if the EO effect is dominant, the value at  $3\pi/2$ ,  $V_{3\pi/2}$ , will still have a negative phase, but the two will be different in amplitude. In this case, the value for  $V_{ac}$  will be

$$V_{ac} = \left| \frac{V_{\pi/2} - V_{3\pi/2}}{2} \right| \quad (3.20)$$

where  $V_{3\pi/2}$  is negative. If the electro-absorption effect is dominant, then the two signals have the same electrical phase (both positive), but different magnitudes. In this case, the

expression for  $V_{ac}$  is still given by Eq.(3.20), but now  $V_{3\pi/2}$  is positive. Because the magnitude of the electro-absorption effect depends on the incident intensity, whereas the EO effect depends on the derivative of the incident intensity, this averaging routine effectively cancels out the electro-absorption effect.<sup>73</sup>

Many of the EO measurements in this study are done at 690 nm on films containing the chromophore dye Disperse Red 1 (DR1), which has a peak absorption wavelength of 513 nm.<sup>26</sup> There is a slight overlap of the tail-end of the absorption band of DR1 with the 690 nm wavelength; this averaging routine, therefore, is essential to cancel the electro-absorption effects due to this overlap. The modified expression for the EO coefficient taking into account Eq. (3.20) can be written as

$$r_{33} = \frac{3\lambda}{4\pi n^2} \frac{\sqrt{n^2 - \sin^2 \theta}}{\sin^2 \theta} \frac{(V_{\pi/2} - V_{3\pi/2})/2}{V_m V_{dc}} \quad (3.21)$$

It is important to emphasize that this modified expression in Eq. (3.21) can be used to remove the electro-absorption effects only if the measurement is far from the absorption band. If the measurement wavelength significantly overlaps the absorption band, the absorption effects will dominate the observed signals and this averaging routine will not be accurate.<sup>67</sup> Levy *et al.* have shown that this simplified approach breaks down for measurements close to the absorption band.<sup>67</sup> This effect will be discussed in greater detail in Chapter 6.

Another consideration when making these types of measurements is the effect of interferences arising from partial reflections at the surfaces and interfaces of the specimen (air-substrate and substrate-polymer interfaces). These multiple reflections, which depend on the thicknesses of the layers and the wavelength of the incident light, are due



to the interference between forward and backward propagating waves and cause inaccuracies in the EO measurement.<sup>67</sup> Our experience is that for films  $\sim 2\text{ }\mu\text{m}$  or thinner, particular for near-IR wavelengths (e.g.,  $\sim 1300$  and  $\sim 1500\text{ nm}$ ), the introduced errors are  $<10\%$ . Moreover, the contributions from these spurious reflections can be effectively reduced by using a lens to focus the light on the film and a second lens to image the resulting spot onto a pinhole placed in front of the detector.<sup>73</sup> The pinhole is adjusted to reject, to the extent possible, the light coming from the first surface of the substrate (i.e., glass slide). However, the increased irradiance of the chromophore in the film due to the focusing can produce a “bleaching” of the measured local EO coefficient.<sup>73</sup>

### 3.4 Waveguide Theory

The concepts of guided waves are fundamental to this research. One of the simplest descriptions of an optical waveguide is a high-index dielectric material surrounded on either side by a lower-index dielectric material; this is known as a step-index planar slab waveguide. A schematic of this is shown in Fig. 3.6. The key to optical waveguiding is total internal reflection. A ray of light traveling within the high-index layer, known as the core layer, will be totally-internally-reflected at the boundary interfaces of the low-index layers, known as the cladding layers, if the angle of incidence at the interface exceeds the critical angle. When this condition is met, the waves will be guided along the core layer. The following theory uses the notation outlined by Pollock in *Fundamentals of Optoelectronics*.<sup>74</sup>

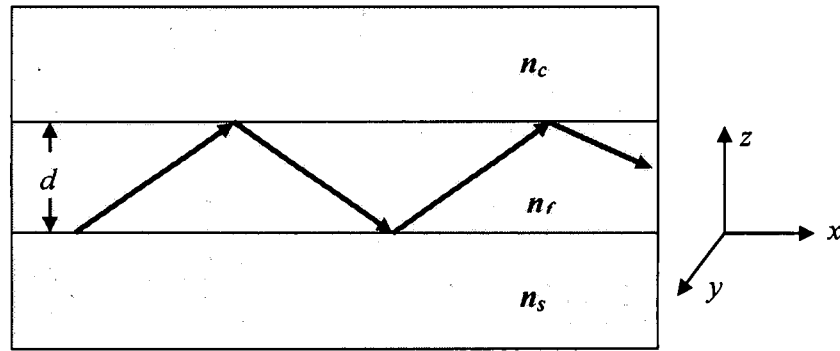


Fig. 3.6. Schematic of a planar slab waveguide. The light is confined by total internal reflection at the interfaces.  $n_f > n_c$  and  $n_f > n_s$

A waveguide can support only certain discrete modes. These modes are determined by the properties of the waveguide such as the indices of refraction, propagating wavelength, and thickness of the core layer. To find these allowed propagating modes, the wave equation must be solved in each dielectric region and then connected by using the boundary conditions at each interface. The wave equation is derived from Maxwell's equations. For a TE polarized wave propagating along the  $x$ -direction (Fig 3.6), the wave equation can be written in terms of  $E_y(x, z)$ , which is independent of  $y$  because the slab extends infinitely in the  $y$ -direction, and is given by

$$\nabla^2 E_y + k_o^2 n_i^2 E_y = 0 \quad (3.22)$$

where  $k_o = 2\pi/\lambda$  is the magnitude of the wavevector,  $n_i$  is the index of the layer of interest. A trial solution to this equation can be written as

$$E_y(x, z) = E_y(z)e^{-i\beta x} \quad (3.23)$$

where  $\beta$  is the propagation constant along the  $x$ -direction that has yet to be determined.

Noting that the electric field is continuous in the  $y$ -direction,  $d^2 E_y / dy^2 = 0$ , the trial solution in Eq. (3.23) is plugged into the wave equation (3.22) to find

$$\frac{\partial^2 E_y}{\partial z^2} + (k_o^2 n_i^2 - \beta^2) E_y = 0 \quad (3.24)$$

For notation simplicity, the following parameters are defined

$$\begin{aligned} \gamma_c &= \sqrt{\beta^2 - k_o^2 n_c^2} \\ \gamma_s &= \sqrt{\beta^2 - k_o^2 n_s^2} \\ \beta &= \sqrt{k_o^2 n_f^2 - K^2} \end{aligned} \quad (3.25)$$

where  $n_c$  is the index of the top cladding layer (the cover),  $n_s$  is the index of the bottom cladding layer (the substrate),  $n_f$  is the index of the core (the film), and  $K$  is to be determined by the eigenvalue equation. The solution to the wave equation in each region can be found to be

$$\begin{aligned} E_y(z) &= A e^{-\gamma_c z} & 0 < z \\ E_y(z) &= B \cos(Kz) + C \cos(Kz) & -d < z < 0 \\ E_y(z) &= D e^{\gamma_s(z+d)} & z < -d \end{aligned} \quad (3.26)$$

where  $d$  is the thickness of the core layer along the  $z$ -direction as shown in Fig. 3.6, and  $A$ ,  $B$ ,  $C$ , and  $D$  are amplitude coefficients to be determined by the boundary conditions. The boundary conditions require that the tangential components of the electric and magnetic fields be continuous. Using these conditions with the solutions in Eq. (3.26) and in conjunction with Maxwell's equations, an eigenvalue equation for the waveguide mode  $\beta$  can be derived for both the TE and TM modes in terms of the waveguide parameters. For the TE modes the eigenvalue equation is found to be

$$\tan(hK) = \frac{\gamma_c + \gamma_s}{K \left[ 1 - \frac{\gamma_c \gamma_s}{K^2} \right]} \quad (3.27)$$

and for the TM modes this eigenvalue equation is found to be

$$\tan(hK) = \frac{K \left[ \frac{n_f^2}{n_c^2} \gamma_c + \frac{n_f^2}{n_s^2} \gamma_s \right]}{K^2 - \frac{n_f^4}{n_c^2 n_s^2} \gamma_c \gamma_s} \quad (3.28)$$

These are transcendental equations that can be solved for  $K$  only numerically or graphically. For each unique waveguide structure, these equations were used to find the allowed propagating modes of the waveguide.

### 3.5 Waveguide Loss

The fraction of the propagating light that is lost due to absorption and scattering is an essential characteristic of polymer optical waveguides. For incident irradiance  $I_o$  over a path length  $t$  (cm), the absorption is described by Beer's Law<sup>75</sup>

$$I = I_o e^{-\alpha t} \quad (3.29)$$

where  $\alpha$  is the absorption coefficient or fractional loss per cm, which is given in terms of the transmittance  $T = I/I_o$  as

$$\alpha = -\frac{\ln(T)}{t} \quad (3.30)$$

This absorption coefficient can be generalized to include both the scattering coefficient  $\alpha_s$  and the absorption coefficient  $\alpha_A$  and can be written as  $\alpha = \alpha_s + \alpha_A$ . The transmittance is obtained as a function of wavelength with a dual-beam spectrophotometer. The decibel loss per cm (dB/cm) is the more useful number for characterizing waveguide loss and is given by

$$\text{Loss} = -10 \frac{\log(T)}{t} \quad (\text{dB/cm}) \quad (3.31)$$

It is typically desirable that waveguide losses be  $\leq 1$  dB/cm.<sup>2,4,43</sup>

### 3.6 Prism Coupling

There are several techniques commonly used to couple light into a waveguide. Among these are end coupling, grating coupling, and prism coupling.<sup>74</sup> In this research, prism coupling is the coupling method of choice because it is a nondestructive technique that requires no clean, exposed edges (as does end coupling) and it allows for quick and easy launching of a beam into a waveguide. In prism coupling, the incident beam is totally internally reflected at the prism-waveguide interface; this requires that the prism index be greater than the index of the film. The evanescent tail of the field is then coupled into the waveguide. Effective coupling between the evanescent field and the waveguide requires that the phase of a propagating mode in the film is phase matched to the field generated by the evanescent field. For an angle of incidence  $\theta_m$  within the prism this condition is met when<sup>74</sup>

$$\sin \theta_m = \frac{\beta_m}{k_o n_p} \quad (3.32)$$

The expression for  $\theta_m$  in Eq. (3.32) is the incidence angle at the base of the prism required to couple into the waveguide mode  $\beta_m$ . It is not the incidence angle at the face of the prism, which is the more useful angle to know in order to accurately couple an outside beam into a waveguide. Using simple geometry and Snell's law, this incidence angle can be easily found. Figure 3.7 shows an illustration of the problem.

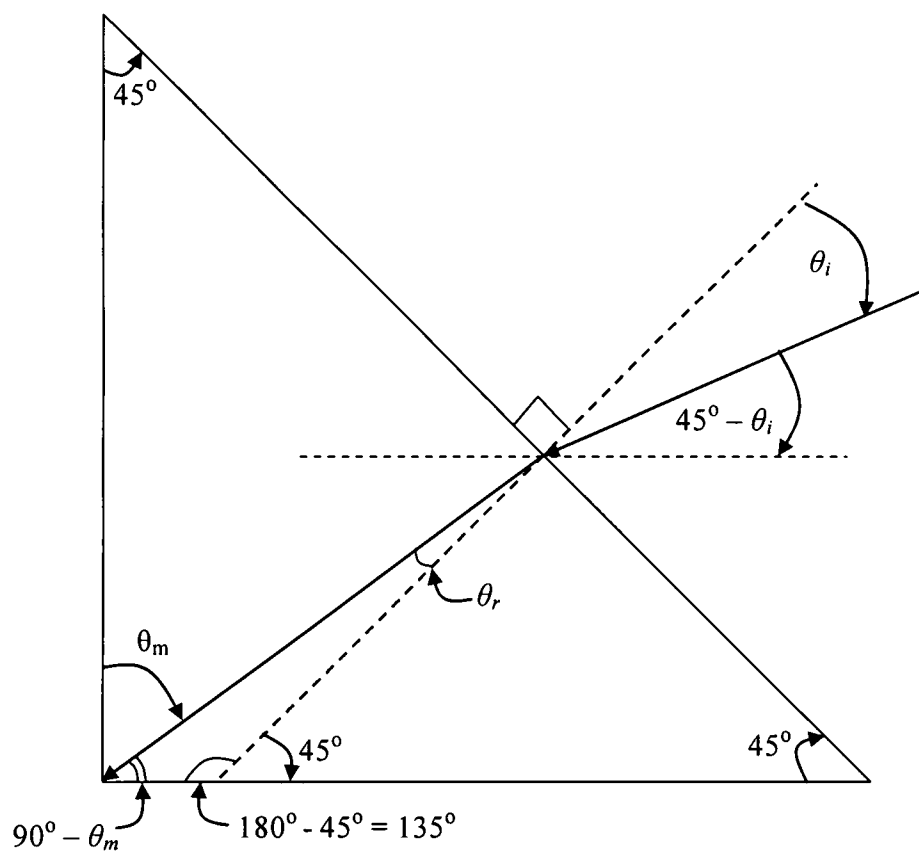


Fig. 3.7. Illustration of geometrical relationships between the angles involved for prism coupling into a thin film using a right-angle prism. The angle of incidence is  $\theta_i$ , the angle of refraction is  $\theta_r$ , and  $\theta_m$  is the coupling angle for a waveguide mode  $\beta_m$ .

The relationship between the angle of incidence  $\theta_i$  with respect to the normal of the prism face (for a  $45^\circ$ - $45^\circ$ - $90^\circ$  prism), and  $\theta_m$ , can be found as follows. Using Snell's law, the relationship between  $\theta_i$  and the angle of refraction is given by

$$n_i \sin \theta_i = n_p \sin \theta_r \quad (3.33)$$

Because the prism is in air,  $n_i = 1$ . Using straight-forward geometric principles, the following relationship between  $\theta_m$  and  $\theta_r$  can be found (see Fig. 3.7)

$$180^\circ = \theta_r + 135^\circ + (90^\circ - \theta_m) \quad (3.34)$$

This can be rearranged to show  $\theta_r = \theta_m - 45^\circ$ . Plugging this result into Eq. (3.33) and using the fact that  $n_i = 1$  gives

$$\theta_i = \sin^{-1} \left[ n_p \sin (\theta_m - 45^\circ) \right] \quad (3.35)$$

Finally, an expression for  $\theta_i$  can be found as a function of only the waveguide parameters and the index of the prism by using the expression for  $\theta_m$  in Eq. (3.32)

$$\theta_i = \sin^{-1} \left[ n_p \sin \left\{ \sin^{-1} \left( \frac{\beta_m}{k_o n_p} \right) - 45^\circ \right\} \right] \quad (3.36)$$

The angle of incidence on the face of the prism required to couple into a given waveguide mode  $\beta_m$  can be calculated using Eq. (3.36). Once the angle of incidence is calculated, the required height of the incident beam can be calculated to ensure that the incident angle is correct (see Fig. 3.8) and set the optics accordingly. Referencing Fig. 3.8, for a film a distance  $x_l$  away from the mirror controlling the angle of the incident beam, the height  $h$  of the mirror needed to prism couple into the film with a required incidence angle of  $\theta_i$  is

$$h = x_l \tan (45^\circ - \theta_i) \quad (3.37)$$

Using this relationship, it is possible to accurately set the height of the mirror controlling the angle of incidence that is a fixed horizontal distance away such that the requirements for prism-coupling into a given waveguide mode, given by  $\beta_m$  can be satisfied.

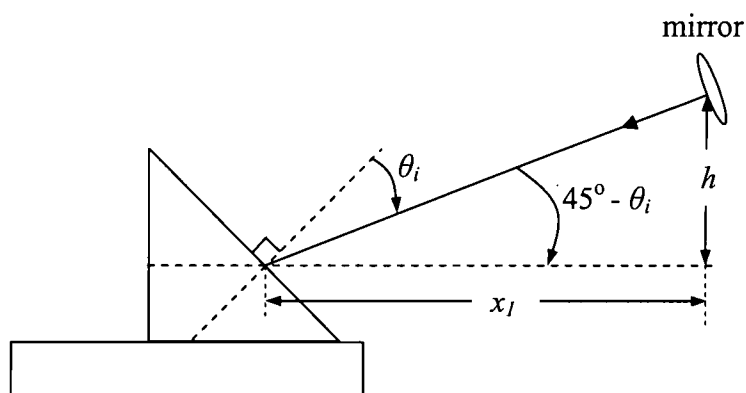


Fig. 3.8. Illustration of relationship between the position of a mirror a horizontal distance  $x_l$  away, with vertical height  $h$  and the angle of incidence  $\theta_i$  required to couple into waveguide mode  $\beta_m$ .  $\tan(45^\circ - \theta_i) = h/x_l$

The need to easily launch a beam into a film prompted the development of a prism-coupling scheme based on the above theory.<sup>42,73</sup> The design of the prism-coupling apparatus incorporated two basic ideas: 1) that the prism itself would be mounted in a plastic holder, thus protecting it from damage and finger prints while making it easy to handle, and 2) the force required to reduce the air gap between the prism and the film would be applied to the free-standing prism-holder assembly by springs compressed by a micrometer.<sup>73</sup> The micrometer permits fine control of the force. A schematic diagram of the prism coupling setup is shown in Fig. 3.9, and photos of the plastic prism-holder



assembly and the setup are shown in Fig. 3.10. It uses a right-angle prism made of SF11 glass, which has an index higher than the materials used in this research. The prism dispersion is shown in Fig. 3.11. The upper mirror has high-precision tilt capability and is mounted on a vertical micrometer translation stage, which permits very fine adjustment of the incident angle. The initial mirror position is set to a height  $h$  determined by Eq. (3.37); however, it must then be adjusted by trial and error due to the slight inaccuracies associated with the measurement parameters in order to achieve the optimum coupling angle. The footprint of the beam on the face of the prism in contact with the film (the bottom face) must be just at the vertical face of the prism (Fig. 3.7).<sup>76</sup> Coupling efficiency also requires that the beam be as small as possible, as a smaller the beam size will result in a higher coupling efficiency.<sup>76</sup> For this reason, a lens may be desired to focus the input beam. This arrangement has proven to be a straight-forward and relatively easy way of coupling a laser beam into a thin film waveguide.

One detail with this setup that is not immediately obvious is that the upper mirror used to correctly position the beam on the prism face may need to reflect the beam at an angle steeper than those for which the optics are typically designed due to a high angle of incidence on the prism. Regarding Fig. 3.7, this angle is  $\theta_i + 45^\circ$  with respect to the vertical bisector of the prism face. This angle depends on the indices and thicknesses of the waveguide layers, which determine the waveguide modes. This can pose a problem if linearly polarized light other than pure TE or TM is required to propagate through the waveguide (as it is for the transverse phase modulator, Sec. 3.2.3). It is common for mirrors to have a thin, dielectric coating that, for steep angles of reflection, can change the initial polarization of the incident beam. A simple solution to this problem is to coat

the mirrors with a thin metallic layer ( $\sim 2000 \text{ \AA}$ ), such as gold. This is sufficient for covering the dielectric layers and preserving the polarization of the reflected beams at steep angles.

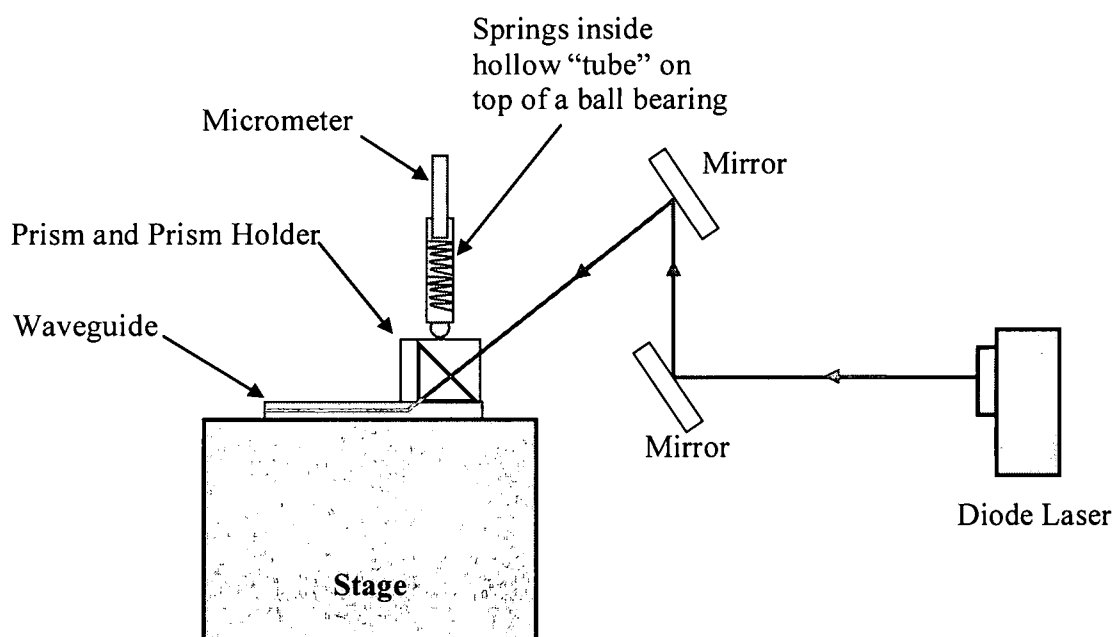


Fig. 3.9. Schematic of prism coupling setup. Pressure is applied to the prism via a micrometer that pushes against springs in the hollow "tube", which in turn pushes against the ball bearing in contact with the prism holder.

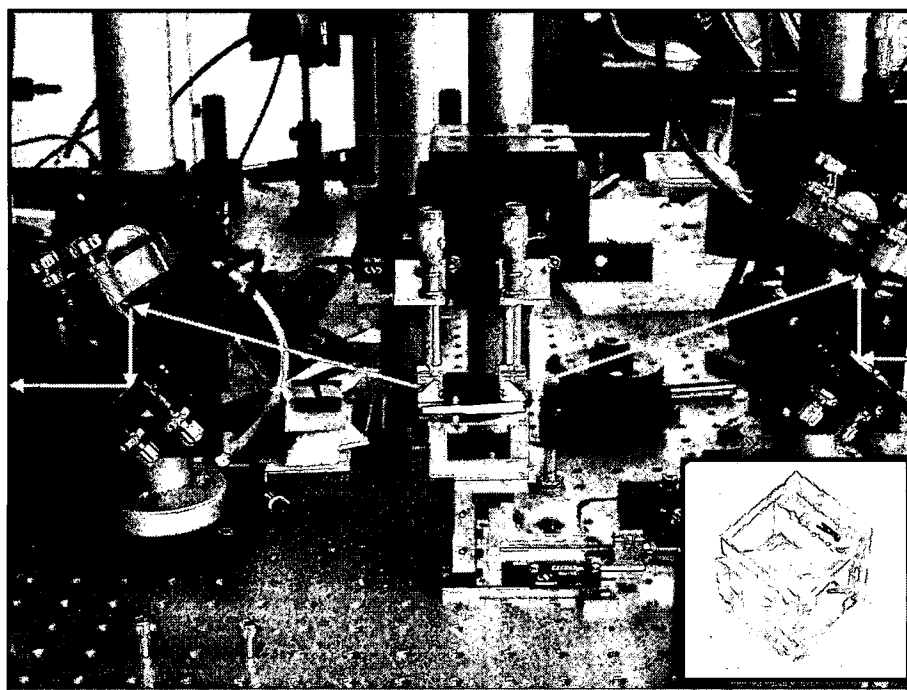


Fig. 3.10. Image of prism coupling setup with close-up of prism in the foreground.

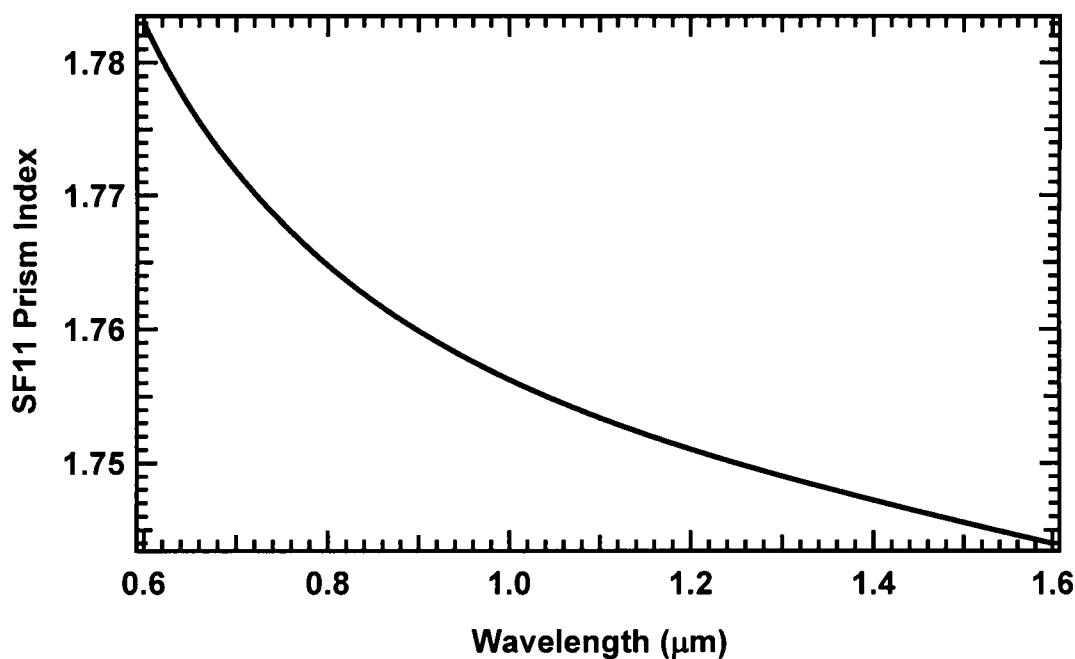


Fig. 3.11. Index of refraction of SF11 prism used for prism coupling. Curve was generated using the Sellmeier equation with coefficients provided by the Schott Glass Catalog. These coefficients are  $a_1 = 1.73848403$ ,  $a_2 = 0.31116897$ ,  $a_3 = 1.17490871$ ,  $b_1 = 0.0136069$ ,  $b_2 = 0.06159605$ , and  $b_3 = 121.922711$ . [From Reference No. 78]

The Sellmeier equation is given as 
$$n^2 = 1 + \frac{a_1 \lambda^2}{\lambda^2 - b_1} + \frac{a_2 \lambda^2}{\lambda^2 - b_2} + \frac{a_3 \lambda^2}{\lambda^2 - b_3}$$

## CHAPTER 4

### DNA PROCESSING

#### 4.1 DNA Purification

The DNA used in this research was purified by the Chitose Institute of Science and Technology (CIST) in Hokkaido, Japan from salmon roe and milt sacs, waste products of the Japanese fishing industry, using an enzyme isolation process. The use of salmon spermatozoa as a rich source for DNA is not new;<sup>77</sup> what is new is the ability to extract and purify the DNA on a scale of mass production. Although the exact purification details are proprietary, the general steps of the purification process are known as this process is simply a variation on time-proven DNA extraction techniques that have been in use for decades.<sup>77</sup> First, the material is homogenized by mixing the material in a blender. This breaks down the protective coating surrounding the DNA. The DNA then undergoes an enzymatic treatment by Protease to degrade the proteins. These proteins are then eliminated by maintaining a pH of 7.5. The remaining DNA then undergoes a carbon treatment for decolorization. Next, ethanol or acetone is added to precipitate the DNA out of solution. The DNA is then filtered and freeze-dried.<sup>27,33</sup> The

final DNA that we receive from CIST is reported to have a purity of ~96% with a protein content of ~2%.

## 4.2 Molecular Weight

For consistency, the molecular weight of DNA in terms of base-pairs (bp), 660 g/mol/bp, is used for all calculations of concentration ( $\text{mM bp}^{-1}$ ) and mol%. This is in contrast to using the actual molecular weight based on the lengths of the DNA strands ( $660\text{g/mol/bp} \times \text{number of bp} = \text{Da}$ ).<sup>65</sup> The molecular weight reported in terms of the lengths of the DNA strands has an uncertainty of  $\pm 50\%$  due to the wide distribution of strand lengths from the sonication process. The base-pair molecular weight, however, remains constant regardless of the DNA strand lengths. Additionally, it is necessary to refer to the molecular weight of the DNA-CTMA complex, for which there are two CTMA molecules for every DNA base pair (one CTMA cation for each DNA anion). Given that the molecular weight of CTMA is 319.75 g/mol, this yields a combined molecular weight of  $660\text{ g/mol/bp} + 2(319.75\text{ g/mol}) = 1299.5\text{ g/mol/bp}$  for DNA-CTMA in terms of DNA base pairs. In all following calculations for concentration and mol%, this molecular weight of the DNA-CTMA complex, 1299.5 g/mol/bp, is used. Molecular weight in Daltons is still a useful quantity and will be referenced when appropriate.

When referring to relative concentrations in a solution or film, the concentration in both wt% and mol% will initially be given. Thereafter, however, the concentration will be given in wt% only as this is the standard quantity typically reported in polymer literature. It is also a more intuitive quantity and therefore, in some cases, more useful. Appendix A provides a detailed explanation of calculating both wt% and mol%.

#### ***4.2.1 Lowering Molecular Weight***

The molecular weight of the DNA provided by CIST was measured to be greater than 8000 kDa using agarose gel electrophoresis. This high molecular weight DNA is difficult to process into an optical waveguide quality film due to its high viscosity in solution. In addition, we have found that the starting molecular weight of the DNA greatly affects poling efficiency. It is necessary to reduce the molecular weight of the DNA to at least 1000 kDa to achieve an appreciable EO coefficient through electrode poling. To reduce the molecular weight, an ultrasonic processor is used. The Sonics & Materials ultrasonic processor model VC-750 with a 19-mm diameter high-gain solid probe can process up to 500 mL of solution and can reduce the mean molecular weight of the CIST DNA to as low as 200 kDa.<sup>79</sup>

The ultrasonic processor works by irradiating the molecular liquid with high frequency sonic energy generated by a piezoelectric transducer probe. The probe creates intense ultrasonic pressure waves in the liquid. These pressure waves produce microscopic bubbles, or cavities, within the liquid. The cavities expand during the negative pressure excursion and violently implode during the positive excursion. This creates millions of shock waves and releases high levels of energy into the liquid. These high levels of energy cause the DNA to be randomly sheared across the double helix. As more energy is delivered to the solution, the strands of DNA are shortened so that each DNA strand contains fewer and fewer base pairs. Using ultrasonics in this manner, it is possible to reduce the MW of DNA from 8 million Daltons (8000 kDa) to less than 200 kDa.

To begin with, two grams of DNA are dissolved in 500 mL of 14 MΩ·cm distilled/deionized water at room temperature. The DNA is then sonicated on ice in ten-second pulses with a twenty-second rest period between each pulse. Figure 4.1 shows the molecular weight as a function of total sonication energy. Sonication does not uniformly reduce the size of the DNA strands; rather it randomly breaks the DNA into a Gaussian-like distribution of molecular weights. The molecular weight reported is the mean of this distribution of molecular weights with a variation of approximately  $\pm 50\%$ . The molecular weight is measured using agarose gel electrophoresis with a 0.8% agarose gel.<sup>80</sup> After sonication, the aqueous DNA solution is filtered through a nylon filter with a 0.45  $\mu\text{m}$  pore size to remove non-DNA particles (such as carbon black) created during sonication.

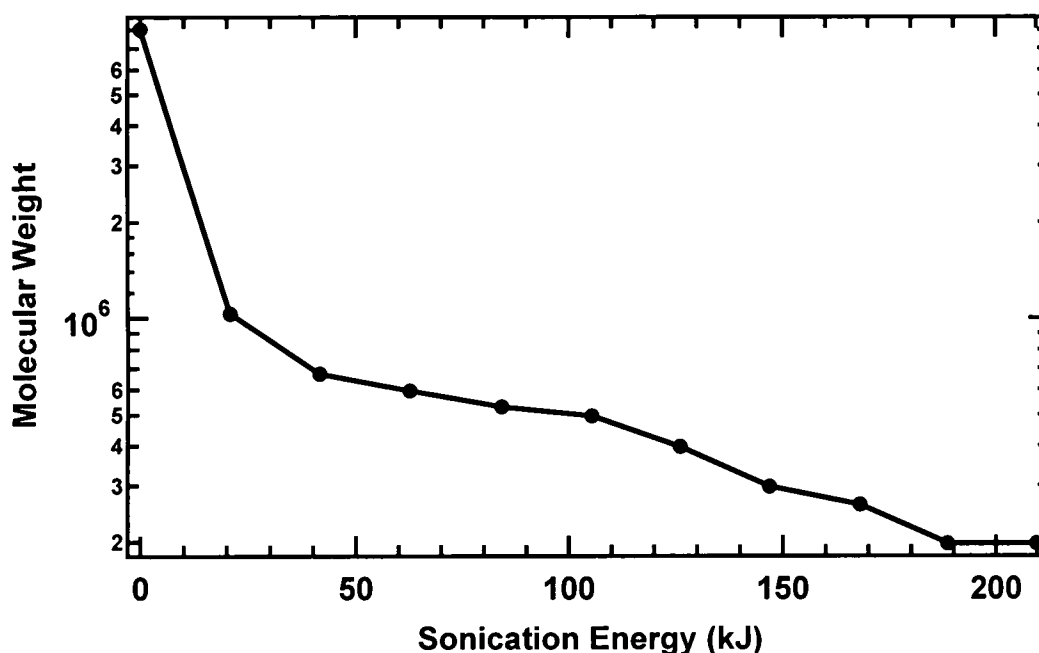


Figure 4.1. Molecular weight of DNA as a function of total sonication energy. The DNA was sonicated on ice in 10-s-long pulses with a 20-s rest period between pulses to prevent overheating of the sample.



#### ***4.2.2 Measuring Molecular Weight***

Gel electrophoresis is a common biological technique used to measure the molecular weight of DNA molecules.<sup>80</sup> DNA samples are loaded into an agarose gel and an electric field is applied across the samples. Because DNA molecules are negatively charged, the strands will be repelled by the negative charge and will move through the gel toward the positive charge. The gel consists of many microscopic holes that the DNA strands must weave in and out of in order to travel through the gel. The short DNA strands are able to move more quickly through the gel than long DNA strands. Over time, the shorter DNA strands will have migrated farther from the starting point than the longer strands. By using a known DNA ladder (a sample of DNA with many known molecular weights), the molecular weight of the DNA strands can be computed by comparing the location of the unknown strands with those of the ladder.

Powdered agarose, a dried powder similar to gelatin but made of seaweed, is dissolved in a 1x TAE (Tris-Acetate-EDTA) buffer at a concentration of 0.8%. To accommodate the size of our gel holder, a total amount of 200 mL TAE and 1.6g of agarose was used. A higher percentage (up to 2%) of agarose would be used for lower molecular weight DNA strands. The agarose-TAE solution must be brought to a boil in order to dissolve the agarose. After the agarose is dissolved, the agarose-TAE solution is allowed to cool for several minutes. Once cooled, 4  $\mu$ L of EtBr, a fluorescent dye, is added to the agarose-TAE solution to stain the DNA and make it visible under UV exposure. The solution is then poured into the gel holder and a gel comb is inserted at one end to define the wells. After 30 minutes, the gel will have hardened and the gel comb can be removed, leaving many well-defined wells in the gel.

A 1x TAE buffer is poured over the gel into the gel holder until the gel is completely covered. An additional 5  $\mu$ L of EtBr is added to this buffer and gently rocked until the EtBr disappears. The first well is loaded with a DNA ladder that has been mixed with a DNA loading dye at a concentration of 1:2 DNA ladder: DNA loading dye. There are many DNA ladder standards available; a 1 Kbp (kilo-base pair) ladder was used due to the high molecular weight of the samples and can be seen in Fig. 4.2.<sup>81</sup> Each additional well is loaded with a DNA sample that has also been mixed with the DNA loading dye at a concentration of 1:2 DNA sample: DNA loading dye. The DNA sample itself is an aqueous solution in deionized water at a concentration of 1 g/ 2 L.

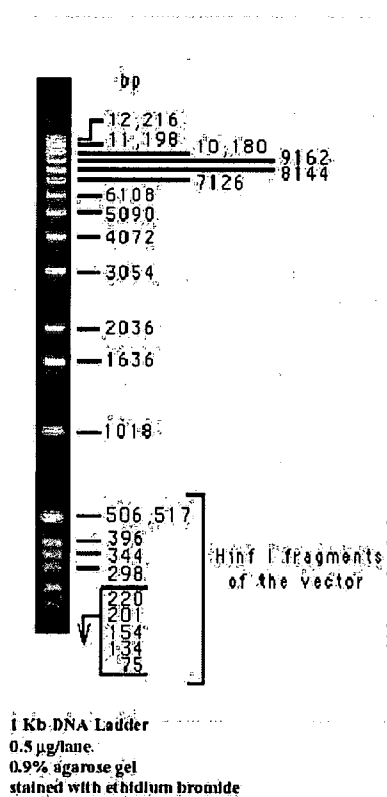


Figure 4.2. 1 Kbp DNA ladder  
[From Reference No. 81]

After all of the samples have been loaded into separate wells, a current is applied across the gel, with the positive lead at the farthest end of the gel to encourage DNA migration across the length of the gel. A constant voltage of 150V is applied for approximately one hour. The gel is then removed from the gel holder, placed under a UV source and a picture is taken of the illuminated DNA strands. By comparing the brightest spot of the DNA samples with the ladder, the number of base pairs of the sample can be calculated. This is demonstrated in Fig. 4.3. The molecular weight is then calculated by multiplying the number of base pairs by 660 g/mol/bp.

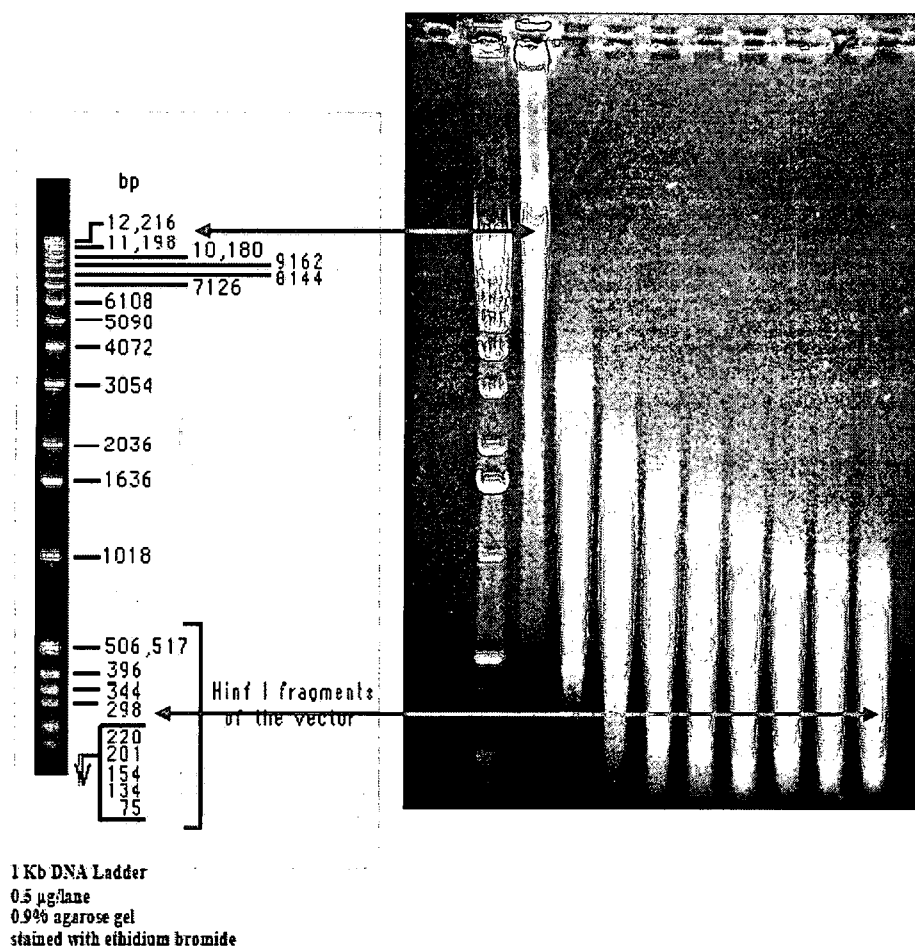


Figure 4.3. On the left the 1 Kbp DNA ladder standard is compared to a picture of the results of an agarose gel electrophoresis run. The first column on the left is the 1 Kbp DNA ladder. The second column is the unsonicated DNA, showing it has an initial molecular weight of ~12,000 bp or ~8000 kDa. The last column DNA that has been sonicated for ~200 kJ and shows that it has a molecular weight of ~300 bp or ~200 kDa.

### 4.3 Precipitation with CTMA Surfactant

The DNA is initially soluble only in aqueous solutions and does not dissolve in any organic solvent. We precipitate it with the cationic surfactant complex hexadecyltrimethylammonium-chloride (CTMA) to make it water insoluble and to provide increased molecular stability.<sup>27,28</sup> This is done through an ion exchange reaction as illustrated in Fig. 4.4. The CTMA surfactant was chosen over other surfactants for two reasons. First, the alkyl chain length of 16 for CTMA was ideal. Cationic surfactants with alkyl chains shorter than 16 might induce poor mechanical properties of the material while surfactants with longer alkyl chains are water insoluble (which complicates the precipitation process since it cannot be initially dissolved in water) and pose the risk of damaging the DNA double helical structure.<sup>27</sup> Secondly, the CTMA surfactant was commercially available. It was obtained from Fisher Scientific and used without further purification.

To precipitate the DNA with the CTMA cationic surfactant, the DNA is first dissolved at room temperature in 14 MΩ·cm distilled/deionized water at a ratio of 4g/L using a magnetic stirrer. If necessary, the molecular weight of the DNA is reduced with the ultrasonic processor as described in Sec. 4.2.1. An equal amount by weight of CTMA is likewise dissolved in 14 MΩ·cm distilled/deionized water, also at a concentration of 4g/L. Using equal amounts of DNA and CTMA by weight ensures that there is one CTMA molecule for each DNA base pair. One gram of DNA dissolved in 250 mL of 14 MΩ·cm distilled/deionized water means that there is  $(1\text{g})/(660\text{ g/mol/bp}) = 0.001516\text{ mol/bp}$  since the molecular weight of DNA in terms of base pairs is 660 g/mol/bp.<sup>65</sup> The formula weight of CTMA is 319.75 g/mol. To have one CTMA molecule per base pair

of DNA means we must have  $2 \times (0.001516 \text{ mol}) = 0.00303 \text{ mol}$  of CTMA. Multiplying the moles of CTMA by the formula weight of CTMA gives  $(319.75 \text{ g/mol}) \times (0.00303 \text{ mol}) = 0.97 \text{ grams}$  or  $\sim 1 \text{ gram}$  of CTMA for 1 gram of DNA. Reducing the molecular weight by sonication does not change the amount of CTMA needed to precipitate 1 gram of DNA. One gram of DNA, whether it has a molecular weight of 8000 kDa or 300 kDa, will still have the same number of base pairs, all that will be different is the overall strand lengths of the DNA chains.

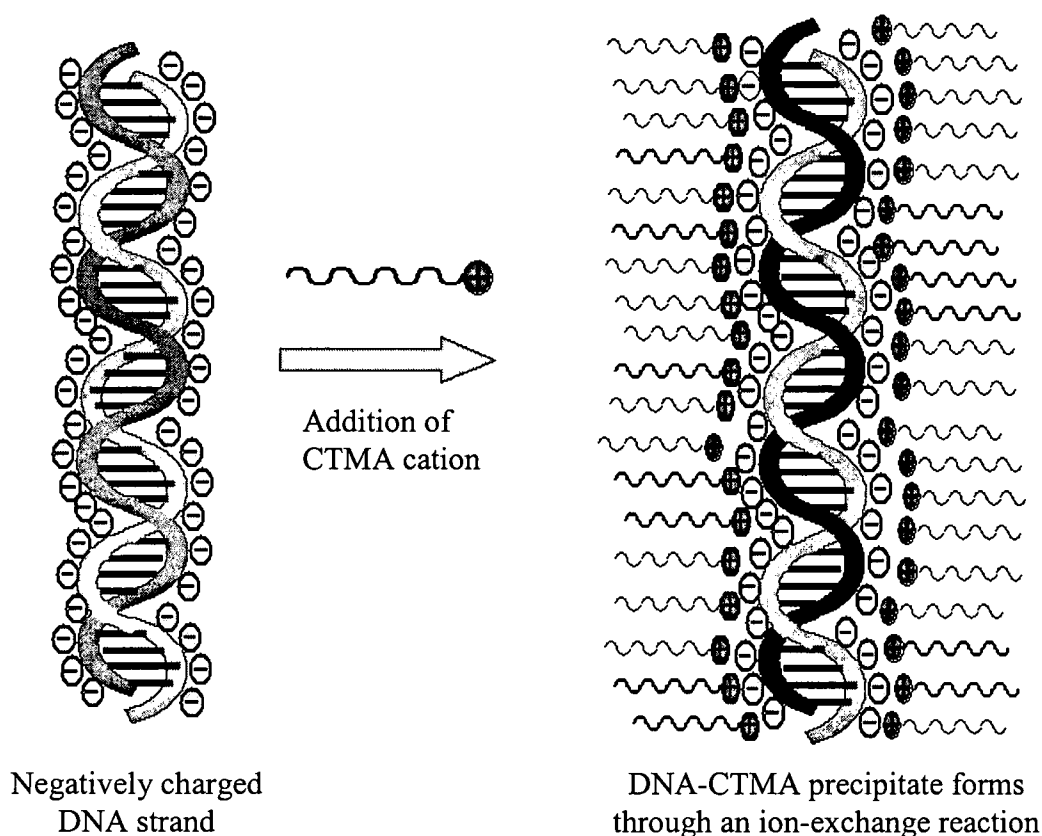


Figure 4.4. Illustration of formation of DNA-CTMA complex.

The DNA solution is added drop-wise to the CTMA solution with a burette. A white DNA-CTMA precipitate forms as the DNA is added to the CTMA. The solution is mixed for an additional four hours at room temperature. The precipitate is removed by filtering the solution using a TX 609 Technicloth low-lint clean-room paper as a filter. Using this type of filter allows for the precipitate to be periodically squeezed within the filter paper to remove any unprecipitated CTMA. It also provides a more complete rinsing of the DNA-CTMA precipitate. During the filtering process, an additional 3 to 4 L of 14 M $\Omega$ ·cm distilled/deionized water are poured through the filter to rinse the precipitate and to ensure that any CTMA that did not bind to the DNA is thoroughly rinsed away. When the water running through the filter comes out clear and there is no evidence of surfactant bubbles, it is assumed that the precipitate has been thoroughly rinsed. The precipitate is then collected, placed in a Teflon beaker and dried in a vacuum oven overnight at 40 °C. This excessive rinsing and periodic squeezing of the precipitate within the filter is essential to obtaining a pure DNA-CTMA sample with no unprecipitated CTMA mixed in. This method yields a white, powdery DNA-CTMA precipitate. Although squeezing the DNA-CTMA precipitate in the filter paper is the most effective way we have found to remove the excess CTMA, one drawback of this method is that filter fibers tend to stick to the precipitate. These fibers are eventually removed by using a 0.2  $\mu$ m syringe filter as described below (Sec. 4.4.2). An alternative method of filtering the precipitate which poses no risk of filter fiber contamination is to use a 20  $\mu$ m pore size nylon filter. It is much more difficult, however, to thoroughly rinse the DNA-CTMA using the nylon filter as the precipitate clumps up and prevents effective rinsing. The precipitate rinsed in this manner is more crystalline than powdery, evidence

of excess unprecipitated CTMA. The possibility of contamination by filter paper fibers is, therefore, chosen over the possibility of a DNA-CTMA precipitate that has not been thoroughly rinsed and the filter paper squeeze method is used over the nylon filter method.

#### **4.4 Preparation of DNA-CTMA Films**

##### ***4.4.1 Spin Parameters***

Achieving uniform film thickness with the DNA biopolymer proved to be more complicated than originally thought. Initially, the DNA-CTMA was dissolved in butanol by mixing for 1-2 hours in a 60 °C oven using an ATR Rotamix tumbling mechanism until all of the DNA-CTMA appeared to be fully dissolved in the solution. However, we had tried various spinning parameters with these solutions and were unable to achieve films with reasonably uniform thickness; variations would be well over 0.5  $\mu\text{m}$  for a 2-3  $\mu\text{m}$  thick film. For waveguide applications, this variation in thickness is unacceptable. Additionally, it made accurate measurements of other DNA-CTMA properties, such as resistivity, nearly impossible.

Because the DNA contains a broad distribution of molecular weights (Sec. 4.2), we hypothesized that the most likely reason we were unable to achieve uniformly thick films was due to insufficient distribution of the DNA chains in solution. That is, we believed that the longer DNA chains were not equally distributed in solution and therefore aggregation was occurring during the spin-coating process. To counteract this, we tried sonicating the DNA-CTMA butanol solution in a water bath for four hours in addition to the two hours it was initially mixed using the Rotamix. For comparison, we allowed an identical solution to continue mixing on the Rotamix for the four hours the



other solution was being sonicated. We were then comparing two identical solutions, one that had mixed on the Rotamix for six hours, and one that had been mixed on the Rotamix for two hours and sonicated for an additional four hours. Additionally, we tried varying the spinning parameters. Each solution was spin-coated on a plain glass slide substrate with two different spinning parameters: one at 1000 rpm for ten seconds with a five second ramp, and one at 1000 rpm for ten seconds with no ramp.

The thickness of the films was measured using a Veeco Dektak profilometer. Because the glass slides are not perfectly flat and can have variations of up to 0.5  $\mu\text{m}$ , a scratch was made on the film so that the profile of the plain glass slide could be measured first. The film profile was then measured as close as possible to the scratch, starting on an area of plain glass slide to use as a reference (see Fig. 4.5). The absolute film thickness was then obtained by subtracting the glass profile from the film+glass profile and a line with the slope held to zero was fit to this difference. This technique allows the variations in the glass substrate to be factored out.

Using this comparison process for two different molecular weight DNA-CTMA-butanol solutions, 200 kDa and 5,000 kDa, we found that there was little difference between the solutions that were sonicated and were mixed with the Rotamix for six hours. Rather, the longer mixing time of six hours seemed to be key, whether that additional mixing took place using sonication or the Rotamix was immaterial. Additionally, we found that using a five second ramp with the spin parameters gave a much more uniform film for both the 200 kDa and 5,000 kDa solutions than did the spin parameters without a ramp. For the 200 kDa solution that was mixed using the Rotamix for the entire six hours, the film thickness using a five second ramp was  $t = 2.298 \pm 0.05$

$\mu\text{m}$  over 14 mm, while the film thickness for no ramp was  $t = 2.056 \pm 0.4 \mu\text{m}$  over 14 mm. For the 5,000 kDa solution that was mixed using the Rotamix for the entire six hours, the film thickness using a 5 sec ramp was  $t = 0.751 \pm 0.1 \mu\text{m}$  over 6 mm (the smaller distance is due to a measurement error, and does not represent a failure on the part of the film itself), while the film thickness for no ramp was  $t = 0.746 \pm 0.3 \mu\text{m}$  over 14 mm. These results were obtained with a Veeco Dektak profilometer. Figures 4.6 – 4.9 show the thickness profiles for the results reported above. They were obtained by using the profilometer to scan the film thickness and a scan of the glass thickness was then obtained immediately next to the film. The thickness of the glass slide was then subtracted from the thickness of the film profile to remove any variations in thickness due to the glass slide.

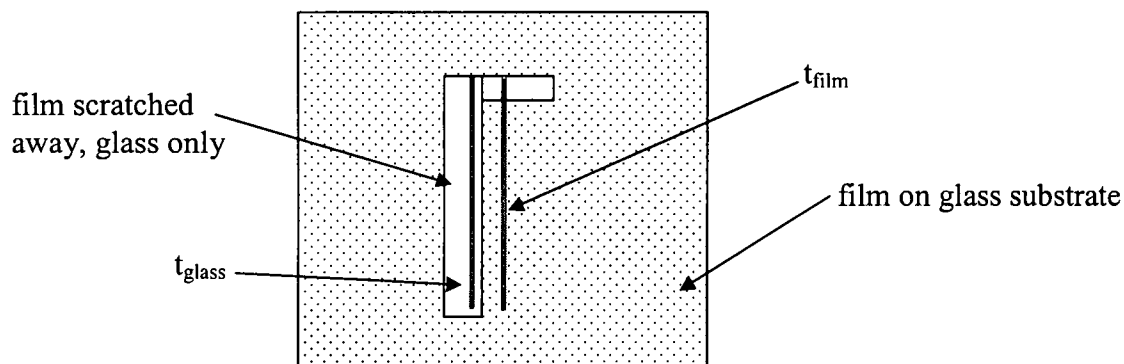


Fig. 4.5. Schematic of profilometer measurement technique to factor out thickness variations in glass substrate. A scratch is made in the film and a scan is taken along the scratch ( $t_{\text{glass}}$ ), and a scan of the film is taken next to the glass ( $t_{\text{film}}$ ). The thickness is found by subtracting  $t_{\text{glass}}$  from  $t_{\text{film}}$ . The film scan is started on glass so that a common reference can be used for the film and glass scans.

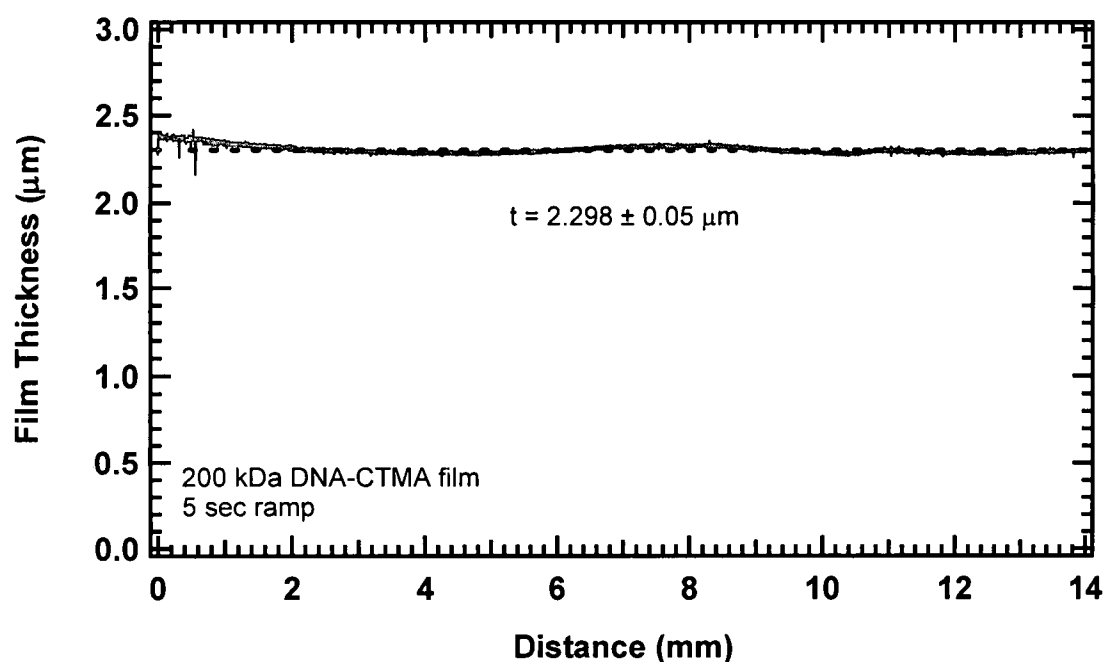


Fig. 4.6. Thickness of 200 kDa DNA-CTMA film with spinning parameters of 1000 rpm for ten seconds with a five second ramp. The best fit line is shown with the slope held to zero.

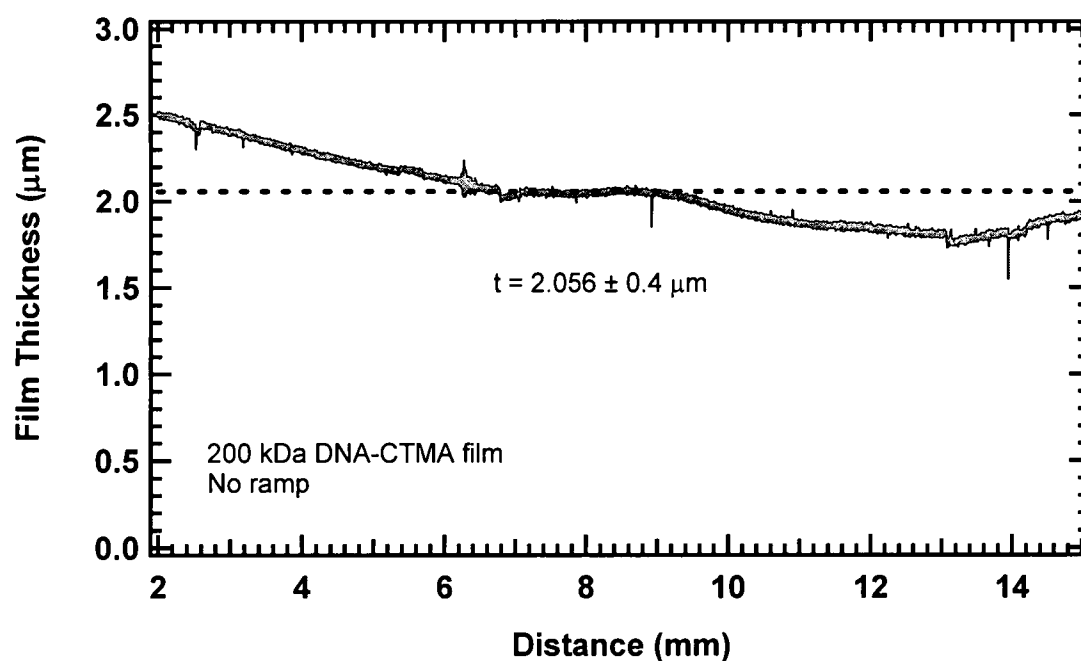


Fig. 4.7. Thickness of 200 kDa DNA-CTMA film with spinning parameters of 1000 rpm for ten seconds with no ramp. The best fit line is shown with the slope held to zero.

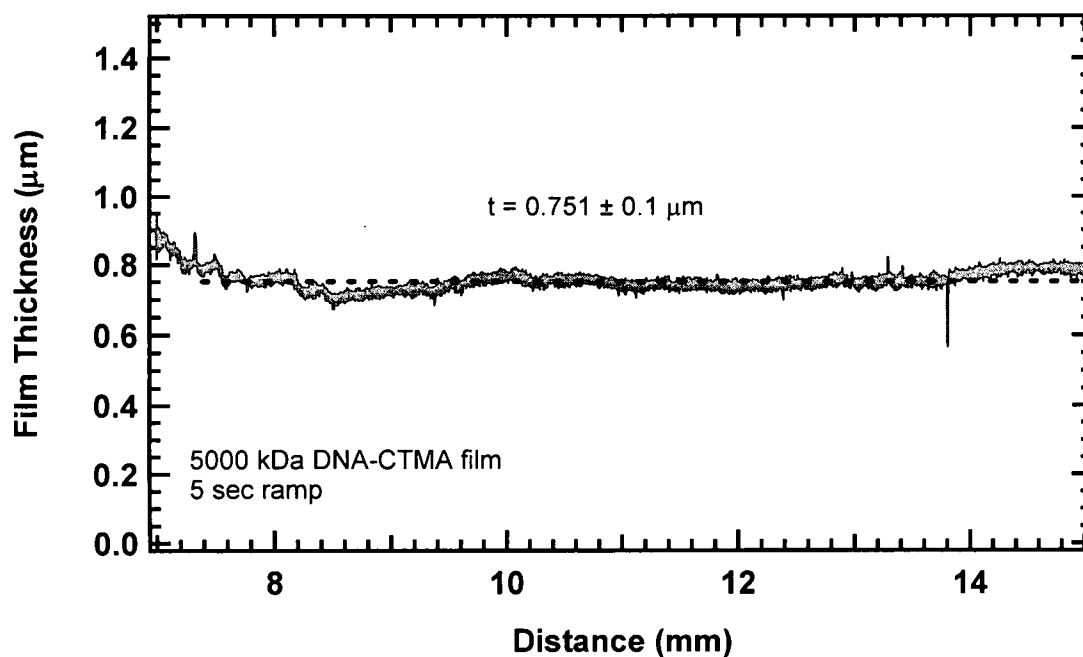


Fig. 4.8. Thickness of 5,000 kDa DNA-CTMA film with spinning parameters of 1000 rpm for ten seconds with a five second ramp. The best fit line is shown with the slope held to zero.

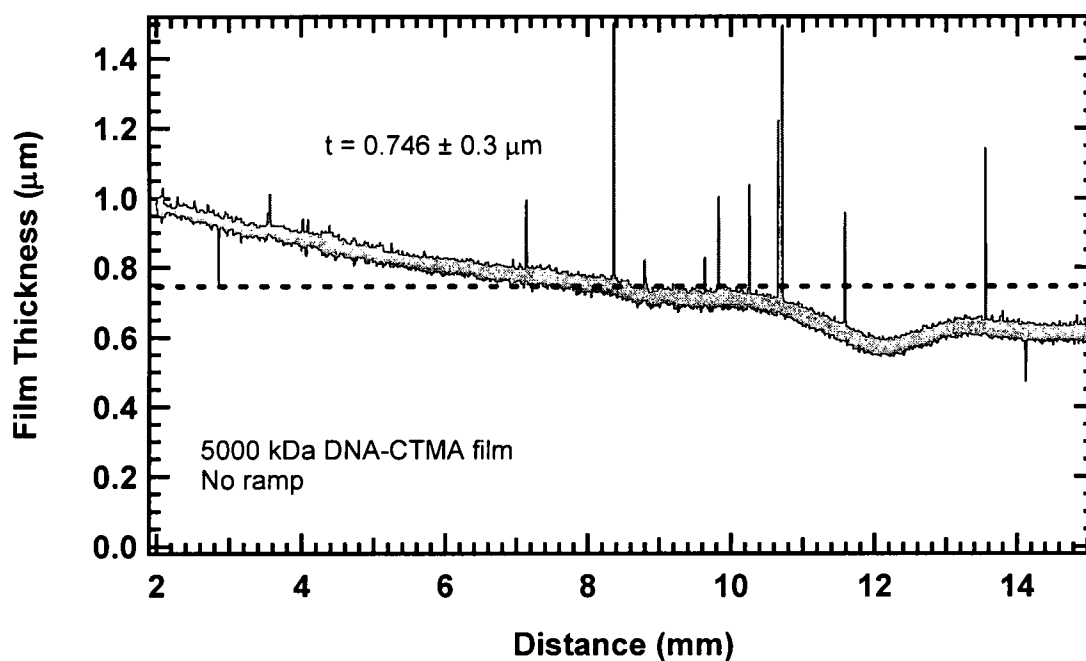


Fig. 4.9. Thickness of 5,000 kDa DNA-CTMA film with spinning parameters of 1000 rpm for ten seconds with no ramp. The best fit line is shown with the slope held to zero.

#### **4.4.2 Noncrosslinked DNA-CTMA Films**

The resulting DNA-CTMA compound is soluble in many of the alcohols including butanol, methanol, ethanol and isopropanol, as well as an alcohol-chloroform blend. To spin-coat a thin film for photonics applications, butanol is the solvent of choice because its slow evaporation due to a high boiling point (116 – 118 °C) ensures a smooth, uniform film during the spin-coating process. Butanol has a density of 0.81 g/mL and was purchased from Aldrich and used without further purification. The amount of solvent used in dissolving the DNA-CTMA is dependent on the molecular weight of the starting DNA. Higher molecular weight (>1000 kDa) DNA forms a more viscous solution than lower molecular weight (<500 kDa) DNA. A greater amount of solvent is, therefore, required for higher molecular weight DNA. For example, for DNA with a starting molecular weight of 8000 kDa, DNA-CTMA is dissolved in butanol at a concentration ranging from 39.8 to 54.2 mM bp<sup>-1</sup>. For a lower molecular weight of 200 kDa, a concentration between 85.0 and 110.0 mM bp<sup>-1</sup> is used.

To make a thin film, DNA-CTMA is dissolved in butanol at a concentration appropriate for its molecular weight. The most common molecular weights used are 500 kDa and 200 kDa. For these lower molecular weights, a solution of 110 mM bp<sup>-1</sup> DNA-CTMA in butanol yields a film thickness of between 2 and 3 μm for spinning parameters of 800 rpm for 10 sec. The solution is mixed in a sealed glass bottle, in a 60 °C oven, using an ATR Rotamix for at least six hours as discussed in Sec. 4.4.1. Once completely dissolved, the solution is filtered through a 0.2 μm pore size syringe filter. Because DNA-CTMA solutions are more viscous at room temperature, the filtering takes place inside a 60 °C oven using a New Era pump systems motorized syringe pump. The

solution is left to sit overnight in a tightly capped container in the 60 °C oven to allow any micro-bubbles induced by filtering to dissipate. It is then spin-coated on to a substrate at a speed of 800 – 1000 rpm for ten seconds with a five second ramp (Sec. 4.4.1). After spinning, the sample is cured in an 80 °C oven for one hour. Table 3.1 provides examples of measured film thickness as a function of DNA molecular weight and DNA-CTMA concentration in solution. These data show that the film thickness is quite sensitive to the DNA-CTMA concentration for a given molecular weight and, as might be expected, higher concentrations are possible with the lower molecular weights.

#### ***4.4.3 Crosslinked DNA-CTMA Films***

The noncrosslinked DNA-CTMA films, while of high optical quality, are soft and scratch easily (a visible mark is left on the film when scratched by a fingernail). This makes them incompatible with more aggressive processing techniques, such as sawing, that are often required to fabricate a photonic device. One solution to this problem is to crosslink the DNA-CTMA films. The crosslinker used in this work is poly(phenyl isocyanate)-co-formaldehyde (PPIF) with a formula weight of 400 g/mol. It was purchased from Aldrich and used without further purification. The resulting crosslinked DNA-CTMA films are significantly harder (the films show no mark when scratched by a fingernail) than the non-crosslinked films, allowing them to withstand more demanding fabrication procedures than non-crosslinked films due to their increased hardness. Crosslinked films are also resistant to a wider range of solvents, including butanol and other alcohols. This allows multi-layer DNA-based structures to be fabricated.

It was found through trial and error that the lowest amount of PPIF that can be used and still crosslink the DNA-CTMA film is 10 wt% (36.1 mol%) PPIF with respect

to DNA-CTMA. However, concentrations of up to 20 wt% (81.2 mol%) can be used. Beyond 20 wt%, optical losses are too high for photonics applications ( $>1$  dB/cm). The addition of the crosslinker significantly increases the refractive index (Sec. 5.3) and this must be taken into consideration when choosing the amount of crosslinker to use. It was also found that the higher concentration of crosslinker more easily crosslinked DNA-CTMA films doped with a chromophore dye, although crosslinking could be achieved with a lower concentration by altering the curing procedure (Sec. 4.4.4).

To prepare a crosslinked DNA-CTMA film, the DNA-CTMA is dissolved in butanol at a concentration appropriate for its molecular weight (Table 4.1). The PPIF crosslinker is dissolved in butanol at a ratio of 1:4, PPIF:Butanol by weight. The DNA-CTMA-butanol solution is mixed in a 60 °C oven for at least six hours as discussed in Sec. 4.4.1. The PPIF-butanol solution is not mixed using the Rotamix, but rather is left standing in the 60 °C oven. After a few hours of standing in the oven, the PPIF is fully dissolved in the butanol. Once fully dissolved, the DNA-CTMA-butanol solution is added to the PPIF-butanol solution and the resulting solution is mixed for an additional two hours in the 60 °C oven. The DNA-CTMA-PPIF solution is then filtered through a 0.2  $\mu\text{m}$  pore size syringe filter to remove any impurities and left to sit overnight in a 60 °C oven to allow any micro-bubbles induced by filtering to dissipate. It is spin-coated onto a substrate using the same spin parameters as the non-crosslinked DNA-CTMA films (Sec. 4.4.2). The substrates are baked in an 80 °C oven for five minutes and then cured in a vacuum oven at 175 °C for 15 min. After curing, the crosslinked films are resistant to butanol and will not be damaged if rubbed with a cotton swab soaked in butanol.

Table 4.1. Film thickness of spin-coated DNA-CTMA films, spin speed was 800 rpm for 10s.

Molecular weight of DNA (kDa) <sup>a</sup>	DNA-CTMA concentration in butanol (mM bp <sup>-1</sup> )	Film Thickness (μm) <sup>b</sup>
8000	54.2	5.0
8000	39.8	2.4
1300	61.6	3.0
1300	46.9	1.3
500	85.0	3.0
500	69.3	1.7
300	101.5	2.0
300	85.0	1.5
200	85.0	2.6

<sup>a</sup> Estimated uncertainty  $\pm 50\%$

<sup>b</sup> Estimated uncertainty  $\pm 0.1 \mu\text{m}$

#### 4.4.4 DNA-CTMA-Chromophore Films

For the core waveguide layer, a chromophore dye is added to the DNA-CTMA-PPIF solution. In this work, the chromophore dye Disperse Red 1 (DR1) is used. DR1 has a formula weight of 314.34 g/mol and was purchased from Sigma-Aldrich and used without further purification.<sup>26</sup> It was chosen because it is inexpensive and has proven success as an EO chromophore.<sup>82</sup> Both crosslinked and noncrosslinked DNA-CTMA-chromophore films were made. Crosslinking a film with chromophore dye was found to be slightly more complicated than crosslinking films without a chromophore dye. The amount of chromophore dye determines both the amount of crosslinker needed and the curing conditions.



For the core layer, an amount between 5 wt% (21.8 mol%) and 10 wt% (45.9 mol%) DR1 with respect to DNA-CTMA was used. The dye was dissolved separately in dioxane at a concentration of 24.6 mM. Dioxane has a density of 1.034 g/mL and was purchased from Sigma-Aldrich and used without further purification. For the lower concentration of chromophore dye, the lower amount of PPIF, 10 wt%, is suitable to achieve crosslinking, however a longer curing time of 20 minutes at 175 °C is required. For the higher concentration of chromophore dye, a higher amount of PPIF, 20 wt%, is required to achieve crosslinking.

To fabricate a DNA-CTMA-chromophore film, DNA-CTMA is dissolved in butanol as previously discussed and an appropriate amount of PPIF is dissolved separately in butanol at a concentration of 1:4, PPIF:Butanol by weight, by being allowed to stand in a 60 °C oven for several hours. Once dissolved, the DNA-CTMA-butanol solution is added to the PPIF-butanol solution and mixed for an additional two hours. The chromophore dye is dissolved separately in dioxane at a concentration of 24.6 mM. The chromophore dye-dioxane solution is then added to the DNA-CTMA-PPIF solution and mixed for an additional hour. The solution is filtered through a 0.2 µm syringe filter and allowed to stand overnight. It is spin-coated and cured in a manner appropriate for the dye concentration as previously discussed.

#### ***4.4.5 Thick Films for Absorption Measurements***

To make absorption measurements as an estimation of waveguide loss it is necessary to have thick films (>100 µm) in order to have accurate measurements (Sec. 5.4.1). These films cannot be fabricated using spin-coating techniques as spin-coating typically can yield thicknesses of only ten microns or less. Casting films in a Teflon

mold is typically the method of choice for fabricating thick films and has been previously used to cast thick DNA-CTMA films.<sup>28</sup> However, we found that the film quality using this method is not suitable for absorption measurements. The film surfaces are textured due to the surface texture of the Teflon mold. This causes increased scattering for absorption measurements.

A technique was developed to produce thick DNA-CTMA films that had little or no surface defects. A viscous solution of the desired film is made and filtered with a 0.2  $\mu\text{m}$  filter. The solution should be as viscous as possible while still being able to be filtered; this concentration is determined through trial and error. The solution is poured onto a microscope cover slide that is in a 40 °C vacuum oven. The film is left to sit overnight or until all of the solvent has evaporated. Once the film is fully cured, a razor blade is used to carefully separate the film from the slide. This leaves a free-standing thick film with smooth surfaces suitable for absorption loss measurements.

## CHAPTER 5

### DNA-CTMA CHARACTERIZATION

Although the properties of DNA have been well-characterized on the molecular level,<sup>83,84</sup> its bulk material properties are still largely undetermined. It is important to characterize the complexed DNA-CTMA bulk material as thoroughly as possible to gain insight into how best to integrate it into an EO waveguide modulator. This analysis begins with the structure and composition of the material. The DNA purified by CIST is reported to have a protein content of two percent.<sup>85</sup> Because this DNA was received from a noncommercial source, it is important to independently confirm these purity reports and to compare them with salmon-derived DNA purchased commercially from Sigma-Aldrich.<sup>26</sup> It is also desirable to have a thorough understanding of the DNA structure within the DNA-CTMA bulk film, specifically whether or not the DNA double helix is preserved in the DNA-CTMA and DNA-CTMA-chromophore films.

Additionally, there are many material properties that need to be determined for successful integration of DNA-CTMA into a waveguide device. These include the thermal properties of DNA-CTMA, the indices of refraction for both crosslinked and noncrosslinked DNA-CTMA films and for DNA-CTMA-chromophore films, the

absorption losses at the communications wavelengths, the resistivities of the films, and the dielectric constant.

### 5.1 DNA Purity

A quick assessment of the purity of DNA samples can be made by determining the ratio of spectrophotometric absorbance of the samples at 260 nm to that of 280 nm. This is referred to as the A260/A280 ratio and is a common molecular biology protocol.<sup>86</sup> A pure DNA preparation is expected to have an A260/A280 ratio of 1.8 while a pure protein sample would have an A260/A280 ratio of 0.57.<sup>86</sup> The A260/A280 ratio is only an indication of purity and is not a precise measure. However, this measurement is useful as a rough indication of purity and a good starting point for characterizing this material. A Cary 500 UV-VIS-NIR spectrophotometer was used for these measurements. Liquid samples were placed in a quartz cuvette and the measurements were taken at room temperature. For comparison, salmon-derived DNA was obtained from Sigma-Aldrich and used without further purification. The exact protein content of the Aldrich DNA was not available, although it is assumed to be low. The DNA samples from CIST and Aldrich were prepared by dissolving the DNA in 14 M $\Omega$ ·cm distilled/deionized water at a concentration of 50  $\mu$ g/mL. The UV absorbance for the CIST and Aldrich DNA samples are shown in Fig. 5.1. The A260/A280 ratios are 1.86 for the CIST DNA and 1.83 for the Aldrich DNA. This implies that both samples have relatively low protein content and leaves no reason to doubt the reported protein content by CIST.

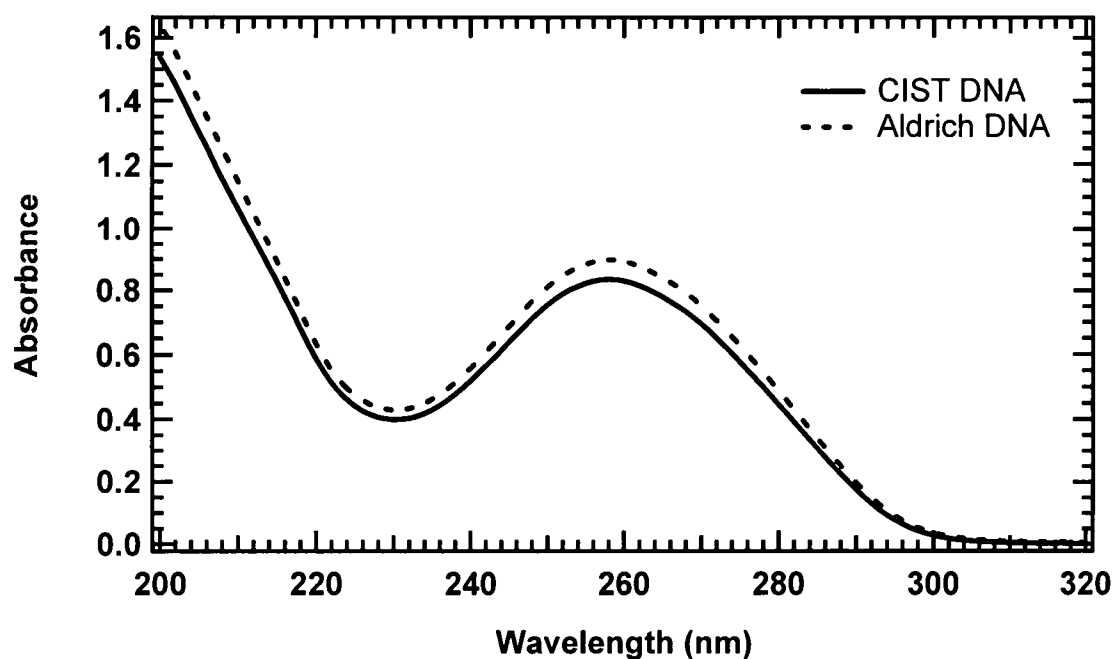


Figure 5.1. Absorbance of DNA from CIST and Aldrich. DNA samples are dissolved in water at a concentration of 50  $\mu\text{g/mL}$ . The  $A_{260}/A_{280}$  ratio is 1.86 for the CIST DNA and 1.83 for the Aldrich DNA.

## 5.2 DNA-CTMA Structure

Circular dichroism (CD) and absorption measurements at 260 nm were used to determine if the double helical structure of DNA is preserved in the complexed DNA-CTMA material.<sup>87,88</sup> CD measurements confirmed that a DNA-CTMA solution does, in fact, retain its double helical structure at room temperature. Absorption measurements were used to determine the temperature at which the double helix of DNA-CTMA in solution separates, called the denaturation temperature. If the CD spectra confirms that the double helix is in tact for DNA-CTMA in solution at room temperature, and if the absorption measurements show that the denaturation temperature of DNA-CTMA in

solution is higher than the temperatures to which the DNA-CTMA is exposed during film processing, the conclusion that the double helix is intact for DNA-CTMA films could be made.

The double helical form of DNA is a chiral molecule, a molecule with molecular asymmetry that is not identical to its mirror image. A way of characterizing chiral structures is through their interactions with polarized light. CD refers to the difference in absorption of left- and right-circularly polarized light.<sup>87,88</sup> A CD spectrum is only present for samples that exhibit molecular asymmetry; for symmetric molecules there is no difference in the absorption of left- and right-circularly polarized light. Because double helical DNA is a chiral molecule, it exhibits a very distinctive CD spectrum.

The CD measurements were taken using a Jasco model J-720 spectropolarimeter. The DNA-CTMA was dissolved in butanol at a concentration of 26.0 mM. This concentration was found by trial and error to be the highest concentration that could be used without overloading the spectropolarimeter detector. The absorption measurements were taken using a Cary 100 Bio UV-Visible Spectrophotometer. The liquid samples were placed into a quartz cuvette and the temperature was controlled with a Peltier device connected to Varian Bio-Melt software. The temperature was controlled by the software and is increased by 5 °C every two minutes, with a 30 sec wait time at each temperature before each measurement. The sample concentrations were 50 µg/mL for aqueous DNA measurements and 34 mg/mL for DNA-CTMA in butanol. The absorption measurements were performed by UES, Incorporated, which is a contractor to AFRL at WPAFB.

A CD spectrum was taken at room temperature of DNA-CTMA in butanol and was shown to exhibit the same characteristics as a CD spectrum of aqueous DNA,

although it is shifted slightly.<sup>87,88</sup> This shift is most likely due to the addition of the CTMA molecules on the DNA chain. This spectrum implies that DNA-CTMA retains the double helical structure of DNA at room temperature. The CD spectra of DNA-CTMA in butanol and DNA in water for room temperature are shown in Fig. 5.2.

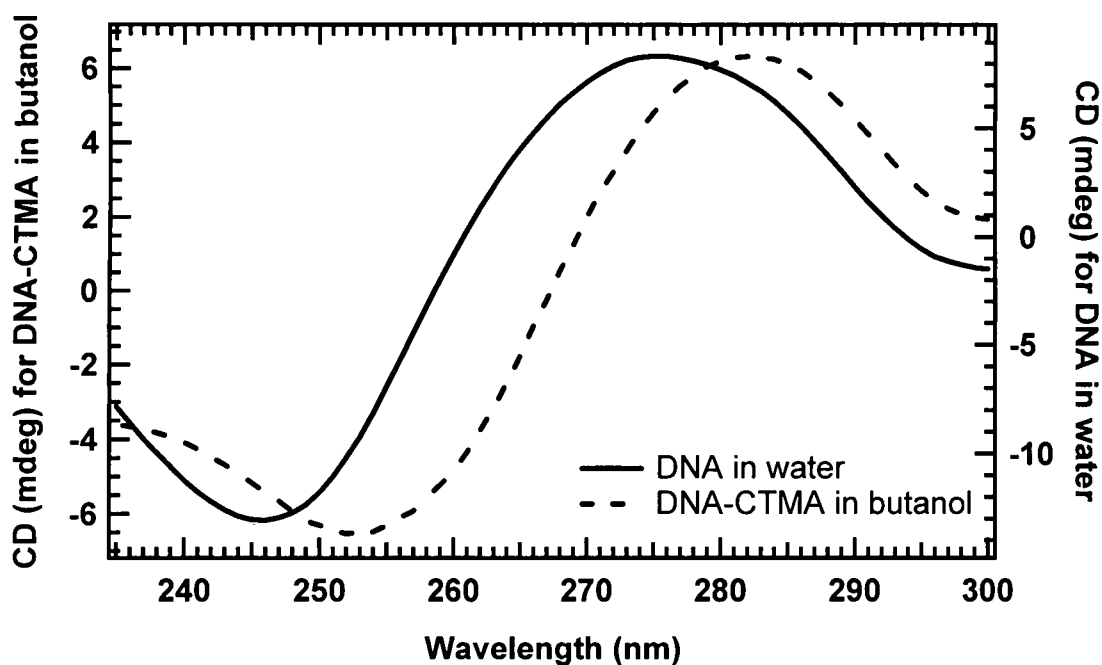


Fig. 5.2. CD spectra of DNA in water and DNA-CTMA in butanol at room temperature. DNA-CTMA shows the peaks characteristic of DNA, although they are shifted slightly due to the addition of CTMA to the DNA chain. This suggests the helix is intact in the DNA-CTMA butanol solution. The CD signal strength is different for each sample due to differences in concentration.

An absorption scan at 260 nm as a function of temperature was used to determine the denaturation temperature of the complexed DNA-CTMA. Denaturation describes the collapse of the DNA double-helical structure and is accompanied by the separation of the duplex into its single strands. This occurs when the DNA in an aqueous solution has been heated to  $\sim 90\text{--}95^\circ\text{C}$ .<sup>64</sup> The wavelength of maximum absorption for aqueous DNA is 260 nm, as seen in the DNA UV absorbance spectrum in Fig. 5.1. At this wavelength, the absorption by single-stranded DNA is  $\sim 40\%$  higher than by double-stranded DNA.<sup>64</sup> This increase in absorption results from the unstacking of the base pairs in the helix and is referred to as the hyperchromic effect.<sup>64</sup> By monitoring the 260 nm absorption while the temperature of the DNA solution is gradually increased, the change from double-stranded DNA to the denatured form can be observed. Such a curve is referred to as a melting curve; the temperature at which 50% melting has occurred is called the melting temperature  $T_m$  of DNA. Common melting curves from different DNA species are shown in Fig. 5.3.

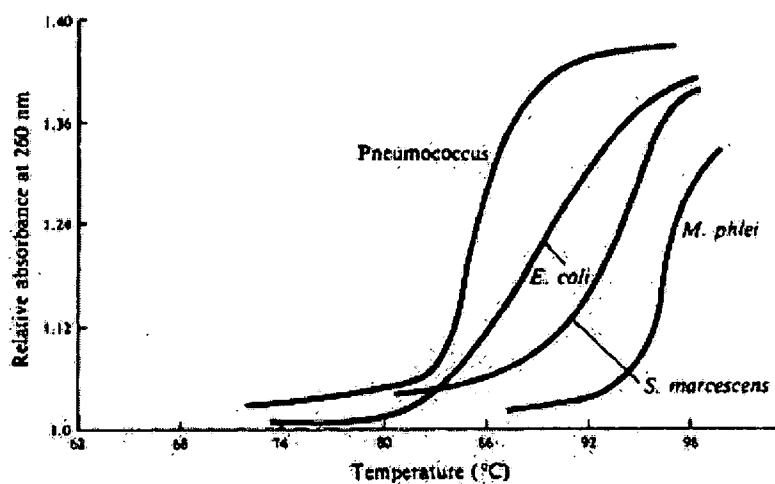


Fig 5.3. Melting curves for DNA from different species.  
[From Reference No. 64]



Figure 5.4 shows the melting curve at 260 nm for the DNA received from CIST for both aqueous DNA and complexed DNA-CTMA in butanol. The absorption spectrum of the aqueous DNA received from CIST shows the expected increase in absorption centered around 90 °C, confirming its expected denaturation temperature. The absorption spectrum for DNA-CTMA dissolved in butanol does not, however, show a substantial increase in absorption even up to 100 °C (the high temperature limit for the instrument). This implies that the denaturing temperature for complexed DNA-CTMA is greater than 100 °C.

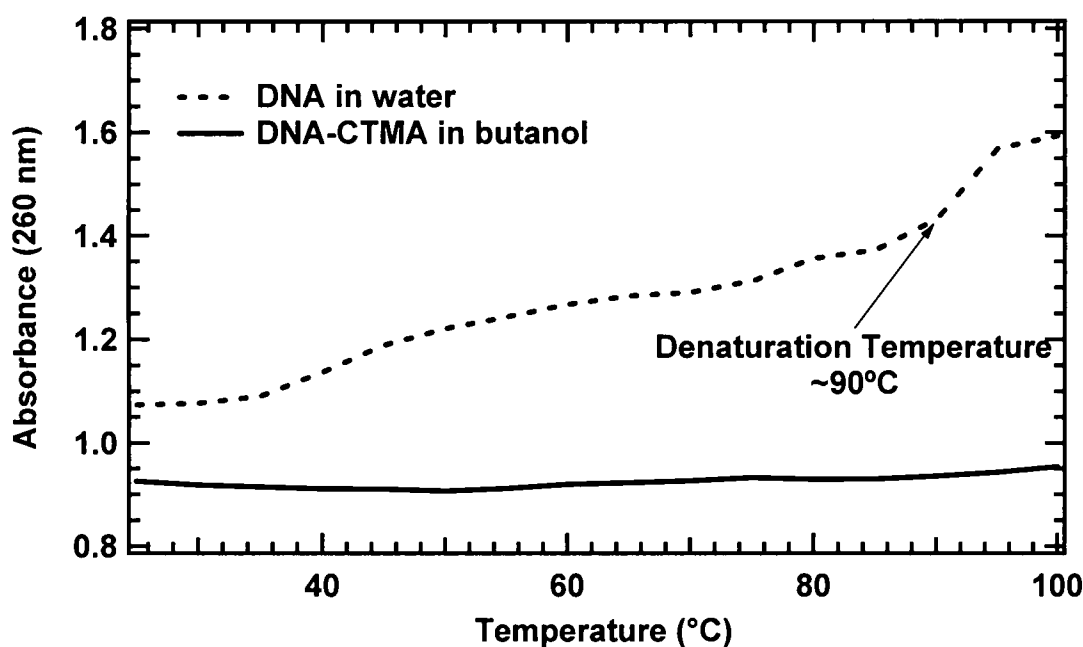


Fig. 5.4. Melting curves of DNA in water and complexed DNA-CTMA in butanol. Denaturation temperature of DNA in water is ~90°C, the denaturation temperature of DNA-CTMA is >100°C.

The CD data confirm that the helix is preserved for the DNA-CTMA solution at room temperature, and the 260 nm absorption data indicate that it remains preserved for temperatures  $>100^{\circ}\text{C}$ . It is unknown whether or not the helix is intact for a cured DNA-CTMA film. However, because the noncrosslinked DNA-CTMA films are fully cured at  $80^{\circ}\text{C}$ , well below  $100^{\circ}\text{C}$ , it can be concluded that the double helix also remains intact in the cured, noncrosslinked DNA-CTMA films. Even though the crosslinked films are fully cured at temperatures greater than  $100^{\circ}\text{C}$ , the solvent is completely removed at  $80^{\circ}\text{C}$ . It is therefore reasonable to conclude that the double helix is also intact for crosslinked DNA-CTMA films. A more detailed structural analysis is needed to fully confirm this supposition.

### 5.3 Index of Refraction

The index of refraction was measured with the Metricon 2010 Prism Coupler. The sample to be measured is brought into contact with the base of a prism by means of a pneumatically-operated coupling head, which creates a small air gap between the film and the prism. A laser beam (632.8 nm, 1152 nm, or 1523 nm) strikes the base of the prism and is totally internally reflected at the prism base onto a photodetector. At certain discrete values of the incident angle, photons can tunnel across the air gap into the film and enter into a guided optical propagation mode. This causes a sharp drop in the intensity of light reaching the detector. The film index is determined by the angular location of the first mode. A DNA-CTMA film is spin-coated onto a Si wafer. The indices of refraction of the film were measured at the three available wavelengths. A Cauchy fit to these data was used to plot the dispersion. The Metricon can also provide the film thickness when three or more modes are recorded. It is important that the film be

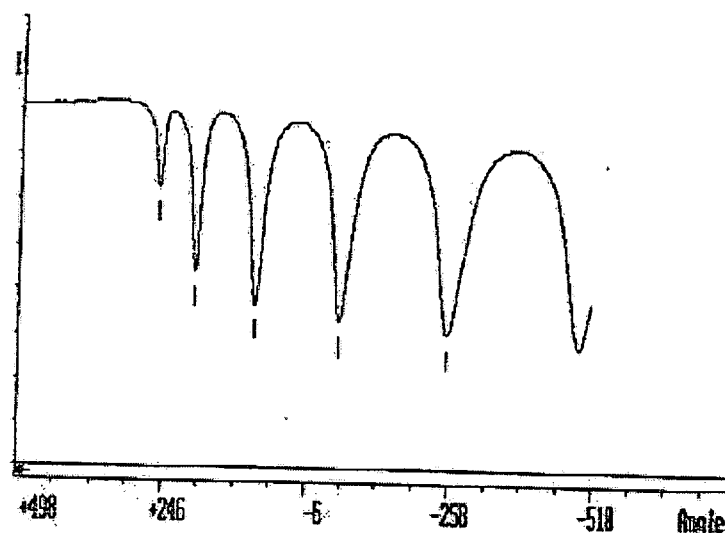
kept in the same location for each measurement as there can be slight variations in thickness and film quality across the surface.

An example of an index measurement using the Metricon for a DNA-based film is shown in Fig. 5.5. The sharp dips indicate the angular locations of the coupled modes for the film. Based on these positions (indicated with a vertical line directly underneath the dip), the computer calculates the film index and thickness that are the best fit to the data. For the example shown in Fig. 5.5, the film measured was a crosslinked DNA-CTMA-DR1 film with 20 wt% PPIF and 3 wt% DR1. It was measured at 632.8 nm and an index  $n = 1.5576$  and a thickness  $t = 2.9681$  were calculated. Fitting uncertainties are also provided. For this example, the standard deviation in fit of the index measurement is 0.00%, and the standard deviation to the fit of the thickness measurement is 0.18%.

Although three modes are needed to calculate both the index and the thickness; five modes are preferred for the increased accuracy. If only two modes are detected, a range of possible index and thickness pairs are generated and it is usually possible to determine the correct pairing based on a measurement at a different wavelength or prior knowledge of the film. If only one mode is detected, the user must input either the thickness or index, and from that information the other variable can be calculated.

The indices of refraction were measured for noncrosslinked DNA-CTMA for three different molecular weights (200 kDa, 500 kDa, and 5,000 kDa) and are shown with a Cauchy fit in Fig. 5.6. Within experimental uncertainty, there is no appreciable difference in the indices as a function of molecular weight. The indices were measured to be  $n(\lambda=632.8\text{nm}) = 1.5153 \pm 0.0002$ ,  $n(\lambda=1152\text{nm}) = 1.5053 \pm 0.0003$ , and  $n(\lambda=1523\text{nm}) = 1.5029 \pm 0.0004$ .

The addition of the PPIF crosslinker raises the index of refraction as does the addition of a chromophore dye. A summary of the indices for films with varying concentrations of PPIF and DR1 are shown in Table 5.1. As seen in Table 5.1, there are many possible core and cladding material combinations that provide an index difference of at least 0.02, which is required for waveguiding.



ID= XL(20%)-DR1(3%)	03-23-2005 12:02	Rel 34
Prism= 1030	Substrate N= 3.5	Data= 498 to -502
Wavelength= 632.8	Prism N= 1.9648	
+259 (1.5541)	+194 (1.5436)	+88 (1.5263)
-250 (1.4691)	-61 (1.5015)	
Off	n	SD
>> 0	1.5576	0.0000
1	1.5635	0.0008
	SD	XS
	2.9681	0.0053
	3.6202	0.1521
	SD	XS
	0.0053	0.18
	0.1521	4.20

Fig. 5.5. Metriton index data for a DNA-CTMA film with 20 wt% PPIF and 3 wt% DR1.

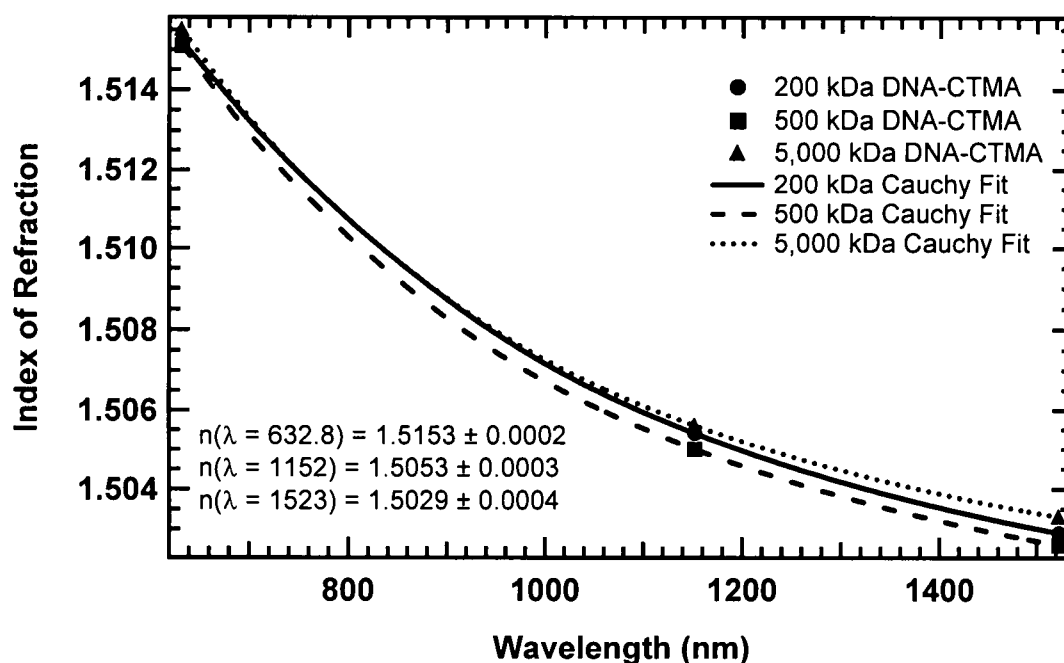


Fig. 5.6. Index of refraction with Cauchy fit of DNA-CTMA for three different molecular weights. Within experimental uncertainty, there is no appreciable change in index with molecular weight.

Table 5.1. Refractive indices of various DNA-CTMA (DC) core and cladding materials. Crosslinker is PPIF and DR1 is the chromophore dye. The numbers in subscripts are the amounts of each substance in wt% with respect to DNA-CTMA. The indices listed at 633 nm, 1152 nm, and 1523 nm are measured values, while the indices listed at 690 nm and 1300 nm are found from a Cauchy fit to the measured values. Also listed are APC and PMMA, materials that could be used as a buffer layer.

Material	Use	n (633 nm)	n (690 nm)	n (1152 nm)	n (1300 nm)	n (1523 nm)
DC	Clad	1.5152	1.5135	1.5054	1.5042	1.5029
DC-PPIF <sub>10</sub>	Clad	1.5326	1.5292	1.5201	1.5191	1.5181
DC-PPIF <sub>15</sub>	Clad	1.5353	1.5325	1.5225	1.5212	1.5199
DC-PPIF <sub>10</sub> -DR1 <sub>4</sub>	Core	1.5597	1.5526	1.5350	1.5335	1.5321
DC-PPIF <sub>10</sub> -DR1 <sub>5</sub>	Core	1.5536	1.5476	1.5292	1.5272	1.5252
DC-PPIF <sub>20</sub> -DR1 <sub>5</sub>	Core	1.5702	1.5637	1.5452	1.5433	1.5415
DC-PPIF <sub>20</sub> -DR1 <sub>3</sub>	Core	1.5587	1.5544	1.5390	1.5370	1.5350
PMMA	Buffer	1.4896	1.4881	1.4840	1.4836	1.4832
APC	Buffer	1.5697	1.5662	1.5548	1.5534	1.5521

## 5.4 Waveguide Loss

### 5.4.1 Absorption Loss

A Hitachi model 4001 UV-VIS spectrophotometer was used to measure the optical absorption loss for a thick ( $>100\text{ }\mu\text{m}$ ) noncrosslinked DNA-CTMA film over a wavelength range of 400 – 1600 nm. The thick DNA-CTMA free-standing film used for the transmission measurement was made by slowly evaporating a DNA-CTMA-butanol solution in a Teflon mold in a  $40\text{ }^{\circ}\text{C}$  vacuum oven. The film thickness was measured using a micrometer. This technique could not be used to measure the absorption loss for a crosslinked DNA-CTMA film due to excessive cracking of the thick crosslinked films.

The scattering losses at the film-air interfaces are similar to the film absorption for the thick ( $>100\text{ }\mu\text{m}$ ) films. This suggests that the internal film transmittance for these films can be estimated by adjusting the peak transmittance (minimum loss) regions of the corrected spectrum where there is no evident absorption structure to be  $\sim 100\%$  transmittance ( $\sim 0\text{ dB/cm loss}$ ).<sup>73</sup> By shifting the spectrum slightly to near-zero loss to remove the estimated scattering and interface losses of the specimen, the minimum possible loss that can be expected for a given wavelength can be calculated.

The absorption loss for a noncrosslinked DNA-CTMA film is shown in Fig. 5.7. The film was measured to be  $\sim 356\text{ }\mu\text{m}$  thick. The spectrum was shifted slightly to zero loss at  $\sim 790\text{ nm}$ . The loss was found to be  $<1\text{ dB/cm}$  at the communications wavelengths:  $0.1\text{ dB/cm}$  at  $800\text{ nm}$ ,  $0.2\text{ dB/cm}$  at  $1300\text{ nm}$ , and  $0.7\text{ dB/cm}$  at  $1550\text{ nm}$ . This shows that the conventional criterion that the loss for waveguide applications be  $\leq 1\text{ dB/cm}$  at the communications wavelengths is met. The loss was also calculated at  $690$

nm because of the many measurements taken at this wavelength and was found to be 1.2 dB/cm.

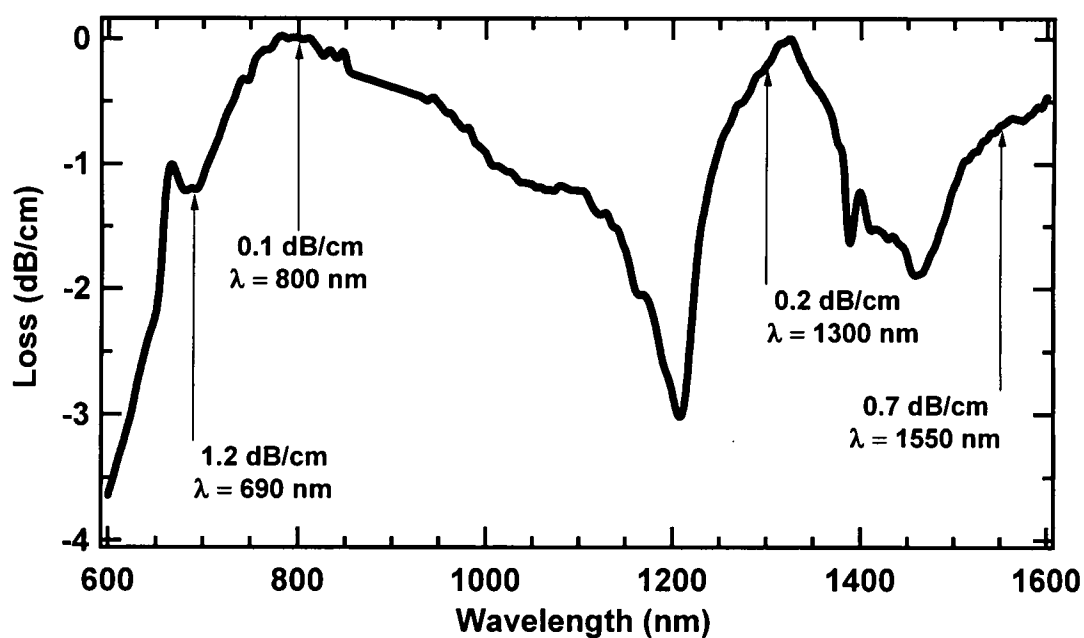


Fig. 5.7. Absorption loss spectrum of a 356  $\mu\text{m}$  thick film of noncrosslinked DNA-CTMA. The losses at the communications wavelengths are shown to be  $< 1$  dB/cm.

### 5.4.2 Waveguide Loss

Optical waveguide losses (scattering and absorption losses) were measured at 690 nm for single-layer noncrosslinked and crosslinked DNA-CTMA films. The film was spin-coated on an SiO<sub>2</sub>-coated Si substrate and served as the core layer of a one-dimensional waveguide with SiO<sub>2</sub> ( $n = 1.46$  at 690 nm) and air ( $n=1$ ) as the bottom and top cladding layers, respectively. Light was coupled into the films using the prism coupling method (Sec. 3.6), and the streak propagating through the waveguide was captured with a Sony Cybershot DSC-P93 5.1 Mpixel digital camera. The camera has a linear response over the pixel range. Calibration of the streak is achieved by placing a ruler directly over the streak and recording a photo of the ruler with the camera in the exact position it was in when the streak was recorded.

The data were analyzed using the image-processing package in Igor Pro.<sup>89</sup> Both the image of the streak and the image of the ruler were first converted from a color image to gray-scale. The image of the ruler was used to calculate the number of pixels/cm. Figure 5.8 shows a photo of the ruler, and Fig. 5.9 shows part of the corresponding cross-section used to calculate the dispersion. Using this dispersion value, a cross-section of the streak image was plotted as a function of distance in cm. The data were smoothed and then converted to dB by taking 10 times the log of the streak data. The slope of the linear fit to these data gives the loss of the film in dB/cm. This loss value contains the total waveguide losses – losses from absorption, scattering, and from the wings of the propagating mode(s) into the cladding layers (which depends on the cladding materials and the index difference).





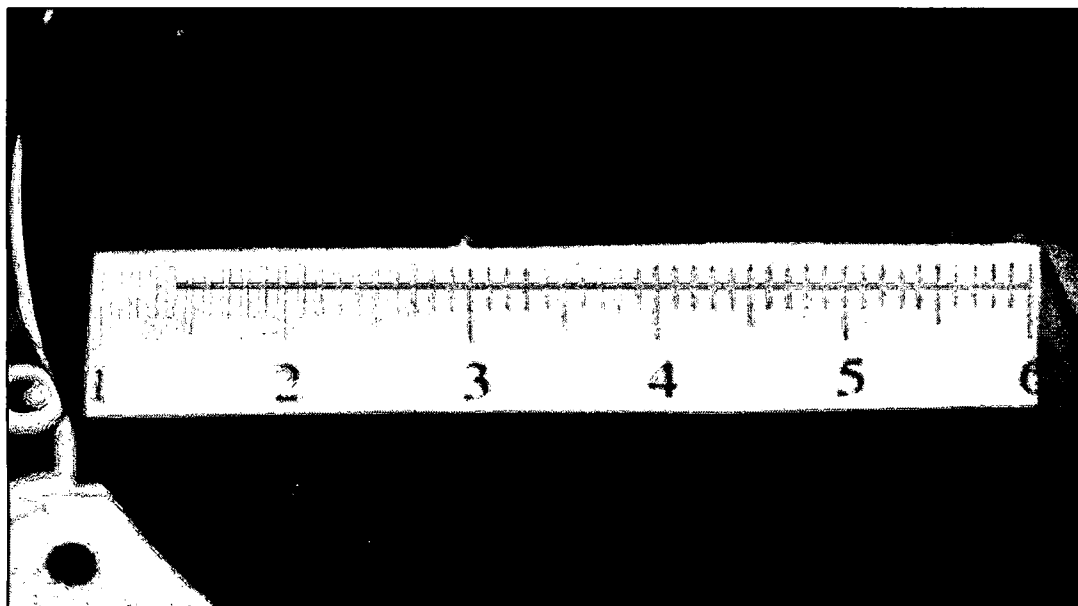


Fig. 5.8. Photo of the ruler used to calculate the dispersion in pixels/cm. The line indicates the location of the cross-section used for the calculation.

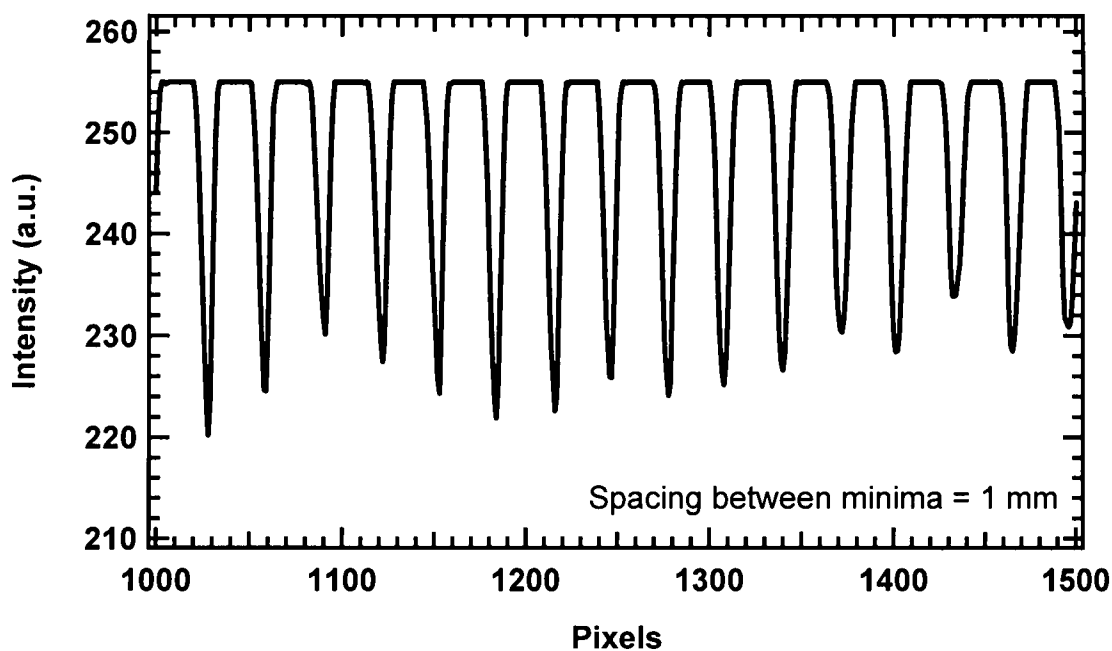


Fig. 5.9. Graph corresponding to Fig. 5.8 of the tick marks of the ruler. Each minima represents the location of a tick mark and the spacing between each minima is 1 mm. This allows the image to be calibrated in terms of cm.

The waveguide loss was calculated for a noncrosslinked DNA-CTMA film and for three crosslinked DNA-CTMA films with varying concentrations of crosslinker: 10 wt%, 15 wt% and 20 wt% PPIF. The losses for these films at 690 nm are shown in Table 5.2. As expected, the loss increases with increasing concentration of crosslinker. The loss data for each film is shown in Figs. 5.10-5.13. The loss for the noncrosslinked DNA-CTMA was calculated to be  $1.25 \text{ dB/cm} \pm 10\%$ . The absorption loss in Fig. 5.7 shows an absorption loss of  $1.2 \text{ dB/cm}$  at 690 nm for a noncrosslinked DNA-CTMA film. This indicates that our background estimate for the transmission was reasonable, as one would expect the loss from the propagation streak to be higher than the transmission loss because of the increased scattering loss in the waveguides. Although the losses are  $>1 \text{ dB/cm}$ , these values are for measurements at 690 nm, where higher loss is expected. At 690 nm, the crosslinked films show a loss increase of  $\sim 20\%$  and  $\sim 40\%$ , respectively, for the 10 wt% and 15 wt% PPIF films compared to the noncrosslinked film. Assuming the same percentage increase of loss at the communications wavelengths (where for the noncrosslinked film the loss was  $0.2 \text{ dB/cm}$  at 1300 nm and  $0.7 \text{ dB/cm}$  at 1550), the absorption and scattering losses in these materials should be sufficiently low at the communications wavelengths.

Table 5.2. Waveguide loss for varying concentrations of PPIF crosslinker in DNA-CTMA films.

Amount of PPIF crosslinker (wt%)	Amount of PPIF crosslinker (mol%)	Waveguide Loss (dB/cm)
0	0	$1.25 \pm 0.008$
10	36.1	$1.48 \pm 0.024$
15	57.3	$1.79 \pm 0.015$
20	81.2	$3.08 \pm 0.017$

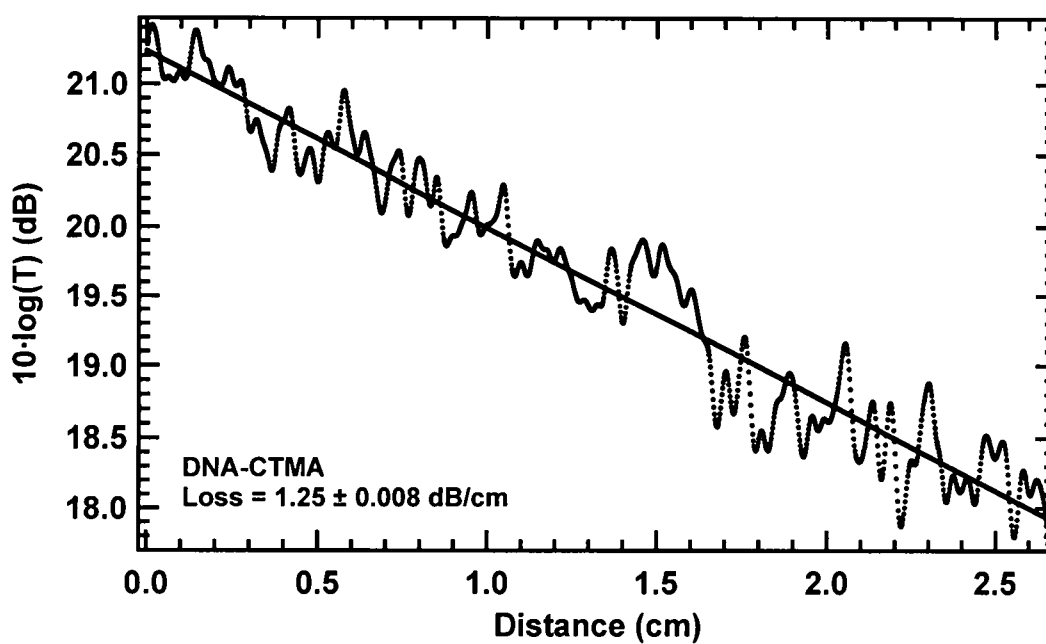


Fig. 5.10. Noncrosslinked DNA-CTMA loss data with fit at 690 nm.

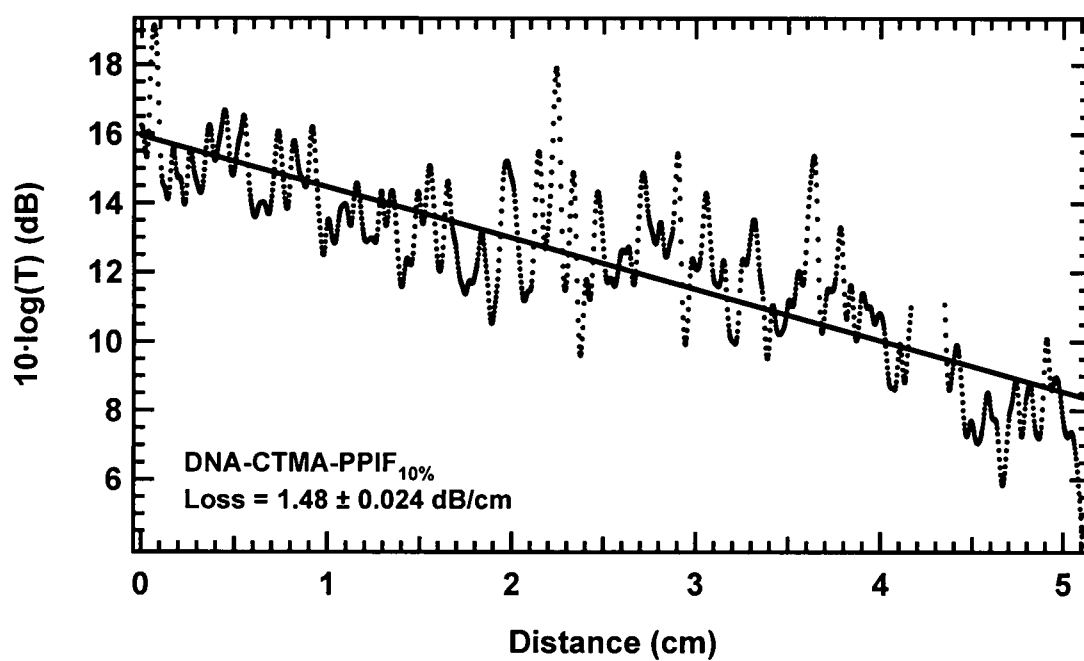


Fig. 5.11. Crosslinked DNA-CTMA loss data with fit at 690 nm for 10 wt% PPIF.

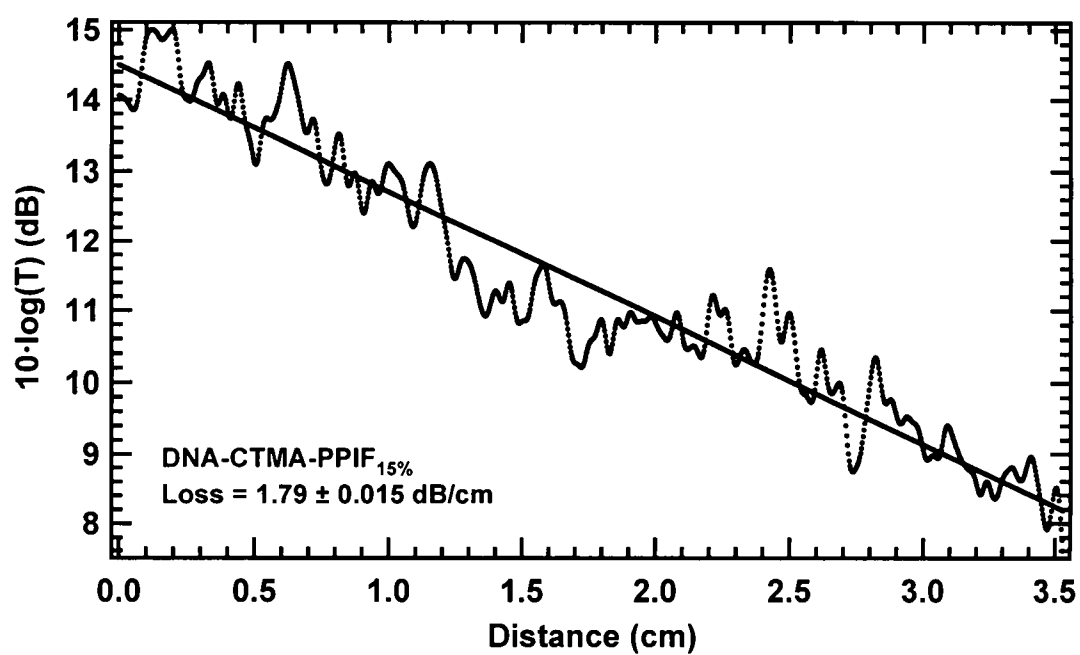


Fig. 5.12. Crosslinked DNA-CTMA loss data with fit at 690 nm for 15 wt% PPIF.

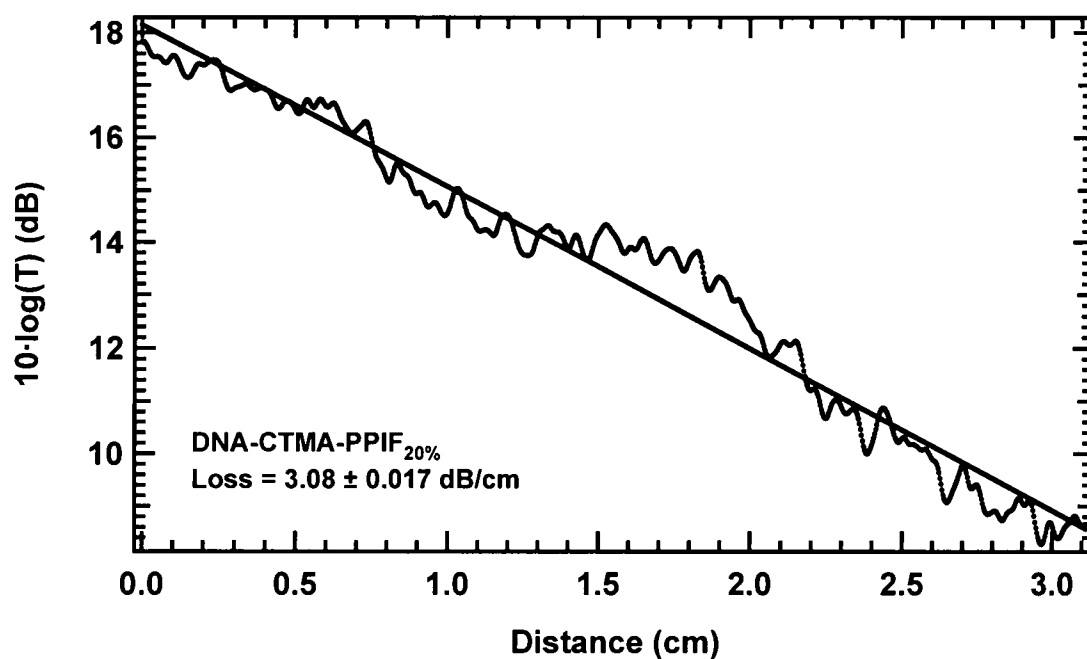


Fig. 5.13. Crosslinked DNA-CTMA loss data with fit at 690 nm for 20 wt% PPIF.

## 5.5 Thermal Studies

Thermogravimetric analysis (TGA) and differential scanning calorimetry (DSC) were used to characterize the thermal properties of DNA in its various forms. The materials analyzed were: 1) unprecipitated DNA (the raw material received from CIST); 2) DNA-CTMA powder; 3) a DNA-CTMA film; and 4) a crosslinked DNA-CTMA film. TGA was used to determine the thermal stability of the materials, and DSC was used to determine the glass-transition temperature  $T_g$  of the materials. All measurements were performed by the Polymers Division (MLBP) within the Materials and Manufacturing Directorate of the Air Force Research Laboratory at Wright-Patterson AFB, Ohio.

### 5.5.1 Thermogravimetric Analysis (TGA)

TGA monitors the weight of a material as a function of temperature.<sup>90,91</sup> A sharp drop in weight indicates the evaporation or burning of a component of the material. For these measurements, the sample was placed in a crucible and heated at a rate of 10 °C/min. The TGA curves for the four DNA materials are shown in Fig. 5.14. The materials show no sharp change in weight up to 200 °C, suggesting that they are thermally stable and suitable for device operation up to this temperature.

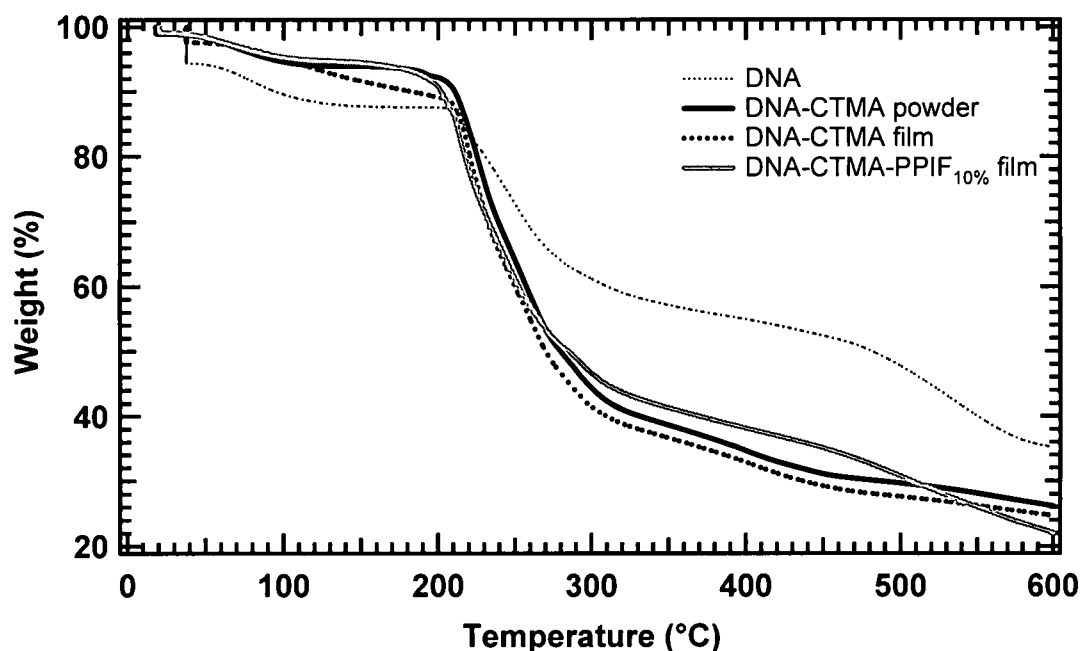


Fig. 5.14. TGA curves for DNA specimens. There is no appreciable weight loss up to 200 °C, indicating these materials are thermally stable up to this temperature.

### 5.5.2 Differential Scanning Calorimetry (DSC)

DSC is the typical method used for determining the thermal transitions of a polymer, including its  $T_g$ .<sup>90-92</sup> In a DSC measurement, there are two pans that are heated at the same rate: one is a reference pan and the other contains the sample. The heating rate is monitored by a computer to ensure the rates remain the same at all times. A shift in the heat flow of the polymer indicates the polymer has reached its glass transition temperature. The heating rate for all samples was 10 °C/min. The DSC results are shown in Fig. 5.15. A glass transition temperature of 148.17 °C was detected for the DNA-CTMA *powder*; however, a clear  $T_g$  could not be detected for the DNA-CTMA *film* or for the other samples. The lack of a  $T_g$  for the DNA-CTMA films has major implications on the poling technique and will be discussed in Chapter 6.

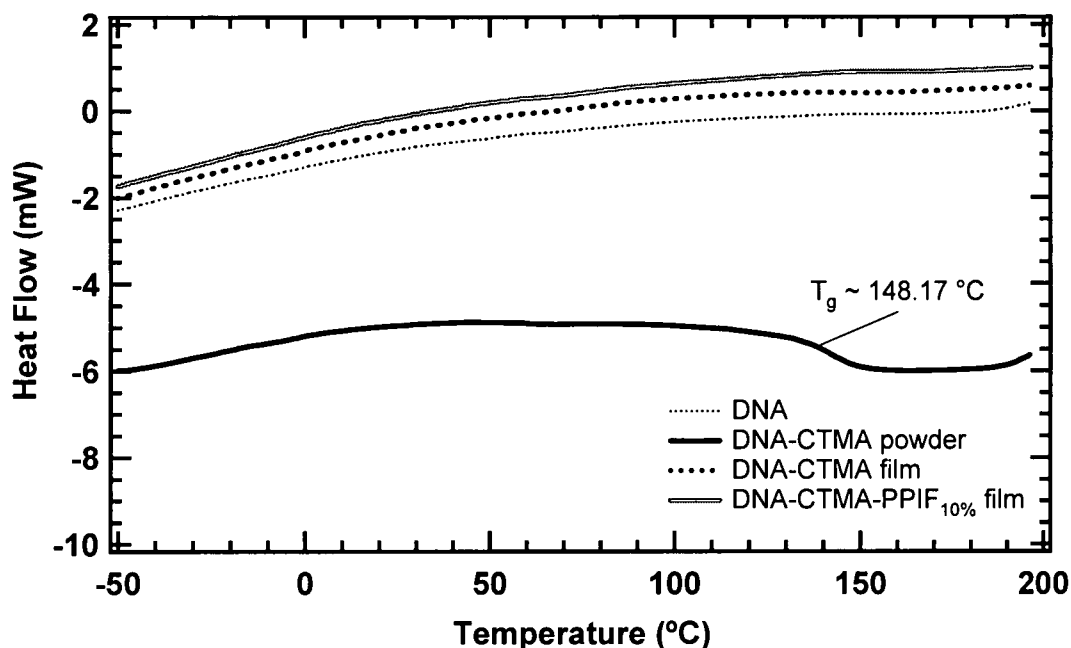


Fig. 5.15. DSC curves for DNA specimens. The DNA-CTMA powder has a  $T_g$  of 148.17 °C; however, a clear  $T_g$  could not be detected for the other materials.



## 5.6 Resistivity

The straight-forward approach to measuring the volume resistivity is to sandwich a film between two electrodes and measure the current through the sandwich for an applied voltage. This technique, which works reasonably well for resistivities below  $10^{12} \Omega\cdot\text{cm}$ , but becomes complicated for higher resistivities due to a combination of background currents from a variety of sources.<sup>93</sup> These background currents can include piezoelectric and electrical discharging effects, although the sources are not easily identified.<sup>93</sup> Additionally, environmental effects such as humidity and temperature can greatly influence the measurement, although performing the measurements in a dry environment can greatly reduce the effects of the former. For high resistivity materials ( $>10^{12} \Omega\cdot\text{cm}$ ) these factors can make it difficult to obtain reproducible, day-to-day results.

To combat these problems, an alternating polarity technique was used to measure the resistivities of a crosslinked DNA-CTMA film and a crosslinked DNA-CTMA-DR1 film.<sup>73</sup> Additionally, a guarded electrode configuration was used to remove the effects of surface resistance.<sup>94</sup> It is important that the top and bottom electrodes be made of the same material in order to minimize asymmetry in the current-voltage curve of the specimen. Gold was used for both electrodes because of its inertness. The guarded electrodes used were fabricated by initially coating a glass microscope slide with 500 Å of gold. The lower circular guarded electrode of diameter  $D = 12 \text{ mm}$  was patterned by the photoresist method. The large 12-mm diameter guarded electrode was chosen because it allows a large gap between the guard and guarded electrodes.<sup>94</sup> This is a necessary consideration for practical fabrication procedures. The guard electrode is spaced by a gap  $g = 1 \text{ mm}$  from the guarded electrode. It is connected to ground for

volume resistivity measurements. The DNA-based film is spin-coated on top of the patterned electrode and a 500 Å gold electrode is deposited on top of the film. A schematic of the guarded electrode configuration is shown in Fig. 5.16.

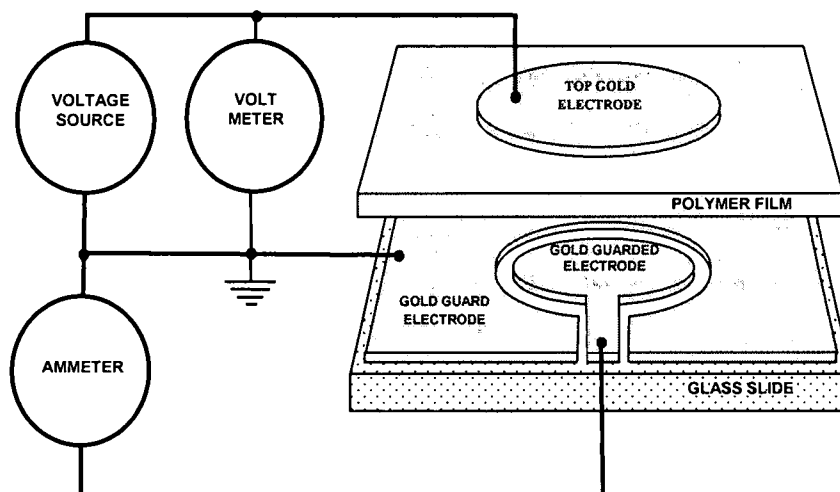


Fig. 5.16. Expanded view of the electrode configuration connected for volume resistivity measurements using a guarded electrode. Contacts are made with probes by scratching away the polymer near the top electrode to contact the guard electrode and at the tab that connects to the guarded electrode. [From Reference No. 73].

The ammeter is connected between ground and the guarded electrode, which makes the guarded electrode essentially at ground potential. For volume resistivity measurements, the upper electrode is connected to the high side of the power supply. Since the guarded electrode is virtually at ground potential, no current flows between the guarded and guard electrodes. The only stimulating current is that which flows through the volume of the polymer. By moving the power supply lead to the guard electrode and the ground lead to the top electrode, the surface resistivity can be measured. This

connection gives a zero potential across the thickness of the film, and the measured current is across the surface in the 1 mm gap between the guarded electrode and the guard electrode. The volume and surface resistivities,  $\rho_v$  and  $\rho_s$ , are calculated using the electrode scheme in Fig. 5.16 with the equations given in Eq. (5.1).

$$\rho_v = R \frac{\pi}{4t^2} D^2 \text{ ohm} \cdot \text{cm} \quad \text{and} \quad \rho_s = R \frac{\pi(D+g)}{g} \text{ ohm/square} \quad (5.1)$$

where  $R$  is the measured resistance,  $D$  is the diameter of the circular electrode,  $t$  is the film thickness and  $g$  is the gap between the circular guard and guarded electrodes. It should be noted here that accurate determination of the film thickness is a significant requirement for reproducible measurements of resistivity. Accurate thickness data were obtained with a Veeco Dektak profilometer, which has often revealed variations in thickness across the electrode of a specimen as the source of poor reproducibility.

The Keithley 617 programmable electrometer used in this work can measure the current  $I$  due to an applied voltage  $V$  from a separate power supply, it can measure resistance directly using a small internally fixed voltage (ohmmeter function) or it can measure the resistance by measuring  $V/I$  using its internal power supply. The advantage of the  $V/I$  method is that the voltage applied to the electrodes is adjustable. This expands the resistance range of the instrument, making it particularly suitable for measurements on insulating materials. Using the internal voltage source also optimizes the circuitry for reliability. The electrometer and a Watlow F4 programmable temperature controller are interfaced to a computer using a LabView program, which controls the two units, records the data, computes the resistivities and saves the results to the hard disk.

The presence of background currents introduces systematic errors and noise when computing the resistance by measuring the current due to an applied voltage. Averaging cannot remove the systematic shift in the observed current. However, the alternating polarity technique for resistance measurements removes the contributions of the background current to second order and provides a convenient method for obtaining reproducible results.<sup>95</sup> This is accomplished by applying essentially a square wave voltage source to the electrodes and measuring the current at the end of four successive half cycles. By an averaging procedure, any uniformly decaying background current can be canceled out to second order. An equivalent circuit for the measurement set up is shown in Fig. 2(a). Assuming that the decay of the background current can be reasonably approximated by an exponential decay, the total current,  $i_T$ , can be written

$$i_T = \frac{V}{R} + \frac{V}{R_C} e^{-t/\tau_C} + i_{b0} e^{-t/\tau_b} \quad (5.2)$$

where  $\tau_C = R_C C$ ,  $i_{b0}$  is the initial background current,  $\tau_b$  is the effective background decay constant and  $t$  is time at the beginning of each half cycle. We first do a Taylor series expansion of the background decay to second order. Then an averaging is done using the end currents at four successive half cycles starting with a positive half-cycle. It is generally found that this should start after the first cycle (assuming the cycling starts positive), because the first cycle is very asymmetrical. A simple averaging process over four successive half cycles will remove the background current contribution to second order as follows:

$$\begin{aligned} I_{14} &= \frac{1}{2} \left\{ \frac{1}{2} \left[ \frac{(I_1 - I_2)}{2} + \frac{(-I_2 + I_3)}{2} \right] + \frac{1}{2} \left[ \frac{(-I_2 + I_3)}{2} + \frac{(I_3 - I_4)}{2} \right] \right\} \\ &= (I_1 - 3I_2 + 3I_3 - I_4)/8 \end{aligned} \quad (5.3)$$

where  $I_1$  and  $I_3$  are the final currents of two consecutive positive half cycles and  $I_2$  and  $I_4$  are the final currents of two consecutive negative half cycles as illustrated in Fig. 5.17(b). This calculation can be done for any four consecutive half-cycles that start with a positive half-cycle; however, for the cancellation to be complete, the time durations of the half-cycles must be equal to within 0.1%.<sup>95</sup> For example, from Fig. 2(b), which does not show the first cycle, three values of resistivity are obtained, namely  $2.64 \times 10^9 \Omega \cdot \text{cm}$ ,  $2.80 \times 10^9 \Omega \cdot \text{cm}$  and  $2.89 \times 10^9 \Omega \cdot \text{cm}$  starting with the first positive value for  $I_1 = 5.947 \times 10^{-6}$  A in Fig. 5.17(b). These data illustrate typical convergence of the resistivity as later cycles are analyzed. The degree of convergence is determined by the choice of half-cycle duration. The 50 sec duration used in Fig. 15.17(b) usually gives better than 5% convergence after five full cycles. The important issue regarding the cycle time is that by keeping it constant from run to run and specimen to specimen, the results will be reasonably self consistent and reproducible.

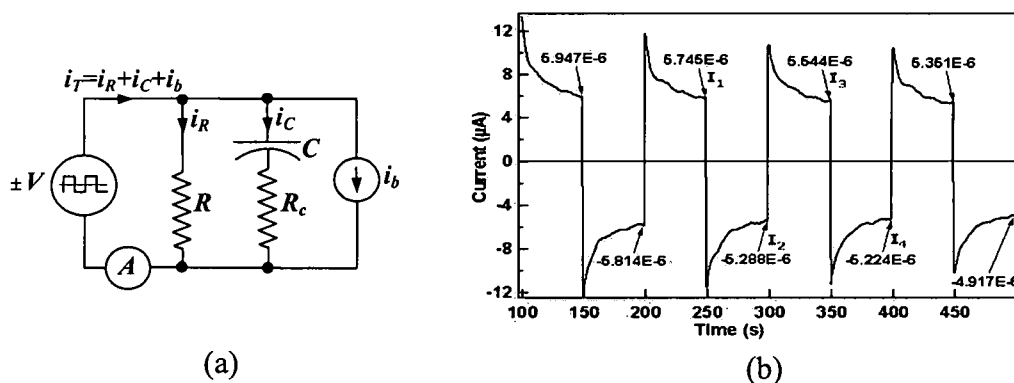


Figure 5.17. (a) Equivalent circuit for resistivity measurement, where  $V$  is the applied alternating potential,  $R$  is the resistance of the polymer specimen,  $C$  and  $R_c$  represent the charging/discharging time constant  $\tau_c = R_c C$  of the electrode-polymer-electrode sandwich and  $i_b$  is the polymer "background" current. (b) Typical alternating polarity ( $\pm 5$  V) data taken on a 3.52 mm-thick, crosslinked, water-insoluble DNA polymer film at  $100^\circ\text{C}$  using the guarded electrode technique. [From Reference No.73]

The complete results of measurements as a function of temperature for a crosslinked 500 kDa DNA-CTMA film with 15 wt% PPIF and for a crosslinked 500 kDa DNA-CTMA film with 20wt% PPIF and 5 wt% DR1 are given in Fig. 5.18. Although these specimens were fabricated and measured at different times, with a chromophore in one, the results show good reproducibility. As would be expected, the small amount of DR1 and the small difference in crosslinker concentration does not influence the resistivity.

As shown in Fig. 5.19, these data were also plotted with a fit to the thermally activated Arrhenius ansatz  $\rho = \rho_0 \exp(E_a / kT)$ , which is usually written in the inverse form as conductivity. The fit to the data reveals a consistent value for the activation energy  $E_a$  of 1.31-1.34 eV, which characterizes the observed five orders of magnitude range of resistivity. This characteristic of these data supports the electron hopping model for the conduction mechanism in DNA in the temperature range of the measurements.<sup>96,97</sup> Measurements on dried sheets of oriented Li-DNA from calf thymus were reported to have an activation energy of  $\sim 0.8$  eV.<sup>88</sup> The slightly higher value obtained here is most likely due to the presence of the PPIF crosslinker. At the last point of 125 °C with the DR1 data, the electrode began to bubble, which we frequently observe at high temperatures when there is an applied voltage (Sec. 6.1).

As can be seen from Fig. 5.18, the resistivities of the materials are essentially equal, despite differences in crosslinker and chromophore concentration. Although these equal resistivities will not optimize the poling process, they will not hinder it either. The important issue is to make sure that, at least, the cladding material is not *more* conductive than the core, which it is not.

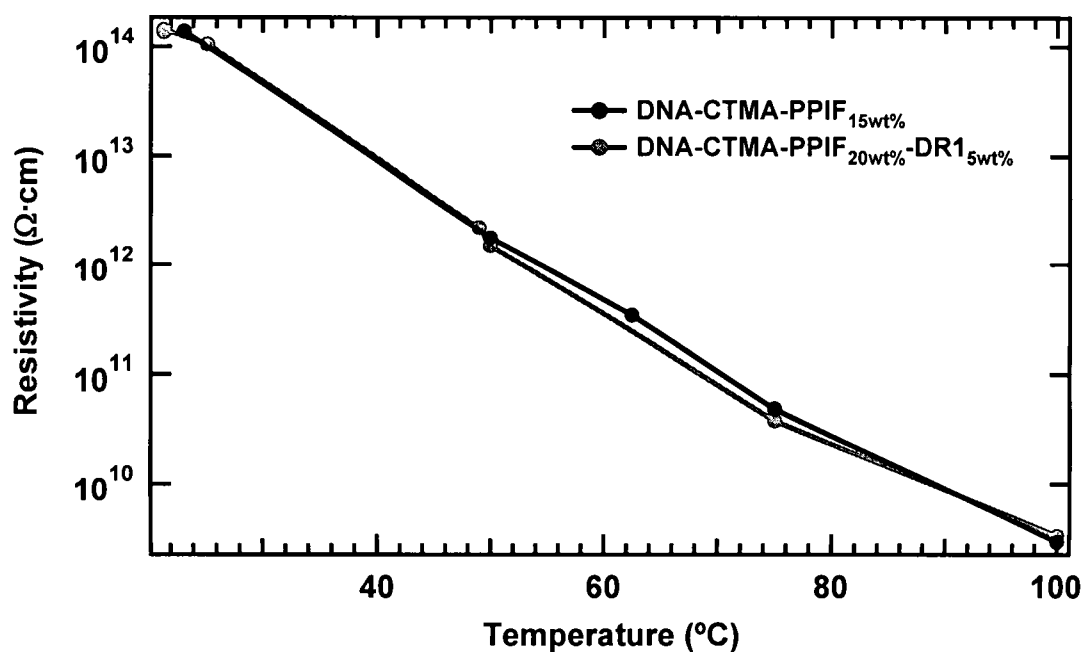


Fig. 5.18. Resistivity as a function of temperature of crosslinked DNA-CTMA films with and without DR1 chromophore.  
[From Reference No. 73]

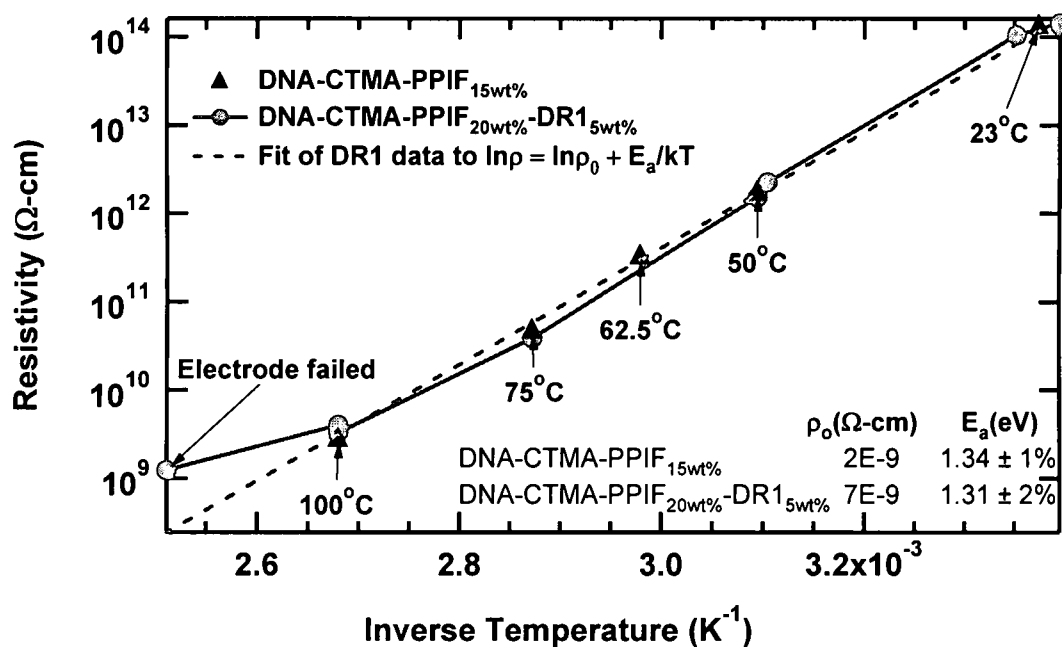


Fig. 5.19. Resistivity as a function of inverse temperature of crosslinked DNA-CTMA films with and without DR1. An activation energy of 1.31-1.34 was found over the temperature range. [From Reference No. 73]

### 5.7 Dielectric Constant

The dielectric constant was calculated for noncrosslinked DNA-CTMA films at microwave frequencies.<sup>32,98</sup> This was done at room temperature with a co-planar waveguide (CPW) test structure. The DNA had a molecular weight of ~6500 kDa. The DNA-CTMA was spin-coated onto a degreased MgO substrate. The dielectric properties of the film were extracted by comparing the propagation constants of the CPW lines of the bare MgO substrate to the DNA-CTMA-coated MgO substrate. An average dielectric constant of  $\epsilon = 4$  was calculated for the DNA-CTMA film at microwave frequencies. This is comparable to that of typical polymers.<sup>2</sup>



## CHAPTER 6

### ELECTRO-OPTIC COEFFICIENT MEASUREMENTS

The electro-optic (EO) coefficient is a measure of the optical degree of nonlinearity in a material, such as a poled polymer film. It is inversely proportional to the half-wave voltage  $V_{\pi}$  of an EO modulator. It is desirable, therefore, to maximize the EO coefficient in order to minimize  $V_{\pi}$ . For a polymer-chromophore film, the EO coefficient is induced through electric field poling, where the force of the field produces a torque on the chromophores and preferentially aligns them along the direction of the field. Inorganic crystals (such as lithium niobate) currently used in EO modulating devices have EO coefficients of  $\sim 30$  pm/V. To offer a viable alternative to inorganic crystals, a poled polymer film must, therefore, have an EO coefficient of at least 30 pm/V.

EO coefficients as high as 100 pm/V have already been achieved for poled polymer films and results  $>300$  pm/V have been predicted theoretically.<sup>2-6</sup> These EO coefficients are the result of high-quality chromophores specifically chemically engineered for application in poled polymer films. Such chromophores, for example the CLD series developed by Dalton *et al.*, achieve these high degrees of nonlinearity with

high molecular hyperpolarizabilities.<sup>99</sup> Additionally, the chromophores are designed to reduce inter-molecular reactions, allowing for a higher chromophore loading concentration.<sup>2-6</sup> The fabrication of these chromophores, however, is time-intensive and difficult. Demand for them has not yet increased enough to warrant mass production, and as a result they are expensive (~\$10,000 per gram) and difficult to obtain.<sup>100</sup>

Because of the difficulty in acquiring high-quality chromophores, the chromophore dye, Disperse Red 1 (DR1), which can be purchased commercially from Sigma-Aldrich, was used.<sup>26</sup> At its maximum loading capacity (30 wt%), DR1 typically only produces results of ~13 pm/V at 633 nm in common polymers such as PMMA.<sup>25,101</sup> Clearly this number is not competitive with inorganic crystal devices.<sup>2</sup> However, if an EO coefficient can be demonstrated and optimized in DNA-CTMA with the DR1 chromophore, then a higher quality chromophore can later be obtained and used to make a device with an EO coefficient competitive with those in current EO modulators.

## **6.1 Contact Poling**

### **6.1.1 Technique**

As previously discussed in Sec. 2.1.1, the poling process is conceptually straightforward. A chromophore-doped polymer film is heated to its glass transition temperature  $T_g$ , and an electric field is applied to enhance the statistical alignment of the dipoles in the direction of the field. The film is then cooled down with the field still applied to maintain this enhanced dipole alignment. The result is a poled polymer film.

In practice, however, poling is quite complex. One common problem often encountered in electrode poling is the problem of electrical shorts before, during and sometimes even after the poling process. Often, this occurs because of contaminants

during the fabrication process – a piece of dust that becomes lodged in a film can cause shorts during poling. It can also occur due to dielectric breakdown of the polymer itself. Additionally, shorts can occur due to non-uniformity of the films. Films are typically only 2 – 4  $\mu\text{m}$  thick, and a small pinhole can short the entire film. To combat the occurrence of shorts, the DNA solutions were filtered through a 0.2  $\mu\text{m}$  syringe filter to remove impurities as discussed in Sec. 4.4. Spin-coating and curing of the films were done in a clean-room ( $\sim$  Class 1000) to prevent contamination from environmental particulates. Special care was taken to sputter the top electrodes as quickly as possible after the films had cured, and to store the films in a dry environment (i.e., a vacuum oven maintained at room temperature with Drierite to absorb moisture). These measures reduced, although not completely eliminated, contamination of the films and consequently the occurrences of shorts during the poling process.

Poling was done in a nitrogen atmosphere to reduce harmful interactions from the environment. One reason to pole in such an atmosphere is to eliminate the effects of humidity, which can cause shorting if the film is susceptible to water adsorption, as are DNA-based films. Another reason is to prevent bleaching of the chromophores by free oxygen in the polymer.<sup>21</sup>

The poling system used is shown schematically in Fig. 6.1 and as an image in Fig. 6.2. The temperature was applied using a hotplate controlled by a Watlow F4 programmable temperature controller. The voltage was generated by a Bertan Series 225 high power voltage supply, and the current was monitored with a Keithley 617 programmable electrometer. All equipment was computer interfaced and controlled with a LabView program. The hotplate was contained within a copper-mesh coated Plexiglas

box to provide electrical shielding. This box was purged with nitrogen gas continuously during the poling process.

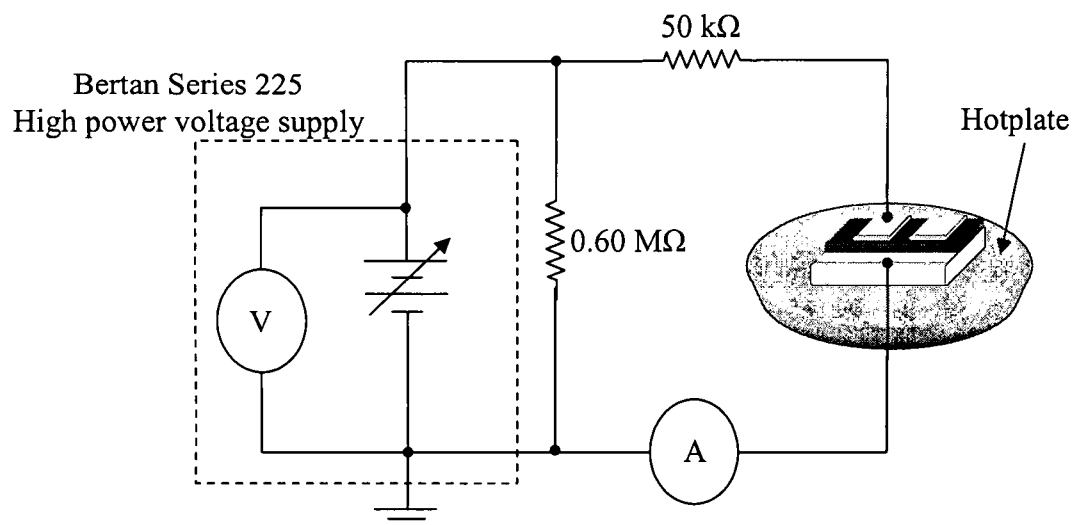


Fig. 6.1. Schematic of the poling system. The ammeter is a Keithley 617 programmable electrometer and the hotplate is controlled by a Watlow F4 programmable temperature controller. The Keithley, Watlow, and Bertan are interfaced to a computer using a LabView program, which controls the units, records the data, and saves the results to the hard disk.

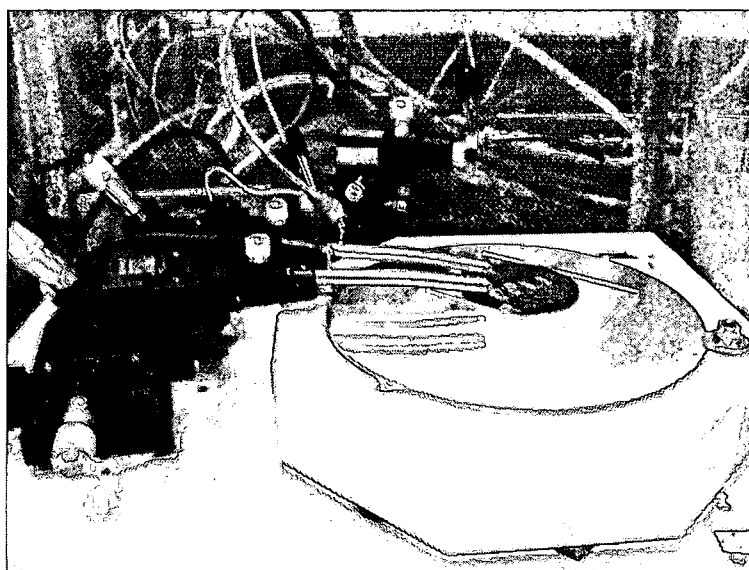


Fig. 6.2. Image of the poling system.

The typical sample configuration is shown in Fig. 6.3. The sample was placed on the hotplate and small gold-coated semicircle pads were placed on top of the gold and indium tin oxide (ITO) electrodes. These gold pads were made by gold-plating holes punched from a thin copper sheet. The electrical leads were attached to probes that made contact with the gold pads; this eliminated the possibility of any sharp edges coming into contact with the film. Electrical contact was made with the gold on the very edge of the sample where there was no ITO. This reduced the risk of punching through the electrode and shorting the film.

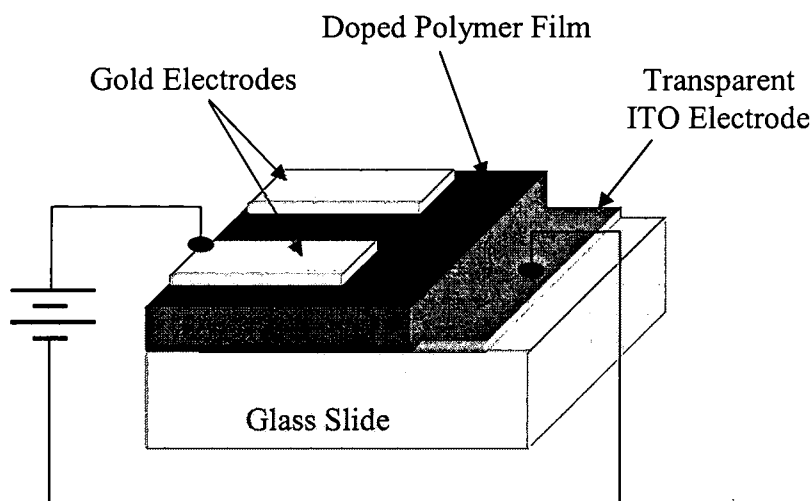


Fig. 6.3. Sample Configuration for Poling. Cut-away view in perspective.

As discussed in Sec. 2.1.1, poling is an extensively researched process and many references on poling techniques are available.<sup>48-57</sup> When electrode poling was first introduced, the common technique was to first heat the sample to its  $T_g$ , and then apply the required voltage to the sample.<sup>44</sup> Recently, however, there have been results

suggesting that a higher degree of alignment is achieved if the voltage is applied first, and then the sample is heated to its  $T_g$ .<sup>24,47</sup> There is no conclusive evidence to support one of these methods over the other; however, Watson *et al.* have done a thorough modeling of the poling process and suggest heating the sample to the poling temperature before applying any voltage to remove trapped oxygen in the sample.<sup>58</sup> Both methods, temperature-first, voltage-second (*T then V*), and voltage-first, temperature-second (*V then T*), have been employed in this research. The majority of the poling data acquired here was done with the *V then T* technique, which our group had previously shown to be more effective with APC and PMMA.<sup>47</sup> However, toward the end of our studies, we found that allowing the DNA-based films to soak at the poling temperature for 30 minutes prior to applying the poling voltage gave a higher EO coefficient with less chance of shorting.

For the *V then T* technique, the voltage was applied to the film at room temperature at a rate of 5 – 10 V/min. The rate was determined in part by the thickness of the film. Thicker films can withstand larger increases in voltage, and larger voltage steps reduce the time of the poling process. The voltage rate was also determined by monitoring the current. If the current through the film seemed to be high compared to past films, the voltage step size was reduced. Occasionally, current spikes due to irregularities in the film forced a longer wait time before the next voltage step. Once the required voltage was applied to the film (50 – 100 V/ $\mu\text{m}$ ), the temperature was increased at a rate of 10-20  $^{\circ}\text{C}/\text{min}$ . As the temperature increased, the current increased dramatically, typically from a few hundred nA to several  $\mu\text{A}$ . Once the desired poling temperature was reached, the current typically began to decay. Watson *et al.* have

modeled that dwelling at the poling temperature for longer periods yields much higher poling efficiencies.<sup>58</sup> Anecdotally, we observed that a longer dwelling time was required (10 – 40 min). The dwelling time was typically based on the current decay. Once the current had decayed to 60-70% of its peak value, the sample was cooled. Copper tubing was used to run chilled water under the hotplate to increase the rate of cooling. Once the film had cooled to room temperature, the field was stepped down and the poling process was complete.

For the *T then V* technique, the sample was heated to the poling temperature at a rate of 10-20 °C/min and allowed to soak for at least 30 min. The voltage was then applied to the film at a rate of 5-10 V/min. Once the desired poling voltage was reached, the technique was identical to the *V then T* technique.

Poling is still very much more of an art than a science. It is impossible to give a step by step, detailed recipe, because the poling process is often very different for different films. Even among the same species of film, the poling characteristics can vary significantly. This has been especially true for DNA-based films. One must gain a “feel” for the poling process and use one’s judgment on matters of voltage and temperature rates based on experience. It is best to remain flexible in the poling regime. For example, a current spike may delay a planned voltage increase of 10 V/min. If the current spikes, we have found that waiting for it to return to normal levels reduces the risk of shorting the sample.

### **6.1.2 DNA-Specific Poling Challenges**

Because DNA is unique among polymer materials, it presents poling challenges not seen with other polymers. As discussed in Sec. 5.5, a clear  $T_g$  could not be measured

for either crosslinked or noncrosslinked DNA-CTMA films using DSC, although a  $T_g$  of 148 °C was measured for the DNA-CTMA powder. The temperatures used for poling the DNA-based films were determined through systematic study. The molecular weight (MW) of the starting DNA plays a significant role in the poling efficiency for both crosslinked and noncrosslinked DNA-CTMA films.

Problems occurred occasionally with bleaching of the chromophore during poling. The film does not short, but after poling it has lost much of its color and there is no measurable EO activity. This has been observed with other polymers and is believed to be due to free oxygen in the polymer.<sup>58</sup> We have noticed that the bleaching requires the presence of both high temperature and high field and have found that a field  $\leq 75$  V/ $\mu$ m and a temperature  $< 80$  °C greatly reduces the occurrence of bleaching.

Electrode bubbling and film damage are also problems we have experienced with DNA-based films more so than with other polymers. Although we have occasionally seen this problem with APC and PMMA films, it is not common, and typically a thin layer (100 Å) of chromium applied before the gold electrode to promote adhesion of the gold to the film prevents bubbling with these polymers. The use of a chromium layer did not, however, make a difference in electrode bubbling with DNA-based films. Similar to the bleaching effect, we have observed that electrode bubbling and film damage most often occur in the presence of both high temperature and high field. Limiting the field to  $\leq 75$  V/ $\mu$ m and a temperature  $< 80$  °C greatly reduces the occurrence of electrode bubbling. Additionally, sealing the electrode edges with a thin layer of epoxy has also greatly reduced the occurrence of electrode damage.



## 6.2 Measuring the Electro-Optic Coefficient

The EO coefficient of the film was measured using the Teng and Man ellipsometric technique outlined in Sec. 3.3. A schematic of the experimental setup is shown in Fig. 6.4. A 690 nm diode laser was used for the majority of the measurements, although occasionally a 1310 nm diode laser was also used. The modified expression for the EO coefficient is given by<sup>102</sup>

$$r_{33} = \frac{3\lambda}{4\pi n^2} \frac{\sqrt{n^2 - \sin^2 \theta}}{\sin^2 \theta} \frac{(V_{\pi/2} - V_{3\pi/2})/2}{V_m V_{dc}} \quad (6.1)$$

One detail that must be noted is that the accuracy of the EO measurements can be greatly reduced due to interference from the reflection of incident light from the air-substrate and substrate-polymer interfaces. These reflections are polarized perpendicular to the plane of incidence; the parallel component is negligible because the angle is very close to Brewster's angle. This reflected light interferes with the light passed through the polymer film and superimposes a strong signal on top of the  $r_{33}$  signal. For a microscope glass-slide substrate ~3 mm thick, these reflections can be blocked with a well-positioned pinhole between the specimen and the compensator (Fig. 6.4). Ideally, an even thicker substrate is desirable to increase the separation of the reflection and the signal, making it easier to block. This pinhole was essential to ensure accurate measurements.<sup>73</sup>

Another detail which must be considered is the size of the active area of the detector. If the area is small, it is likely that not all of the beam will fall on the active area. Because laser waveforms can fluctuate with time, small fluctuations in the beam can introduce small fluctuations on the detected signal if the beam is not fully contained

on the detector area. This can be remedied by using a lens to focus the beam size so that it completely falls on the detector. The lens  $L_1$  in Fig. 6.4 was used for this purpose.

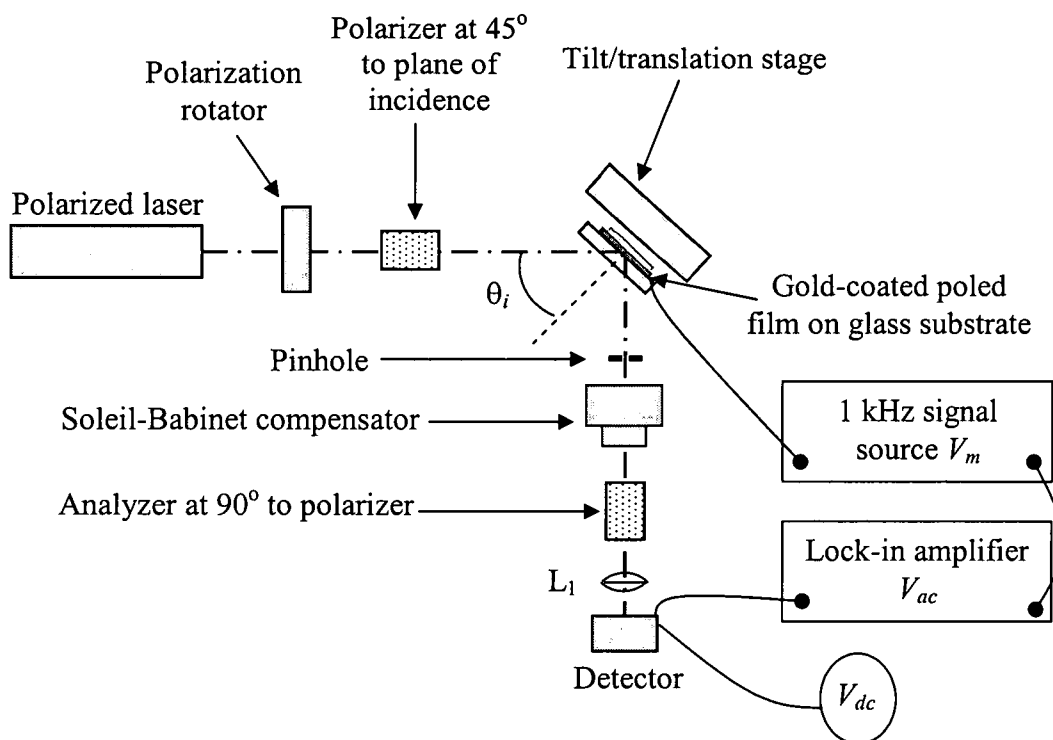


Figure 6.4. The Teng and Man ellipsometric technique for measuring the EO coefficient  $r_{33}$ . The pinhole is adjusted to collect the light that is reflected from the reflecting gold layer on the film and to block, to the extent possible, the light from the other surfaces. Lens  $L_1$  focuses the light on the detector.

Finally, it should be stressed that the correction for  $r_{33}$  due to the electro-absorption effect given in Eq. (3.21) is only valid when the EO effect is dominant. In cases where the electro-absorption effect is dominant, this approximation is no longer accurate. The importance of this fact was emphasized when trying to use the chromophore dye Disperse Red 13 (DR13) in place of DR1. The DR13 absorption is much stronger at 690 nm than that of DR1 and causes the electro-absorption effect to

dominate for small EO signals. An EO coefficient nearly two times greater was measured for DR13 than for DR1 at 690 nm for similar loading by wt%. It seemed, therefore, that DR13 was a better chromophore choice for DNA-based films because it gave higher EO results than DR1. It was not until measurements were made at 1310 nm, far from the absorption band, that we realized the EO measurements at 690 nm were inflated for the DR13 films due to electro-absorption. Using Eq. (3.21), an EO coefficient of 1.5 pm/V was calculated for a DNA-CTMA-DR13 sample at 690 nm; however, at 1310 nm, an EO coefficient of only 0.05 pm/V was calculated for the same spot. The EO coefficient should decrease with increasing wavelength according to a two-level model.<sup>103</sup> Compared to the dispersion of the EO coefficient in other polymers,<sup>103</sup> a reasonable expectation would be that the EO coefficient in DNA-CTMA be roughly half of its value at 1300 nm with respect to its value at 690nm. Clearly, the EO measurements for the DR13 film at 690 nm and 1300 nm do not exhibit this type of relationship. This indicates that the electro-absorption effect is dominant for the DR13 films at 690 nm and the approximation in Eq.(3.21) cannot be made. On the other hand, measurements for DR1 films at 690 nm and 1310 nm confirmed that the EO effect is dominant at 690 nm, and the approximation can be used. A DNA-CTMA-DR1 film was measured to have an EO coefficient of 0.72 pm/V at 690 nm and at the same spot had a value of 0.41 pm/V at 1310 nm, which is consistent with expectations.

### 6.3 Results

There are many variables to consider when optimizing the poling process for any polymer material; these are primarily the dependence of the EO coefficient on the poling field, poling temperature and poling time. The DNA-based materials have the additional

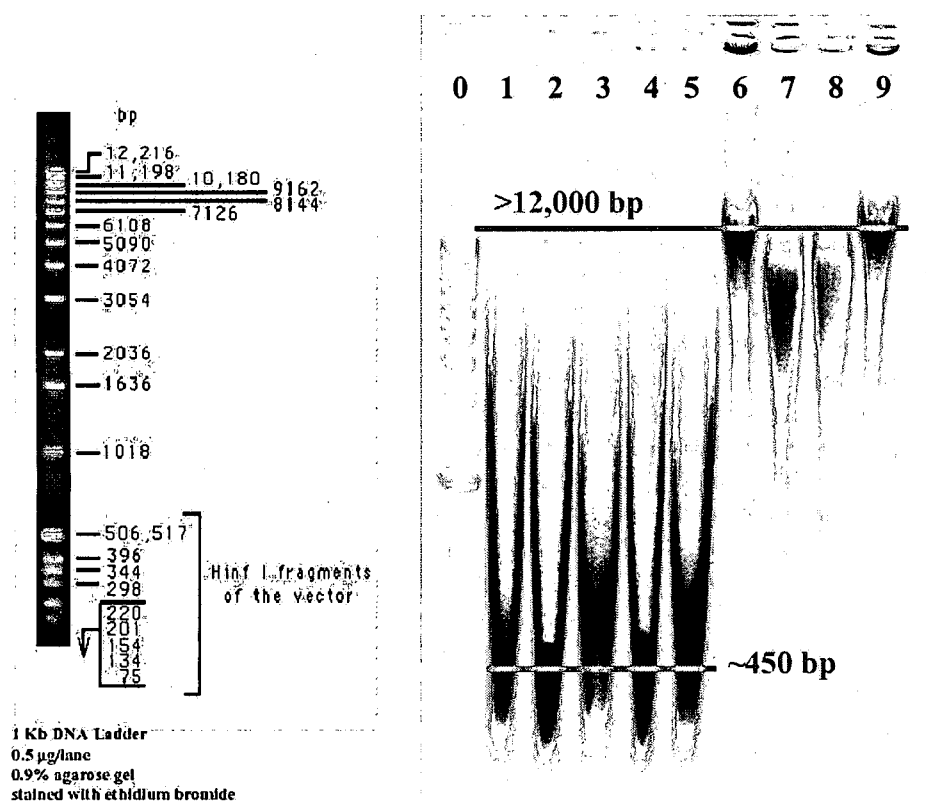
parameters of the percentage of crosslinker, the DNA molecular weight, the distribution of molecular weights and a not well-defined glass transition temperature. These are not issues with common polymer materials such as APC and PMMA, which have fixed molecular weights and clearly defined glass transition temperatures.

With at least four new parameters to consider in addition to the poling process, optimizing the EO coefficient through poling of the DNA-CTMA films was a daunting task. As such, not all of these parameters were fully separated from one another to the extent that a definitive conclusion about their effect on the poling process was drawn. Nonetheless, general trends were evident. The focus of this study was to find a poling process that worked consistently, that achieved the highest possible EO coefficient, and that left the film and electrode without damage. While every attempt was made to distinguish the effect of as many of parameters on poling as possible, limited time and resources restricted the extent to which this was possible.

#### ***6.3.1 Effect of Molecular Weight***

Early batches of DNA received from CIST were small-scale, laboratory-produced quantities and not the large-scale, mass-produced quantities received later. Poling was first accomplished with these early batches of DNA. EO coefficients of 3 pm/V were achieved with noncrosslinked DNA-CTMA films for an 8 wt% DR1 loading. When our laboratory-processed DNA supply was exhausted, the new batches of DNA received from CIST were mass-produced, as their DNA processing operations had been transitioned to industry. We were unable to achieve an EO coefficient of any kind with this mass-produced DNA, despite repeated efforts and many variations on the poling process (poling field, temperature, and technique).

Although the mass-produced DNA was supposed to be identical to the laboratory-produced DNA, we discovered that with regard to molecular weight (MW), there was a marked difference between the materials produced by these two processes. Using a 0.8% agarose gel, the laboratory-produced DNA was measured to have a MW of ~300 kDa, while the mass-produced DNA had a MW >8000 kDa. Figure 6.5 shows the negative image of the results of this agarose gel for the laboratory-produced and mass-produced DNA materials.



6.5 Agarose gel result for laboratory-produced and mass-produced DNA material from CIST. The negative of the image is shown here. A 0.8% gel was used. Well "0" is the 1 Kb DNA Ladder standard. [From Reference No. 81] Wells "1-5" are the laboratory-produced DNA, it has an average base pair length of ~450 bp, which corresponds to a MW of ~300 kDa. Wells "6-9" are the mass-produced DNA, it has an average base pair length of >12,000 bp, which corresponds to a MW > 8000 kDa.

We hypothesized that this difference in MW accounted for our inability to pole the mass-produced material, and developed a technique using an ultrasonic horn to lower the MW from >8000 kDa to between 200-500 kDa (Sec. 4.2.1). Using this lower MW DNA, we were able to achieve the degree of poling reported in the following sections. We believe that when MW is high (>1000 kDa), the long strands become entangled, preventing chromophore alignment during the poling process. It is well-known that short DNA molecules up to chain lengths of ~100 base pairs behave as rigid rods.<sup>83,104</sup> Although the low MW chain lengths being used are slightly longer than this (200 kDa  $\approx$  300 base pairs), it is likely that they exhibit rigid rod-type behavior. This behavior would conceivably allow the chromophores to be more easily oriented in the presence of an electric field because they would not become entangled in long, intertwining strands.

We were unable to achieve any EO activity using the high molecular weight, mass-produced DNA received from CIST (>8000 kDa). It was found that a MW of between 200 – 500 kDa realized the highest EO coefficient. Molecular weights <200 kDa may increase the EO coefficient further; however, sonication could not reduce the MW <200 kDa. Thus, the poling efficiency for DNA with a MW in this range could not be tested. A more thorough study of the relationship between MW and poling efficiency is needed before a definitive relationship between poling efficiency and MW can be drawn.

The only authoritative conclusion drawn with respect to the effect of MW on DNA is that a MW >8000 kDa cannot be poled, while poling can consistently be achieved with a MW between 200-500 kDa. We attempted to compare the EO coefficients between DNA of 200 kDa and 500 kDa; however, our results were

ambiguous and inconclusive (Table 6.1). This is most likely due to the fact that the MW of the DNA reported is not strictly 200 kDa and 500 kDa, but rather, as discussed in Sec. 4.2.1, is a broad range of molecular weights with a distribution of  $\pm 50\%$ . To truly isolate the effect of MW on the poling process, a more effective method than sonication must be employed to reduce the MW of the DNA with narrower distributions. These types of techniques are common among biologists, who, through enzymatic treatments, can routinely produce DNA strands of equal lengths.<sup>83</sup> However, these processes are tailored for DNA quantities of micrograms while several grams of material are required to produce bulk DNA-based film specimens for poling. These techniques for microscopic DNA materials could not be easily adapted for our macroscopic materials needs, due to price and amount of human effort.

Table 6.1. Summary of poling results for DNA-based films. Under Sample ID, "Lab" designates laboratory-produced noncrosslinked DNA-CTMA films, "MP" designates mass-produced noncrosslinked DNA-CTMA films and "XL" designates crosslinked DNA-CTMA films. All  $r_{33}$  results were measured at 690 nm except for the "Lab" samples, which were measured at 633 nm.

Sample ID	MW (kDa)	Crosslinker (wt%)	DR1 (wt%)	Field (V/ $\mu$ m)	Temperature ( $^{\circ}$ C)	$r_{33}$ (pm/V)	Technique
Lab1	300	0	8	60	60	$1.91 \pm 0.09$	<i>V then T</i>
Lab2	300	0	8	80	60	$3.04 \pm 0.02$	<i>epoxy V then T</i>
Lab3	300	0	10	54	50	$1.93 \pm 0.27$	<i>epoxy V then T</i>
MP1	200	0	5	56	65	$0.72 \pm 0.10$	<i>T then V</i>
MP2	200	0	5	56	65	$0.70 \pm 0.01$	<i>T then V</i>
MP3	200	0	5	64	65	$0.48 \pm 0.02$	<i>epoxy T then V</i>
MP4	500	0	5	41	65	$0.65 \pm 0.01$	<i>T then V</i>
							<i>epoxy</i>
XL1	200	10	5	70	65	$2.02 \pm 0.03$	<i>T then V</i>
XL2	200	10	5	64	65	$1.51 \pm 0.02$	<i>T then V</i>
XL3	200	20	5	91	65	$1.04 \pm 0.07$	<i>T then V</i>
XL4	200	10	5	75	65	$0.83 \pm 0.03$	<i>V then T</i>
XL5	200	10	5	50	65	$0.60 \pm 0.02$	<i>V then T</i>
XL6	200	10	5	50	100	$0.71 \pm 0.01$	<i>V then T</i>
XL7	200	20	5	75	65	$0.74 \pm 0.02$	<i>V then T</i>
XL8	500	20	5	75	65	$1.00 \pm 0.04$	<i>V then T</i>
XL9	500	20	5	100	80	$1.33 \pm 0.03$	<i>V then T</i>
XL10	500	20	5	100	90	$1.12 \pm 0.01$	<i>V then T</i>

### 6.3.2 Noncrosslinked DNA-CTMA films

Table 6.1 shows the poling results of both noncrosslinked and crosslinked DNA-CTMA-DR1 films. The poling profile data for selected samples is shown in Fig. 6.5. The noncrosslinked films are designated by the prefix "Lab" for films fabricated from the laboratory-produced DNA, and "MP" for those fabricated from the mass-produced DNA. The prefix "XL" is used to designate the crosslinked DNA films that are discussed in the



following section. The first examples of poled DNA-CTMA films were achieved with the laboratory-produced DNA. An EO coefficient of  $r_{33} = 3.04 \pm 0.02$  pm/V was demonstrated for a film with 8 wt% DR1 for poling conditions of 80 V/ $\mu$ m at 60 °C. The results for the mass-produced noncrosslinked DNA-CTMA films are significantly lower; however, these have only 5 wt% DR1, which accounts for the difference. Because it was determined that a crosslinked DNA-based film was ultimately necessary for the EO waveguide device, very little effort was focused on optimizing the EO coefficient for these noncrosslinked films. Rather, once an EO coefficient was consistently demonstrated in the noncrosslinked films, the focus was shifted toward optimizing the poling conditions for the crosslinked films.

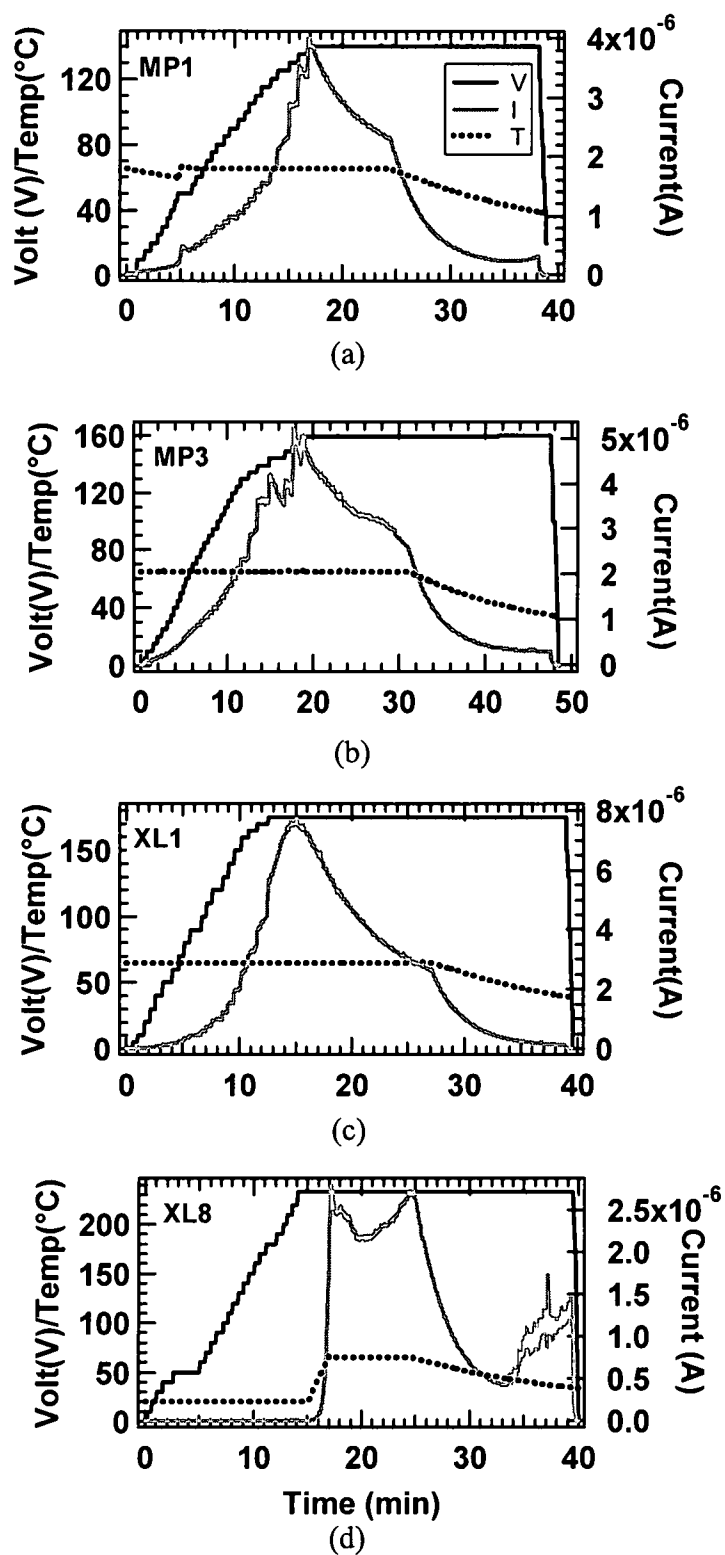


Fig. 6.5. Poling data profiles for selected samples.  
(a) MP1, (b) MP3, (c) XL1, (d) XL8

### 6.3.3. *Crosslinked DNA-CTMA films*

Crosslinking the core DNA-CTMA film is necessary to make it resistant to the solvent of the top cladding layer, enabling spin-coating of the top cladding layer on top of the core. Two different concentrations of crosslinker were explored for the core material. Films with 10 wt% (36.1 mol%) poly(phenyl isocyanate)-co-formaldehyde (PPIF) and films with 20 wt% (81.2 mol%) PPIF, with respect to DNA-CTMA, were fabricated (Sec. 4.4.3). Although 10 wt% PPIF was sufficient to give solvent-resistant films, the higher concentration of 20 wt% PPIF was also explored for use as a core material due its slightly higher index of refraction. These 20 wt% PPIF films were characterized to provide the option of a greater index difference between the core and cladding layers than that provided by the chromophore dye alone. Increasing the amount of crosslinker from 10 wt% to 20 wt% increases the refractive index by an additional 0.0161 at both  $\lambda=690$  nm and  $\lambda=1310$  nm (Table 5.1). This index difference can provide better optical confinement of the propagating wave.

The amount of DR1 used in these studies was typically 5 wt% (21.8 mol%) with respect to DNA-CTMA. This was not the maximum loading capacity; however, many of the waveguide characterization measurements were done at  $\lambda = 690$  nm (where DR1 and DNA-CTMA are slightly absorbing), and allowed visible confirmation of a propagating mode. Five wt% was found to be the maximum loading of DR1 that would still allow a visible streak to propagate the length of a two-inch waveguide without significant attenuation. EO coefficients significantly lower than published results for DR1 are, therefore, to be expected, since the maximum attainable EO coefficient is proportional to the amount of chromophore dye and the typical DR1 loading is 30 wt%.<sup>101</sup> A summary

of the poling results for crosslinked DNA-CTMA films with 5 wt% DR1 is shown in Table 6.1. The EO coefficient reported is an average of three separate measurements taken for each film at three different spots spanning the length of the film. This is to average out any variations due to film thickness or the poling process, and to gain a measure of the poling uniformity. The standard deviation for these measurements was typically  $\leq 3\%$ , demonstrating high poling uniformity.

The addition of the crosslinker improves poling efficiency compared to noncrosslinked films for films poled with the *T then V* technique. This is surprising, because one would expect that the increased mechanical stability provided by crosslinking would hinder chromophore alignment. Referring to Table 6.2, sample XL2 had an EO coefficient of  $1.51 \pm 0.02$  pm/V, while for identical poling conditions, sample MP3 had an EO coefficient of only  $0.48 \pm 0.02$  pm/V. However, compared to crosslinked samples that were poled with the *V then T* technique, the results were the opposite. The noncrosslinked sample MP1 had an EO coefficient of  $0.72 \pm 0.10$  pm/V, while for the same poling conditions but opposite technique (*T then V*) the crosslinked sample had a lower EO coefficient of  $0.60 \pm 0.02$  pm/V. The conclusion that can be drawn from this is not that crosslinking necessarily improves poling efficiency, but that the optimum poling techniques are different for noncrosslinked versus crosslinked films. A more thorough study is needed to confirm this.

Table 6.2. Comparison of poling results between noncrosslinked and crosslinked DNA-based films. The technique that give optimum results for each film are different. Higher EO coefficients were achieved with *T then V* for crosslinked films, while noncrosslinked films had higher EO coefficients for the *V then T* technique.

Sample ID	MW (kDa)	Crosslinker (wt%)	DR1 (wt%)	Field (V/ $\mu$ m)	Temperature ( $^{\circ}$ C)	$r_{33}$ ( $\lambda=690$ ) (pm/V)	Technique
XL2	200	10	5	64	65	$1.51 \pm 0.02$	<i>T then V</i>
MP3	200	0	5	64	65	$0.48 \pm 0.02$	<i>T then V</i>
MP1	200	0	5	56	65	$0.72 \pm 0.10$	<i>T then V</i>
XL5	200	10	5	50	65	$0.60 \pm 0.02$	<i>V then T</i>

The dependence of the EO coefficient on the poling field can be seen from Table 6.3. Samples XL1 and XL2 were poled using the same poling technique (*T then V*), at the same temperature of 65  $^{\circ}$ C, and had a mean MW of 200 kDa with 10 wt% PPIF crosslinker. Sample XL1 was poled with a higher field (70 V/ $\mu$ m) compared to XL2 (64 V/ $\mu$ m), and XL1 had an EO coefficient of  $2.02 \pm 0.03$  pm/V while XL2 had a lower EO coefficient of  $1.51 \pm 0.02$  pm/V. Samples XL4 and XL5 were also poled using the same poling technique with respect to each other (*V then T*), at the same temperature of 65  $^{\circ}$ C and had a mean MW of 200 kDa with 10 wt% PPIF crosslinker. Sample XL4 was poled with a higher field (75 V/ $\mu$ m) compared to XL5 (50 V/ $\mu$ m), and XL4 had an EO coefficient of  $0.83 \pm 0.03$  pm/V while XL5 had a lower EO coefficient of  $0.60 \pm 0.02$  pm/V. These results are consistent with Watson *et al.* who have reported that the level of poling achieved is directly proportional to the magnitude of the poling field.<sup>58</sup> We have found a threshold limit of 75 V/ $\mu$ m for the poling field, above which there is significant electrode bubbling and film damage.

Table 6.3. EO coefficient for crosslinked films as a function of poling field. Higher fields yield higher EO coefficients.

Sample ID	MW (kDa)	Crosslinker (wt%)	DR1 (wt%)	Field (V/ $\mu$ m)	Temperature ( $^{\circ}$ C)	r33 ( $\lambda=690$ ) (pm/V)	Technique
XL1	200	10	5	70	65	$2.02 \pm 0.03$	<i>T then V</i>
XL2	200	10	5	64	65	$1.51 \pm 0.02$	<i>T then V</i>
XL4	200	10	5	75	65	$0.83 \pm 0.03$	<i>V then T</i>
XL5	200	10	5	50	65	$0.60 \pm 0.02$	<i>V then T</i>

The relationship between poling technique and the EO coefficient can be seen from Table 6.4. For similar poling voltages and temperatures, the *T then V* technique gave consistently higher EO coefficients than the *V then T* technique for crosslinked DNA-based films. This contradicts a study reported previously by our group for the polymers PMMA and APC.<sup>47</sup>

Table 6.5 illustrates the relationship between the amount of crosslinker and the EO coefficient. The samples with smaller concentrations of crosslinker (10 wt%) had EO coefficients significantly higher than the samples with higher concentrations of crosslinker (20 wt%). Samples XL4 and XL7 were poled under similar conditions, but XL4 had 10 wt% crosslinker while XL7 had 20 wt% crosslinker. Sample XL4 showed an EO coefficient increase of 12% over that of XL7. The increase was more dramatic in samples XL1, XL2 and XL3, which were poled with the *T then V* technique. Both XL1 and XL2 had a concentration of 10 wt% crosslinker while XL3 had a concentration of 20 wt%. The EO coefficient for XL2 showed an increase of 45% over that of XL3, and the EO coefficient for XL1 showed an increase of 94% compared to XL3. Although the

poling field was not the same for these samples, XL3 was poled with a higher field than XL1 and XL2. This higher field should have increased its EO coefficient. It can be concluded, therefore, that the lower EO coefficient exhibited by XL3 with respect to XL1 and XL2 is due to the increased concentration of crosslinker.

Table 6.4. EO coefficient as a function of poling technique. The T than V technique yields higher EO coefficients. All films have the same MW, same concentration of XL, and are poled at the same temperature. Higher EO results were measured for XL1 and XL2 despite being poled with a lower field.

Sample ID	MW (kDa)	Crosslinker (wt%)	DR1 (wt%)	Field (V/ $\mu$ m)	Temperature ( $^{\circ}$ C)	r33 ( $\lambda=690$ ) (pm/V)	Technique
XL1	200	10	5	70	65	$2.02 \pm 0.03$	<i>T then V</i>
XL2	200	10	5	64	65	$1.51 \pm 0.02$	<i>T then V</i>
XL4	200	10	5	75	65	$0.83 \pm 0.03$	<i>V then T</i>
XL5	200	10	5	50	65	$0.60 \pm 0.02$	<i>V then T</i>

Table 6.5. EO coefficient as a function of crosslinker concentration. For similar poling conditions, samples with 10 wt% crosslinker have higher EO coefficients than those with 20 wt%

Sample ID	MW (kDa)	Crosslinker (wt%)	DR1 (wt%)	Field (V/ $\mu$ m)	Temperature ( $^{\circ}$ C)	r33 ( $\lambda=690$ ) (pm/V)	Technique
XL1	200	10	5	70	65	$2.02 \pm 0.03$	<i>T then V</i>
XL2	200	10	5	64	65	$1.51 \pm 0.02$	<i>T then V</i>
XL3	200	20	5	91	65	$1.04 \pm 0.07$	<i>T then V</i>
XL4	200	10	5	75	65	$0.83 \pm 0.03$	<i>V then T</i>
XL7	200	20	5	75	65	$0.74 \pm 0.02$	<i>V then T</i>

### 6.3.4 Summary

The optimum poling technique is different for crosslinked and noncrosslinked films. Crosslinked films produced better results with the *T then V* technique, while noncrosslinked films produced better results with the *V then T* technique. For both films, film and electrode damage was lessened by using a thin outline of epoxy around the electrode edges and limiting the poling temperature to  $\leq 80^{\circ}\text{C}$  and the field to  $\leq 75\text{ V}/\mu\text{m}$ .

Among crosslinked DNA-CTMA films, optimum poling conditions were found for films with 10 wt% crosslinker, poled with the *T then V* poling technique with as high of a field as possible. It is necessary, however, to limit the field to  $75\text{ V}/\mu\text{m}$  to prevent electrode and film damage. An EO coefficient of  $2.0\text{ pm}/\text{V}$  was achieved for a crosslinked DNA-CTMA film. A poling temperature of  $65^{\circ}\text{C}$  provided consistent results, with no significant EO coefficient improvement at higher temperatures. Further work must be done to show that this is the ideal poling temperature as the results in Table 6.1 are ambiguous due to variations in the other poling parameters.



## CHAPTER 7

### ALL-DNA-BASED EO WAVEGUIDE MODULATOR

#### 7.1 All DNA-Based Three-Layer Waveguide

Preceding the development of an all-DNA-based three-layer EO waveguide *modulator*, a three-layer DNA-based *waveguide* was demonstrated. This was a planar structure with crosslinked DNA-CTMA as the top and bottom cladding layers and crosslinked DNA-CTMA-DR1 as the core layer. Fabrication techniques for masking part of the core layer from the top cladding layer were developed. This was necessary because the planned measurement techniques involved prism coupling, which cannot be achieved through a top cladding layer of a three-layer waveguide.

##### 7.1.1 Fabrication

A three-layer DNA-based waveguide was successfully fabricated and is shown in Fig. 7.1. The cladding layers were crosslinked 500 kDa DNA-CTMA films with 15 wt% PPIF and the core layer was a crosslinked 500 kDa DNA-CTMA-DR1 film with 20 wt% PPIF and 3 wt% DR1. The core and cladding solutions were prepared as described in Sec. 4.4 with a 93.1 mM DNA-CTMA-butanol solution for the cladding and an 85.0 mM DNA-CTMA-butanol solution for the core. A higher DNA-CTMA concentration was

used for the cladding solution to facilitate thicker films. The bottom cladding layer was spin-coated on an  $\text{SiO}_2$  substrate at 800 rpm for 10 sec with no ramp. It was cured at 80 °C for 5 min, and then under vacuum at 175 °C for 15 min. The core layer was then spin-coated and cured using the same parameters as the bottom cladding layer. Before spin-coating the top cladding layer, a low-tack tape was used to mask off one edge of the core layer. The top cladding layer was then spin-coated with the low-tack tape under the same conditions as the other two layers and cured at 80 °C for 5 min. After being removed from the 80 °C oven, the low tack tape was removed and the film finished curing under vacuum at 175 °C for 15 min.

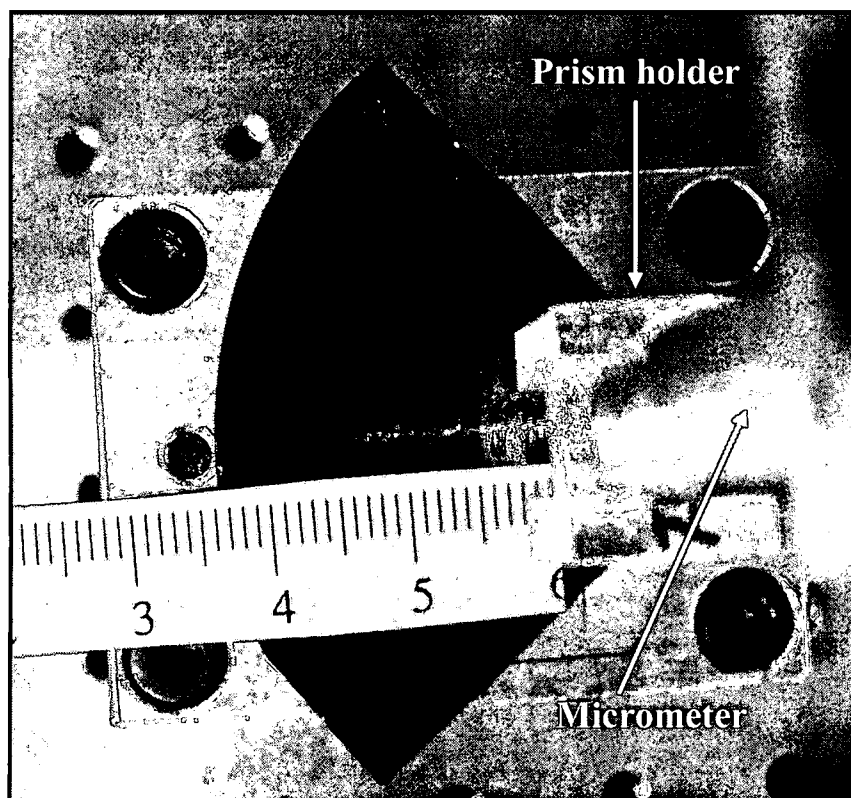


Fig. 7.1. First example of an all-DNA-based three-layer waveguide. Image is a top-view of waveguide. The top cladding layer begins at approximately the 5.8 cm line (notice there is slightly increased scattering at this boundary). The light propagates to the end of the waveguide and can be seen exiting at the 3.6 cm line. [From Reference No. 37]

### 7.1.2. Prism Coupling

As seen in Fig. 7.1, light was successfully prism coupled into the exposed core region of the three-layer DNA-based waveguide. A 690 nm diode laser was used. The exact thicknesses of the individual waveguide layers are unknown, although the total waveguide thickness was measured with a Veeco Dektak profilometer to be  $\sim 10\ \mu\text{m}$ . Based on prior experience with similar solution concentrations and spin-coating conditions, it is estimated that the cladding layers are  $\sim 4\ \mu\text{m}$  thick and the core is  $\sim 2\ \mu\text{m}$  thick. Using these thicknesses and the indices of the materials at 690 nm, the waveguide modes and the corresponding angles of incidence for prism coupling were calculated.

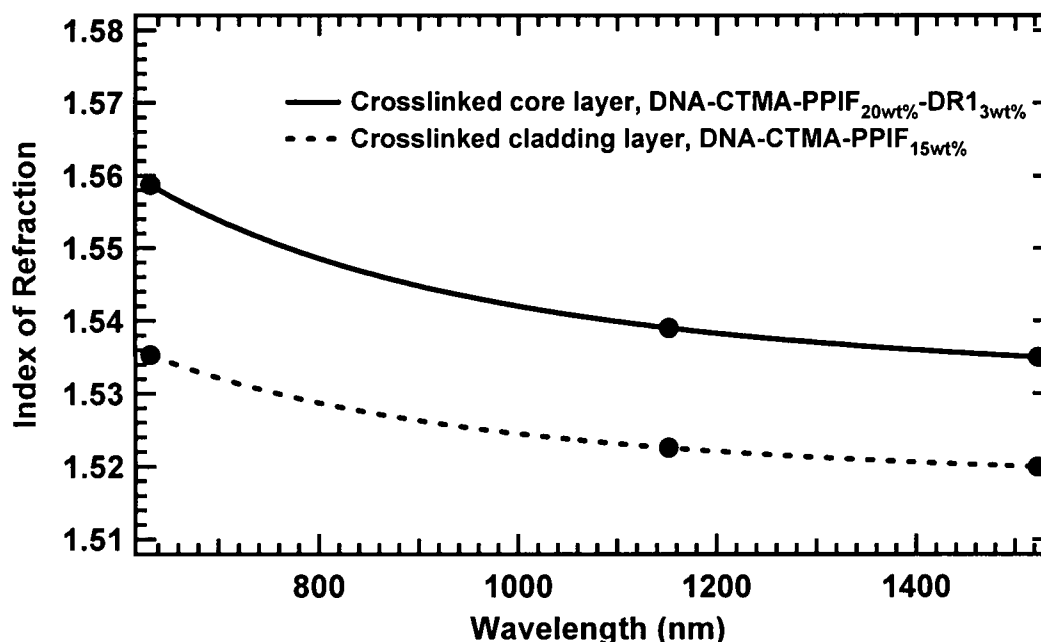


Fig. 7.2. Indices of the core and cladding layers with Cauchy fit for the first all-DNA-based three layer waveguide.

At 690 nm,  $n_{\text{core}} = 1.5544$  and  $n_{\text{clad}} = 1.5325$  (Fig. 7.2), and the index of the SF11 prism  $n_p = 1.7727$ . Assuming the core thickness to be  $2\ \mu\text{m}$ , the TM modes were

calculated from the eigenvalue equation given in Eq. (3.27). Using the specific values for the variables of the three-layer waveguide, this equation became

$$\tan(2K) = \frac{2\sqrt{0.568\pi^2 - K^2}}{K\left(1 - \frac{0.568\pi^2 - K^2}{K^2}\right)} \quad (7.1)$$

To find  $K$ , each side of Eq. (7.1) was plotted as a function of  $K$ . This plot is shown in Fig. 7.3, where two intersections (and therefore two propagating modes) at  $K_1 = 1.0916$  and  $K_2 = 2.0741$  were found. Using the relationship between  $K$  and  $\beta$ , we found

$$\beta = \sqrt{k_o^2 n_f^2 - K^2} \rightarrow \beta_1 = 14.1123 \text{ and } \beta_2 = 14.0017 \quad (7.2)$$

Finally, using the relationship that was developed in Sec. 3.6 between  $\beta$  and the incidence angle  $\theta_i$  on the face of the prism, the incidence angle for each mode was found.

$$\theta_i = \sin^{-1} \left[ n_p \sin \left\{ \sin^{-1} \left( \frac{\beta_m}{k_o n_p} \right) - 45^\circ \right\} \right] \quad (7.3)$$

For  $n_p = 1.7727$  at 690 nm, incidence angles  $\theta_{TE1} = 29.2^\circ$  and  $\theta_{TE2} = 27.6^\circ$  were calculated for the first and second TM modes, respectively. Using the geometry of the prism coupling system, the height  $h$  of the top mirror was positioned so that the incidence angle of the beam on the prism was as close to  $\theta_i$  as possible (Fig. 7.4). A micrometer attached to the top mirror was then used for fine angular tuning to maximize coupling into the waveguide mode.

This calculation was repeated for the TE modes using the TE eigenvalue equation given in Eq. (3.28). The TE modes were calculated as  $\beta_1 = 14.1117$  and  $\beta_2 = 14.0007$  and the corresponding angles of incidence were  $\theta_{TM1} = 29.2^\circ$  and  $\theta_{TM2} = 27.6^\circ$ . It can be seen that the first TM and TE modes are essentially at the same angle (to within one-

hundredth of a degree) and, similarly, the second TM and TE modes are also at the same incidence angle with respect to each other. These results are summarized in Table 7.1.

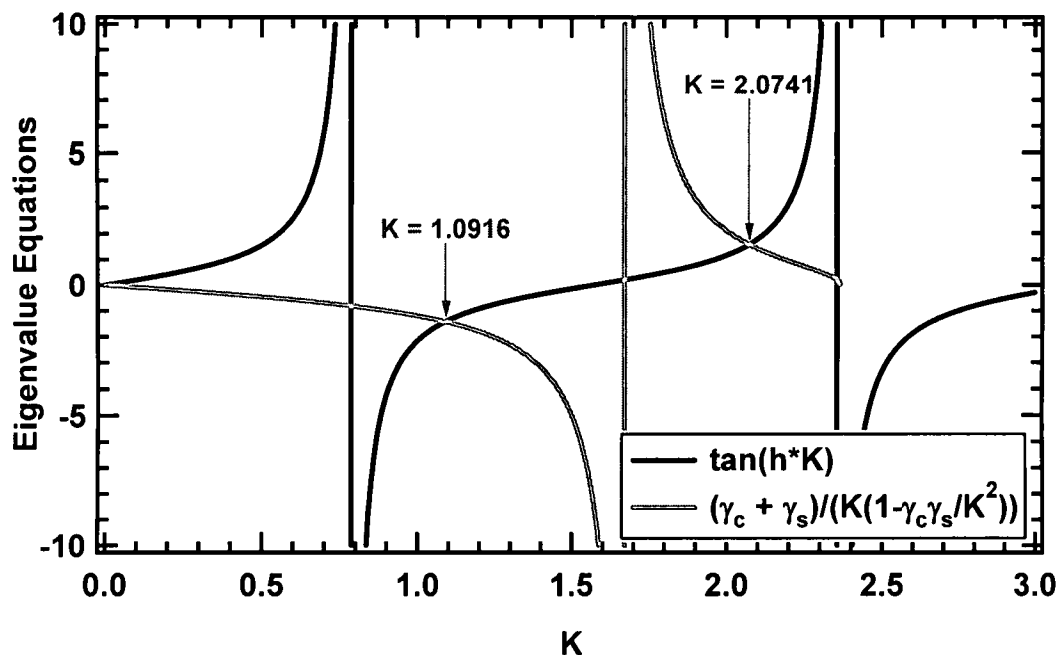


Fig. 7.3. Eigenvalue equation plot for the TE modes of a symmetric three-layer all-DNA-based waveguide.

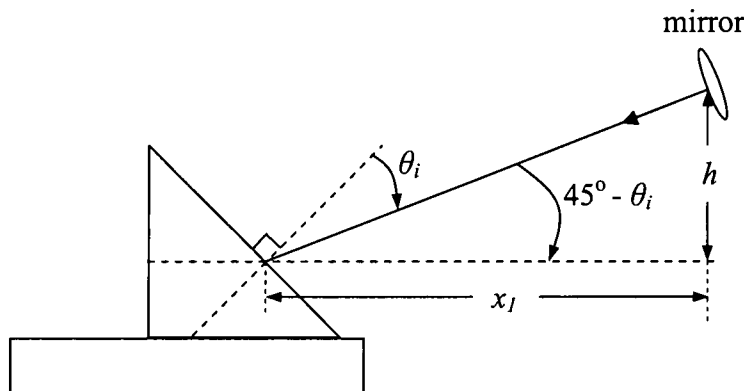


Fig. 7.4. Illustration of relationship between the position of a mirror a horizontal distance  $x_l$  away, with vertical height  $h$  and the angle of incidence  $\theta_i$  required to couple into waveguide mode  $\beta_m$ .  $\tan(45^\circ - \theta_i) = h/x_l$

Table 7.1. Summary of waveguide modes for a 3-layer crosslinked DNA-CTMA waveguide. Calculations were done for  $\lambda = 690$  nm assuming a core thickness of 2  $\mu\text{m}$ . The indices for the core and cladding are  $n_{\text{core}} = 1.5544$  and  $n_{\text{clad}} = 1.5325$  and the prism index is  $n_p = 1.7727$ .

Waveguide Mode	$K$	$\beta$	$\theta_i$ (deg)
TE <sub>1</sub>	1.0916	14.1123	29.1630
TM <sub>1</sub>	1.0995	14.1117	29.1545
TE <sub>2</sub>	2.0741	14.0017	27.6128
TM <sub>2</sub>	2.0804	14.0007	27.5990

## 7.2. All DNA-Based Three-Layer Waveguide Modulator Device Design

After the successful demonstration of an all-DNA-based three-layer waveguide, the development of a modulating device could begin. All of the necessary elements for this device had been demonstrated: an EO coefficient of 2.0 pm/V was achieved for the proposed core layer, the resistivities of the three layers were found to be equal, the waveguide losses were shown to be <1 dB/cm at the communications wavelengths, and the fabrication technique for a three-layer all-DNA-based waveguide had been developed. Although such a device would ultimately be operated at a communications wavelength of either 1300 nm or 1550 nm, a 690 nm diode laser was used for the majority of the work. A 1300 nm and 1550 nm diode laser were also occasionally used. However, these wavelengths provided no clear advantage over 690 nm for the testing configuration (Sec. 7.3), and so the visible 690 nm laser was used for alignment convenience. The waveguide was designed, therefore, with the operating wavelength of 690 nm in mind.

### 7.2.1 Core and Cladding Materials

The core and cladding materials consist of crosslinked DNA-CTMA with the addition of DR1 in the core layer. The indices of the waveguide layers are determined by

the amounts of crosslinker and DR1; increasing the amounts of either of these raises the index. An index difference for the three-layer waveguide of between 0.02 – 0.03 was desired. This was based on BeamProp<sup>106</sup> simulations and on the physical limitations placed on the design. An index difference  $<0.02$  does not have a well-confined mode in the core region, and an index  $>0.03$  requires excessive amounts of PPIF and/or DR1, which introduce unacceptable amounts of scattering and absorption loss. As discussed in Sec. 5.4.2, loss increases with increasing amounts of PPIF. An upper limit of 20 wt% PPIF is imposed due to excessive loss, while 10 to 15 wt% PPIF is ideal. Because the measurements are done at 690 nm, the amount of DR1 is limited to 5 wt% due to absorption. While the amount of DR1 could be increased if the measurements were performed at 1300 or 1550 nm, the EO coefficient goes down at these wavelengths. Thus, the index difference gained by increasing the amount of DR1 at 1300 nm is offset by the loss in the EO coefficient due to the longer wavelength.

The choice of a cladding material was straight-forward. The index of the cladding should have the lowest index possible and the lowest loss possible while being crosslinked. This was achieved by using a cladding layer with 10 wt% PPIF. The core material was chosen based on the above considerations and measurement requirements. It was previously found that no more than 5 wt% DR1 could be used in order to have a beam propagate across a 4 cm long waveguide at 690 nm without visual loss of signal. After fabricating such a waveguide, it was found that an even lower amount was needed in order to prism couple the propagating beam at the output with sufficient power.

Two different core materials (referred to here as *core<sub>1</sub>* and *core<sub>2</sub>*) were identified as ideal with respect to the above considerations, although variations on these were also

tried.  $Core_1$  was DNA-CTMA-PPIF<sub>20</sub>-DR1<sub>3</sub> and  $core_2$  was DNA-CTMA-PPIF<sub>10</sub>-DR1<sub>4</sub>, where the subscripts indicate the amount of the preceding quantity in wt%. Both materials have approximately the same index at 690 nm, and provide an index difference of  $\sim 0.025$  with respect to the cladding material.  $Core_1$  has the advantage of having a lower amount of DR1, and therefore, decreased absorption loss at 690 nm, but has the disadvantage of having increased PPIF and increased scattering loss.  $Core_2$  has the advantage of having decreased PPIF with decreased scattering loss, but has the disadvantage of having increased DR1 and therefore increased absorption loss at 690 nm. However, the increased DR1 in  $core_2$  will be an advantage with respect to the EO coefficient, which is proportional to the chromophore loading. The indices for both the cladding, DNA-CTMA-PPIF<sub>10</sub> and the two proposed core layers, DNA-CTMA-PPIF<sub>20</sub>-DR1<sub>3</sub> and DC-PPIF<sub>10</sub>-DR1<sub>4</sub> are shown in Fig. 7.5.

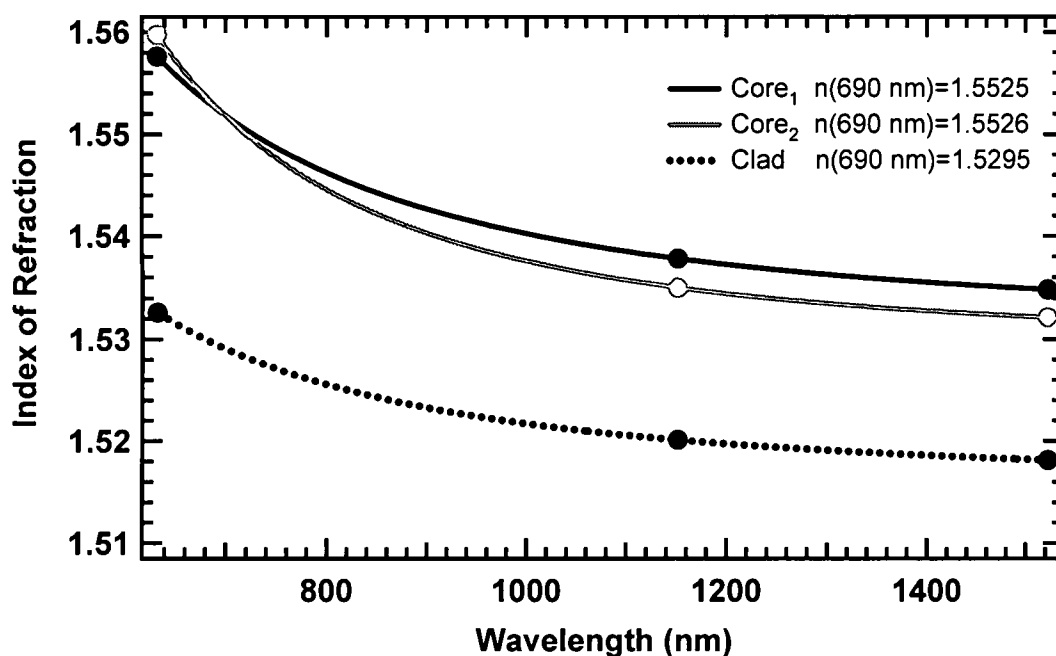


Fig. 7.5. Indices with Cauchy fit of proposed core and cladding materials for 3-layer DNA-based waveguide modulator.  $Core_1$  is DNA-CTMA-PPIF<sub>20</sub>-DR1<sub>3</sub>,  $Core_2$  is DNA-CTMA-PPIF<sub>10</sub>-DR1<sub>4</sub>, and the cladding is DNA-CTMA-PPIF<sub>10</sub>.



### 7.2.2. Physical Dimensions

A schematic of the three-layer waveguide modulator design is shown in Fig. 7.6. The physical parameters that must be determined are the thickness of the bottom cladding layer  $d_{clad1}$ , the thickness of the core  $d_{core}$ , the thickness of the top cladding layer  $d_{clad2}$ , and the length  $L_{clad2}$  that the top cladding layer spans. The length  $L_{clad2}$  determines the propagation length of the waveguide. Because prism coupling was used to couple light into and out of the waveguide, the length determines the closest distance the two prisms can be placed with respect to one another.

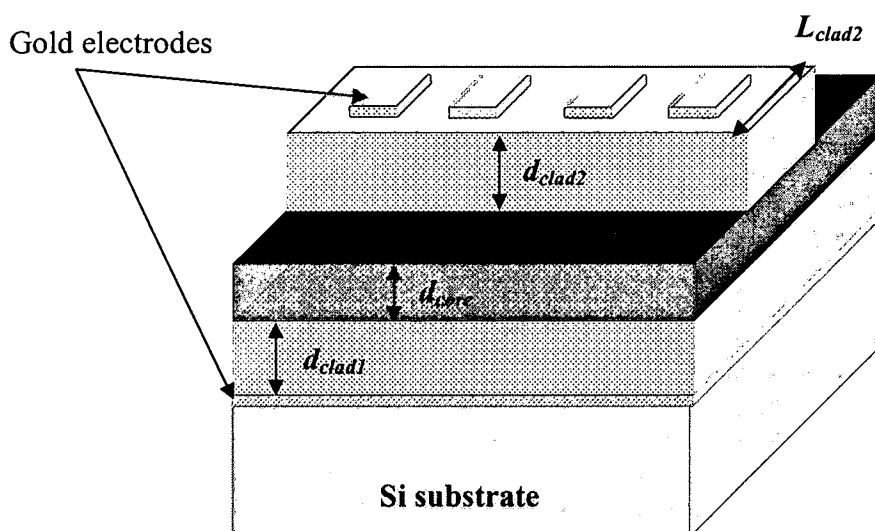


Fig. 7.6. Schematic of 3-layer DNA-based waveguide modulator. Actual substrate is round with a 2" diameter.

The two cladding layers should be thick ( $>4 \mu\text{m}$ ) to avoid the evanescent tail of the waveguide mode reflecting off of the top and bottom gold electrodes. However, the total cladding layer thickness is not unlimited, as the voltage supply used for poling is

limited to 1.1 kV, and the total waveguide thickness must not exceed 22  $\mu\text{m}$  for a poling of field of 50 V/ $\mu\text{m}$ . It is also difficult to spin-coat thick layers  $>8 \mu\text{m}$  uniformly. Ideally, a single-mode waveguide is desired, however the inability to exactly predict the thickness of the core made it necessary to fabricate the core layer slightly thicker than this to ensure at least one propagating mode. The primary waveguide design goal was to fabricate a working device. Due to material and time constraints, fabrication of an ideal, single-mode structure was not attempted. However, BeamPROP was used to compare the advantages and disadvantages of waveguides with varied dimensions.<sup>106</sup> These results are presented in Appendix D, although it was not practical to use them for this stage of the waveguide design.

The fundamental mode for the waveguide with an index difference of 0.025 and a core layer thickness of 3.0  $\mu\text{m}$  is shown in Fig. 7.7. This shows that the cladding layers should extend at least to 4 microns to confine 99% of the mode. Experience has shown that this should be even higher to minimize interactions from the electrodes.

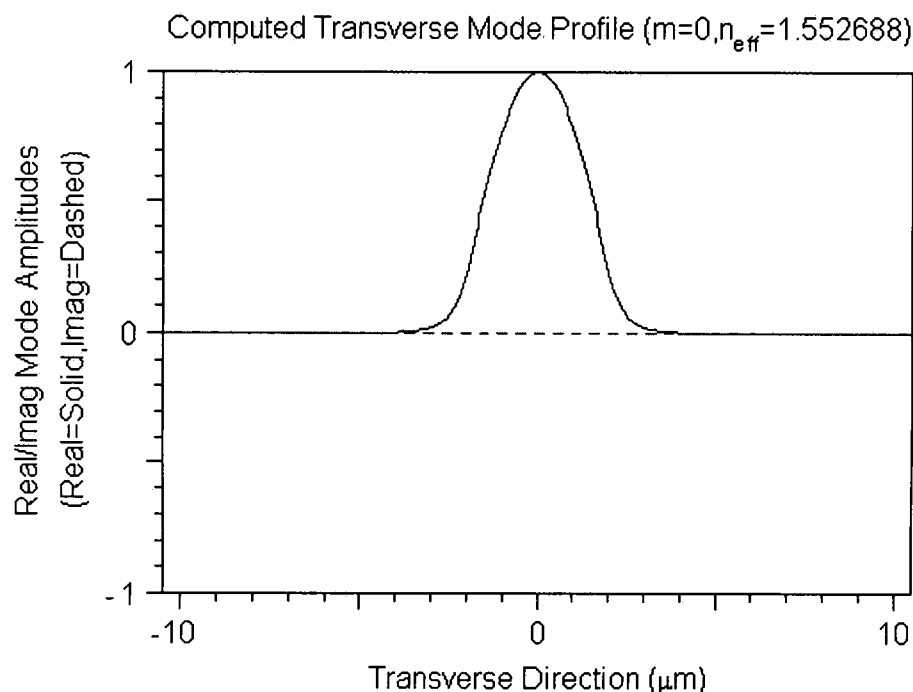


Fig. 7.7. Fundamental mode for a 3-layer symmetric waveguide with  $n_{\text{clad}} = 1.5295$ ,  $n_{\text{core}} = n_{\text{clad}} + 0.025$ ,  $d_{\text{core}} = 3 \mu\text{m}$ ,  $\lambda = 690 \text{ nm}$ . Computed with BeamPROP. [From Reference No. 106]

### 7.2.3. Fabrication

Fabrication is similar to the process described in Sec. 7.1.1. Two different waveguide designs were pursued; one that used  $\text{core}_1$  and one that used  $\text{core}_2$  as the core material. The top and bottom cladding materials were identical for both waveguide designs. The cladding material was prepared from a 110.0 mM solution of 200 kDa DNA-CTMA in butanol with 10 wt% PPIF as described in Sec. 4.4. It was spin-coated on a 2-inch gold-coated Si substrate at 800 rpm for 10 sec with a 5 sec ramp. It was cured at 80 °C for 5 min then vacuum cured at 175 °C for 15 min. A glass cover was

used during curing in the vacuum oven to protect the waveguide surface from contamination by airborne particulates.

Before the core layer was spin-coated, a small edge of the bottom cladding was masked with the low-tack tape. This was to provide a reference plane so that the thickness of the bottom cladding and core layers could be accurately measured. The core layers used were also 110 mM solutions of 200 kDa DNA-CTMA in butanol solutions. *Core<sub>1</sub>* had 20 wt% PPIF and 3 wt% DR1 and *core<sub>2</sub>* had 10 wt% PPIF and 4 wt% DR1. The solutions were prepared as described in Sec. 4.4. The core solutions were spin-coated separately on top of the bottom cladding layers with the low-tack tape mask at 800 rpm for 10 sec with a 5 sec ramp. They were cured at 80 °C for 5 min, after which the low-tack tape was removed and they were further cured for 15 min at 175 °C. The waveguide with *core<sub>2</sub>* was cured an additional 5 min in the 175 °C vacuum oven due to its smaller concentration of crosslinker, which we found requires a longer curing time when containing DR1.

The top cladding layer was the same solution as that used for the bottom cladding layer. The low tack tape was used to mask off both sides of each waveguide, leaving a 1.5 cm channel exposed in the middle of the waveguide. The top cladding layer was spin-coated at 800 rpm for 10 sec with a 5 sec ramp. It was cured at 80 °C for 5 min, after which the low-tack tape was removed and curing was continued under vacuum at 175 °C for 15 min.

After the top cladding layer had fully cured, the low-tack tape was again used to mask off the 1.5 cm channel in the middle of the waveguide. This was to spin-coat a PMMA buffer layer only in the area of the top cladding layer. The necessity of the buffer

layer is discussed in the next section. A 7.5 wt% solution of PMMA in cyclopentanone was prepared for the buffer solution in a similar manner to the DNA-based solutions. It was spin-coated on the top cladding layer at 1000 rpm for 10 sec with no ramp and cured at 80 °C for one hour.

After the waveguide was fully cured, 1000 Å gold-electrodes were sputtered on the three-layer area of the substrate. The electrode masks were made from acetate and were cut using an Xacto-knife. The electrodes were deposited within one hour of fabrication to reduce the risk of contamination to the waveguide surface.

Because a segment of each waveguide layer was masked by low-tack tape before the successive layer was spin-coated on top, an accurate measurement of each layer of the waveguide could be obtained using the Veeco Dektak profilometer. These measurements are listed in Table 7.2.

Although ultimately the ideal design and fabrication for the three-layer waveguide modulator was identified (as described in the previous two sections), several generations of waveguide fabrication were required to hone in on this design. This was due to details that appeared with the poling and testing configurations. As a reference, these waveguides, with their material concentrations and dimensions, are listed in Table 7.2.

Table 7.2. Dimensions of selected three-layer waveguides.

ID	core	clad	$n_{core}$	$n_{clad}$	$L_{clad2}$ (mm)	$d_{clad1}$ ( $\mu\text{m}$ )	$d_{core}$ ( $\mu\text{m}$ )	$d_{clad2}$ ( $\mu\text{m}$ )	$d_{PMMA}$ ( $\mu\text{m}$ )	$d_{total}$ ( $\mu\text{m}$ )
W2	PPIF <sub>10</sub> -DR1 <sub>5</sub>	PPIF <sub>10</sub>	1.5476	1.5292	20	--	--	7.0	0	17.0
W3	PPIF <sub>10</sub> -DR1 <sub>5</sub>	PPIF <sub>10</sub>	1.5476	1.5292	20	--	--	--	0	17.5
W6	PPIF <sub>10</sub> -DR1 <sub>5</sub>	PPIF <sub>10</sub>	1.5476	1.5292	20	3.1	2.9	7.5	0.5	14.0
W10	PPIF <sub>20</sub> -DR1 <sub>3</sub>	PPIF <sub>10</sub>	1.5544	1.5292	15	6.0	3.8	11.7	0.5	22.0
W15	PPIF <sub>10</sub> -DR1 <sub>4</sub>	PPIF <sub>10</sub>	1.5526	1.5292	15	6.5	3.3	6.2	0.5	16.5

### 7.2.4 Poling

The three-layer waveguide stack was poled using techniques similar to those described in Sec. 6.1. A glass slide was placed between the hotplate and the Si wafer to electrically insulate the sample from the hotplate and to provide uniform heating of the wafer. One consequence of the design of the three-layer waveguide is that a measure of the EO coefficient cannot be obtained using the Teng and Man technique because the substrate (Si) and electrodes (gold) are not optically transparent. Additionally, the theory of Teng and Man was developed for a single layer film. The theory for a three-layer stack is different and quite complicated to develop. An estimate of the EO coefficient can only be found, therefore, by testing the device modulation.

The first three-layer waveguides fabricated did not have a buffer layer between the top cladding layer and the top gold electrode. Each had a total thickness of  $\sim 17 \mu\text{m}$ . The cladding layers were DNA-CTMA-PPIF<sub>10</sub> and the core layer was DNA-CTMA-PPIF<sub>10</sub>-DR1<sub>5</sub> (they were fabricated before the necessity of reducing the amount of DR1 was realized). The waveguides samples were labeled *W1* – *W4*. The length  $L_{\text{clad2}}$  of the top cladding layer was 2 cm (again, fabrication occurred before the necessity of a shorter length was realized). Before poling, 690 nm light was prism coupled into each waveguide and good transmission of the modes was confirmed. For poling, the *T then V* technique was used and the sample *W3* was soaked at 65 °C for 30 min before the voltage was applied. The poling current was very high for this waveguide when the voltage was applied. For an applied voltage of only 10 V, the current was in the hundreds of nA range, where normally it is less than 1 nA. Considering the thickness of the waveguide, this is equivalent to an applied field strength of  $<1 \text{ V}/\mu\text{m}$ . Compared to single layer

films, this current was 100 times greater for similar poling fields. Two different electrodes on the *W3* sample were shorted during poling with applied field strengths of only 30 V/  $\mu\text{m}$  and 28 V/  $\mu\text{m}$  (poling was sequential and occurred for the second electrode after the first one was shorted). In fact, these specimens did not simply short, but the edges of the electrodes burned away completely, leaving a blackened, destroyed film underneath.

Poling was then attempted with the sample *W2*, for which the poling profile data is shown in Fig. 7.8. A conservative poling field of only 22 V/ $\mu\text{m}$  (370 V applied over 17  $\mu\text{m}$ ) was applied out of concern of destroying the sample. Even this relatively low field produced currents upwards of 9  $\mu\text{A}$ . The film was held at this voltage for 17 min before cooling.

The high poling currents and the destruction of the film and electrode under a modest field for the three-layer waveguides were unexpected. We believe t

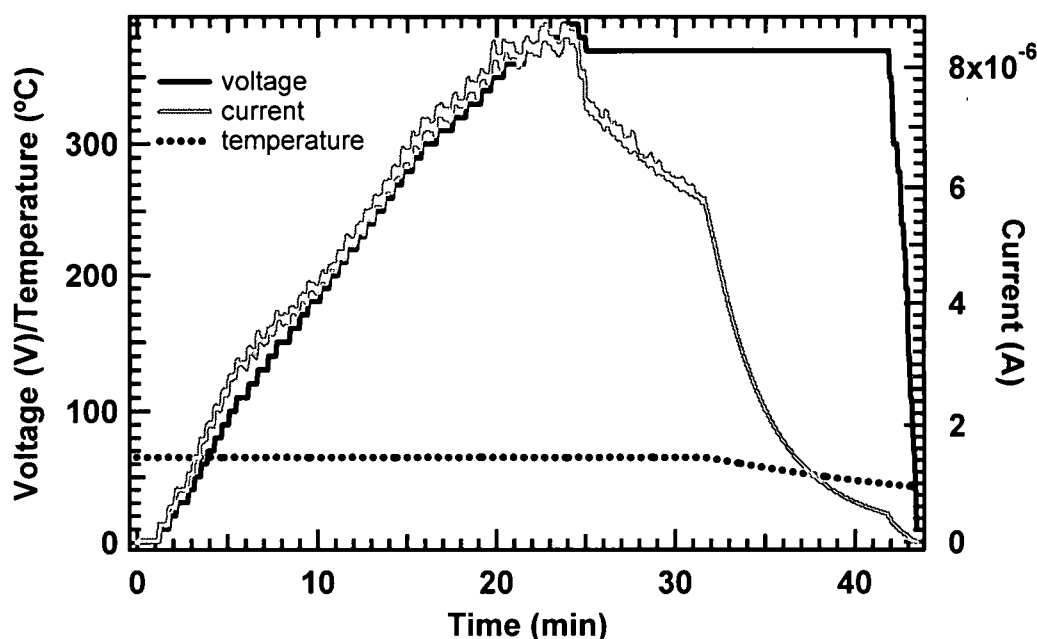


Fig. 7.8. Poling profile data for 3-layer waveguide sample *W2*. Total thickness is 13  $\mu\text{m}$ , no buffer layer.

The poling current for the samples with the PMMA buffer layer was greatly reduced from that without the buffer layer. Sample *W6* had a total thickness of 14  $\mu\text{m}$  and was poled using the *T then V* method. For this sample, a current of only a few nA was observed for a 10 V applied voltage. At the maximum poling voltage of 500 V the current was  $\sim 0.9 \mu\text{A}$ . This voltage corresponds to a field strength of 38 V/ $\mu\text{m}$ . A conservative approach was used with respect to the voltage applied and the dwell time at this voltage out of concern of shorting the sample. The voltage was applied for 20 min then the sample was cooled. Figure 7.9 shows the poling profile data of this sample.



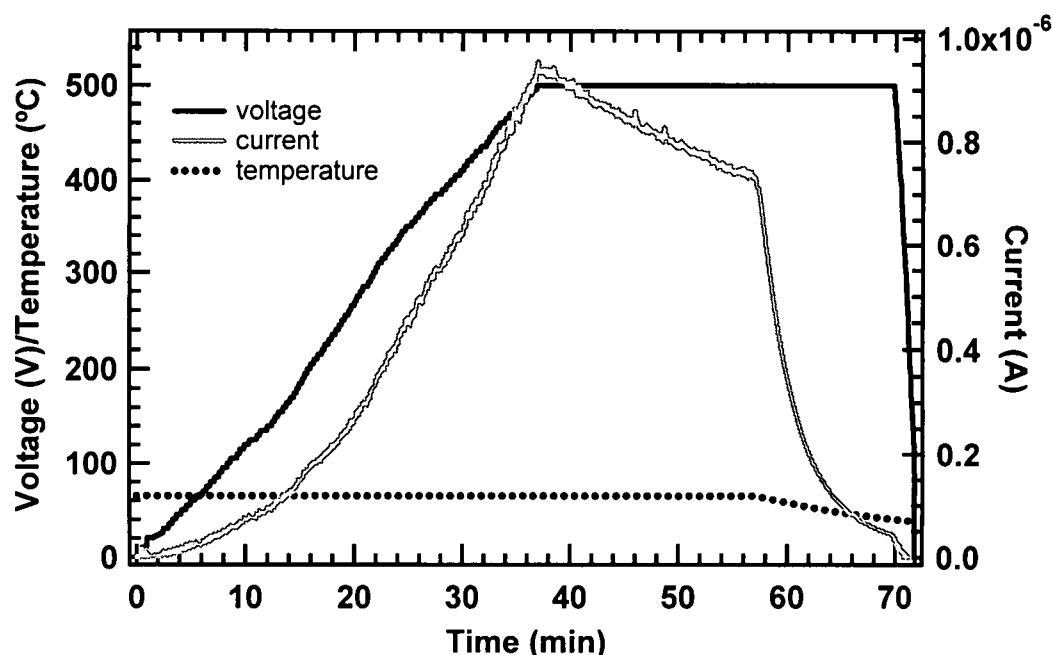


Fig. 7.9. Poling profile data for 3-layer waveguide sample *W6*. Total thickness is 14  $\mu\text{m}$ , 0.5  $\mu\text{m}$  PMMA buffer layer.

The sample *W10* was also poled using the *T then V* technique. The poling temperature was 65 °C and the total field applied was 32 V/ $\mu\text{m}$ , which corresponds to 700 V across the total thickness of 22  $\mu\text{m}$ . At the maximum applied voltage, the current was 227 nA. The voltage was applied for 33 min before the sample was cooled. The poling profile data is shown in Fig. 7.10. Comparing these poling conditions to those of previously poled samples, it is estimated that *W10* has an EO coefficient of  $\sim 0.50$  pm/V. For example, sample *XL2* (Sec. 6.3.3) was poled with a field strength of 64 V/ $\mu\text{m}$  at 65 °C with the *T then V* technique, and had an EO coefficient of  $r_{33} = 1.51$  pm/V. The estimate of  $r_{33} = 0.5$  pm/V takes into consideration that *W10* was poled with half of the field strength and that it contains a higher concentration of crosslinker (20 wt% compared to 10 wt%) and a lower concentration of DR1 (3 wt% compared to 5 wt%).

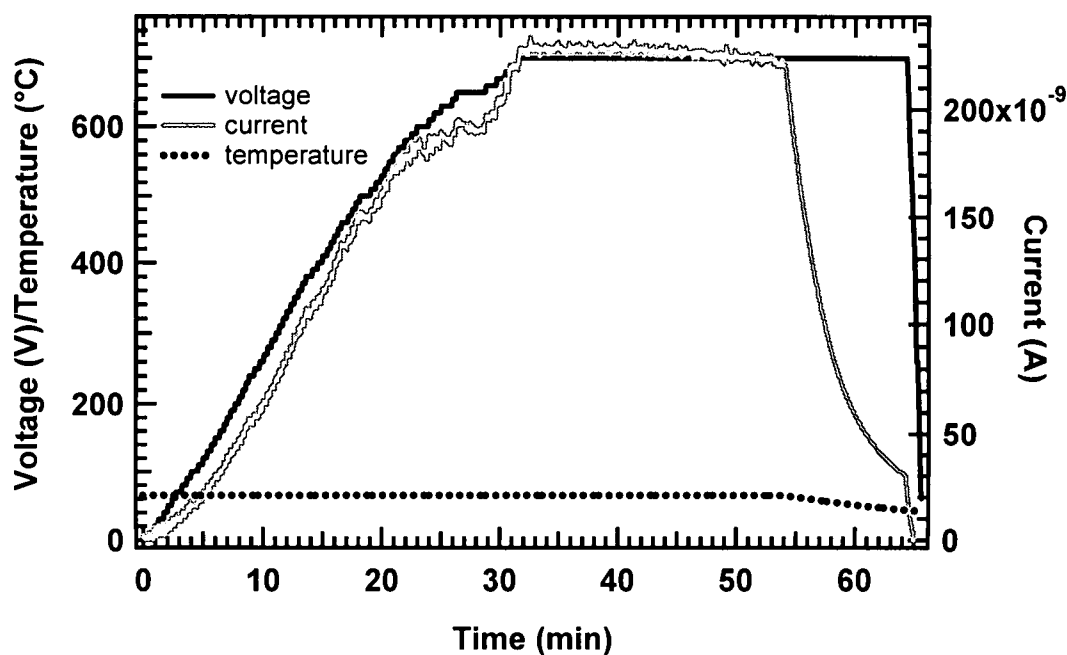


Fig. 7.10. Poling profile data for 3-layer waveguide sample *W10*. Total thickness is 22  $\mu\text{m}$ , 0.5  $\mu\text{m}$  PMMA buffer layer.

### 7.3 Device Testing

Testing the DNA modulator device was more complicated than originally anticipated. There were many details that arose with this material that we have not seen with other polymer devices, such as APC or PMMA. Several testing configurations were tried. Each testing configuration is described below and the advantages and disadvantages are discussed.

#### 7.3.1 Prism Coupling

For all of the following testing configurations, prism coupling was used to couple the light into the waveguide mode. The alternative to prism coupling is end-coupling, which requires sawing and polishing an edge of the waveguide to make a window through which the light can be coupled into the waveguide mode. The fabrication

techniques required to produce such a window are difficult and prism coupling was seen as the most straight-forward approach.

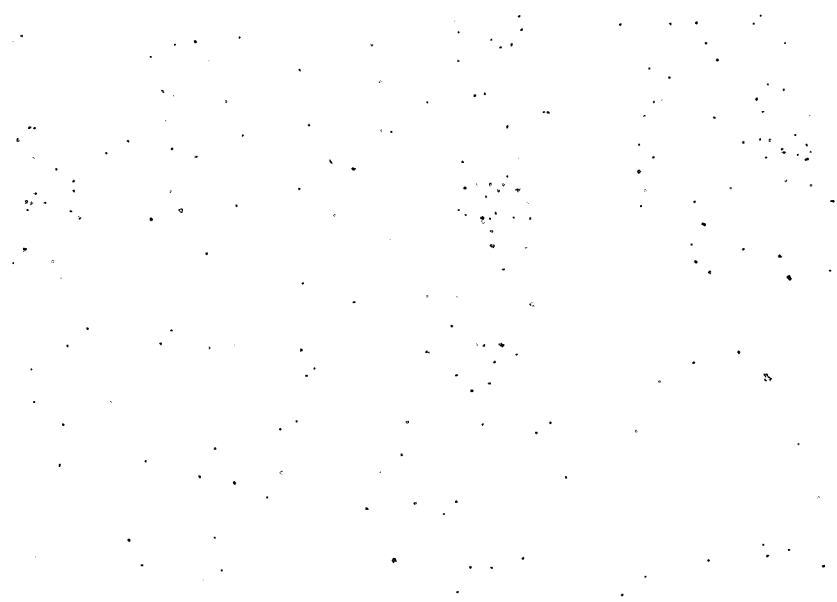
The waveguide modes  $\beta$  for the three-layer waveguide devices initially listed in Table 7.2 were found by using the theory that was outlined in Sec.3.4 and was demonstrated in Sec. 7.1.2. These modes and their corresponding angles of incidence required for prism coupling are summarized in Table 7.3.

Table 7.3. Waveguide modes and angles of incidence for three-layer waveguides.

Waveguide	$\beta_{TE}$	$\theta_{TE}$ (deg)	$\beta_{TM}$	$\theta_{TM}$ (deg)
<i>W6</i>	14.069	28.5	14.069	28.5
	14.002	27.6	14.001	27.6
<i>W10</i>	14.138	29.5	14.138	29.5
	14.089	28.8	14.089	28.8
	14.012	27.8	14.011	27.8
	13.927	26.6	13.97	26.6
<i>W15</i>	14.118	29.2	14.117	29.2
	14.058	28.4	14.057	28.4
	13.968	27.2	13.967	27.2

### 7.3.2 External Mach Zehnder Testing Configuration

The external MZ was described in Sec. 3.2.2. A beam splitter was used to send in two parallel beams through the film. For alignment purposes, a single-layer crosslinked DNA-CTMA film on an SiO<sub>2</sub> substrate was used. Figure 7.11 shows this sample with the two parallel beams prism coupled into and out of the film. After exiting the film, the beams were recombined and an interference pattern was observed. A SB compensator



placed in one of the beams was used to modify the relative phases of the two beams and adjust the interference pattern. This arrangement was successfully demonstrated for the single-layer crosslinked DNA-CTMA film. Light and dark fringes were visibly confirmed, and a maximum-to-minimum signal ratio of about five was obtained on the detector by adjusting the compensator.

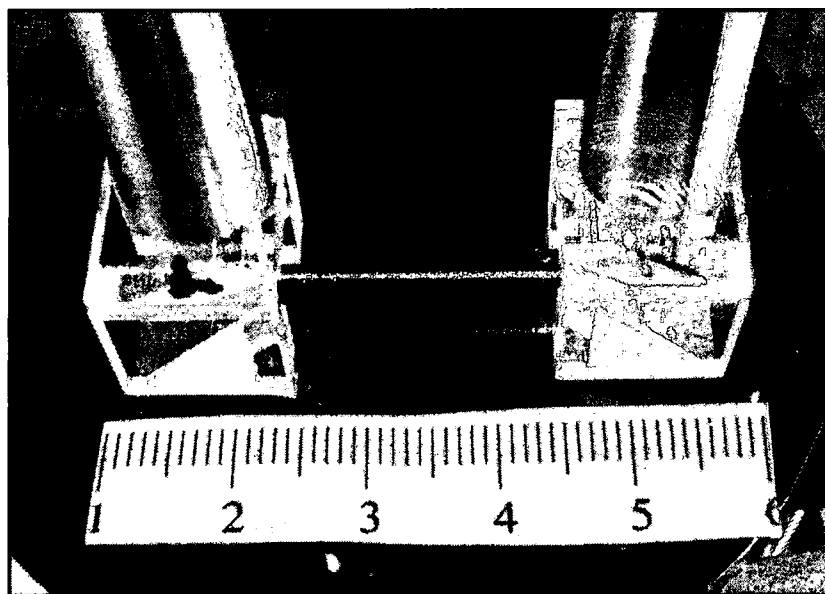


Fig. 7.11. Two beams propagating through single layer DNA film for use in Mach Zehnder external interferometer.

After the external MZ was demonstrated with the single-layer film, measurement of the poled three-layer sample *W10* was attempted. Figure 7.12 shows sample *W10* with one beam propagating in the poled region under the electrode, and the other beam propagating in the unpoled region next to the electrode. It was found that the TM mode was weaker than the TE mode, thus the incident beam was pure TE. Both beams were successfully prism coupled out of the device. Upon exiting, however, the wavefronts

were visually distorted and different for the two beams. The spots that were coupled out showed evidence of structure along the horizontal and vertical directions, and this structure was different for each beam. In the vertical direction, the presence of additional spots is an indication of the presence of additional modes, which couple out of the film at slightly different angles. In the horizontal direction, however, the cause of this structure is most likely due to variations in the waveguide either from thickness variations, scatter from particulates within the films, or a combination of both. Because the wavefronts of the two beams were so dissimilar, constructive and destructive interference of the two could not be achieved. Therefore, it was not possible to use this external MZ arrangement to test the modulation of the DNA-based waveguides.

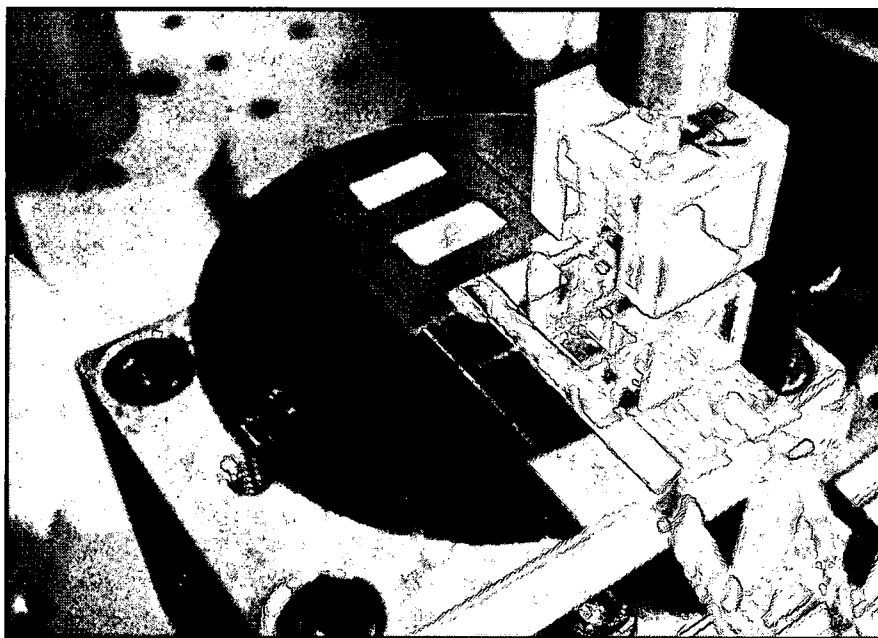


Fig. 7.12. Two beams propagating through three-layer poled DNA-based waveguide for use in Mach Zehnder external interferometer.

### ***7.3.3 Crossed Polarizer Testing Configuration***

The classic, straight-forward testing method of an EO modulator is to place the EO device between a polarizer-analyzer pair oriented at  $45^\circ$  and  $-45^\circ$  and use an incident beam linearly polarized at  $45^\circ$ . For a polymer device, which has different indices in the planes perpendicular and parallel to the poling axis, the addition of a compensator before the analyzer is needed to adjust the polarization of the out-coming light from elliptical back to linear. When no voltage is applied, the compensator is set so that the signal at the detector is at the minimum (preferably null). For a poled material with an EO coefficient, when a voltage is applied across the film the relative phase of the two polarization components of the output light will be changed and a signal will be observed. This method was discussed in detail in Sec. 3.2.3.

Because the laser is horizontally (TE) polarized, a polarization rotator is used in place of a linear polarizer. The rotator is used to achieve the  $45^\circ$  incident polarization required for this testing configuration. A lock-in amplifier, which used a chopper as a reference, was used to better observe changes for weak signals. The chopper was placed after the polarization rotator and was typically operated at  $\sim 400$  Hz. The laser beam was prism-coupled into and out of the device. For this testing configuration, where the incident light was polarized at an angle of  $45^\circ$ , the issue of the mirrors preserving the polarization of the light at high angles of reflection was especially important (Sec. 3.6). To combat the manufacturer's protective dielectric coating of the mirrors, which will not preserve the  $45^\circ$  incident polarization at high angles of incidence, the mirrors were coated with 2000 Å of pure gold.

This testing method was initially tried for the poled sample *W6*. Light was successfully coupled into and out of the waveguide modes for this sample. However, the intensity of the output signal was too faint to be distinguished from noise on the detector. It was determined that a smaller path length and reduced concentration of DR1 were needed to obtain maximum signal output. This led to the design of the next waveguide generations *W9-W12* and *W14-W16*. These specimens had a reduced top cladding layer length  $L_{clad2}$  of 15 mm ( $L_{clad2} = 20$  mm for *W6*). This allowed the input and output prisms to be placed closer together; reducing the path length (and therefore the propagation losses) through the devices. Additionally, smaller concentrations of DR1 were used to minimize absorption losses. Samples *W9-W12* contained 3 wt% DR1 and samples *W14-W16* contained 4 wt% DR1. The amount of crosslinker in samples *W9-W12* was increased to 20 wt% to maintain the index difference of 0.025. Samples *W14-W16* contained 10 wt% PPIF.

This testing configuration was tried for the newly designed waveguide *W10*. Light was successfully coupled into and out of the waveguide modes for this sample. However, with the polarization rotator set for  $45^\circ$  and the analyzer crossed at  $-45^\circ$ , adjusting the compensator did not significantly change the signal on the detector. Consequently, no setting of the compensator could be found to give a minimum signal. By removing the compensator and checking the output signal with the analyzer, it was found that the amplitudes of the TM and TE signals at the output were very different from each other. The TE signal was almost a factor of three times greater than the TM signal. This difference is most likely due to increased absorption and scattering loss of the TM mode compared to the TE mode. Equal TM and TE amplitudes are needed to



minimize the signal. To compensate for this signal difference, the polarization rotator was rotated  $8^\circ$  from  $45^\circ$  toward the TM direction. This passed slightly more TM light than TE light at the input, but resulted in equal TM and TE amplitudes at the output.

With equal TM and TE amplitudes at the output, adjustment of the compensator now showed a maximum and minimum signal, although complete cancellation still could not be achieved. The maximum-to-minimum ratio of the compensator signals was  $\sim 4:1$ . The compensator was set to minimize the signal, and a DC voltage was applied across the device. At  $\sim 100$  V, a signal change was detected. However, when the voltage was removed, it was found that there were no longer equal TM and TE amplitudes. The TM amplitude could not be distinguished from noise levels.

The sample was allowed to sit overnight and the next day it was found that the TM and TE amplitudes were once again approximately equal. We determined that photobleaching of the chromophore due to the high laser power (measured to be 30 mW) and addition of the voltage was most likely the culprit of the unequal TM and TE amplitudes the previous day. The laser power incident on the film was reduced to 4 mW, and again it was found that setting the polarization rotator to  $8^\circ$  from  $45^\circ$  toward TM gave equal TM and TE amplitudes at the output. The compensator was set to a minimum, and a dc voltage was applied across the electrodes. A signal change resulting from the applied voltage was detected on the lock-in.

### **7.3.3.1 Results**

Because the waveguide *W10* is 22  $\mu\text{m}$  thick, we knew that we would not be able to apply the necessary voltage to detect a  $\pi$  signal change (i.e. a maximum signal change). For the waveguide *W10*, we assumed that given its specific poling conditions, it likely

has an EO coefficient of  $\sim 0.5$  pm/V. Given this EO coefficient,  $V_\pi$  can be calculated from Eq. 3.17. In addition to the EO coefficient, the values needed for this calculation are the electrode path length  $L = 0.8$  cm, the core film thickness  $d = 3.8$   $\mu\text{m}$ , core index  $n = 1.5544$ , and the wavelength  $\lambda = 690$  nm. Using this we find that the expected  $V_\pi = 262$  V. This is the voltage required across the core region to induce a  $\pi$  phase change. However, because this is a multilayer waveguide, the total applied voltage across the entire film is much higher. Assuming equal resistivities of the waveguide layers, the total applied voltage needed for a  $V_\pi = 262$  V across  $3.8$   $\mu\text{m}$  of a  $22$   $\mu\text{m}$  thick film would be  $1517$  V,  $V_{total} = V_\pi (22/3.8)$ . Not only is this beyond the capacity of our voltage supply, but we did not want to risk shorting the sample by applying such a high voltage. We limited the total applied voltage to  $\leq 400$  V.

The signal change detected using the crossed-polarizer testing configuration for sample *W10* is shown in Fig. 7.13. The data is fit very nicely with a cosine-squared function. The voltage corresponding to the peak value of this fit is the total applied voltage needed to induce a  $\pi$  phase change, and is seen in Fig. 7.14. This voltage was found to be  $1647$  V, and the corresponding  $V_\pi = 285$  V. This is slightly higher than our predicted value of  $V_\pi = 262$  V, and means that our initial estimate of  $r_{33}$  was high. The calculated  $r_{33}$  from the actual  $V_\pi$  is  $r_{33} = 0.46$  pm/V. Considering the low poling field ( $32$  V/ $\mu\text{m}$ ) and the low concentration of DR1 (3 wt%), the performance of this device behaves as predicted. This is the first example of an all-DNA-based EO waveguide modulator.

For comparison, an unpoled electrode on the same *W10* sample was also tested. No change in signal was detected for this specimen when a dc voltage (up to  $300$  V) was

applied across the electrodes. This confirms that the signal change from the poled *W10* electrode (Fig. 7.13) is an EO effect and not some other voltage-dependent effect such as piezoelectric or electro-absorption.

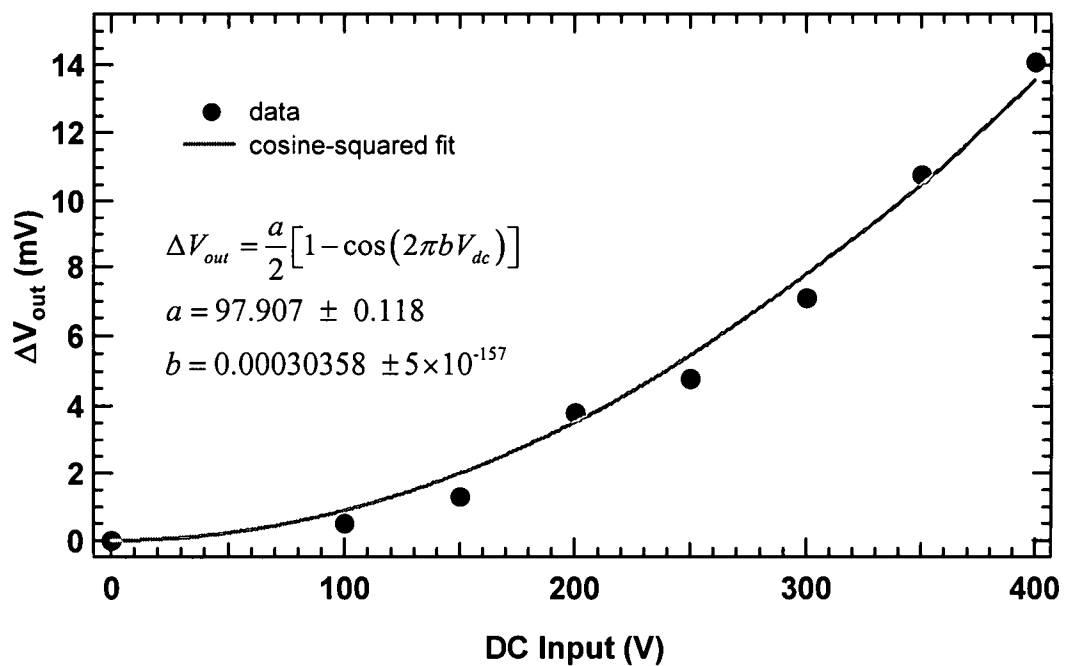


Fig. 7.13. DC modulation of an all-DNA-based EO modulator. A cosine-squared fit is used to find the DC input required for a  $\pi$  phase change.

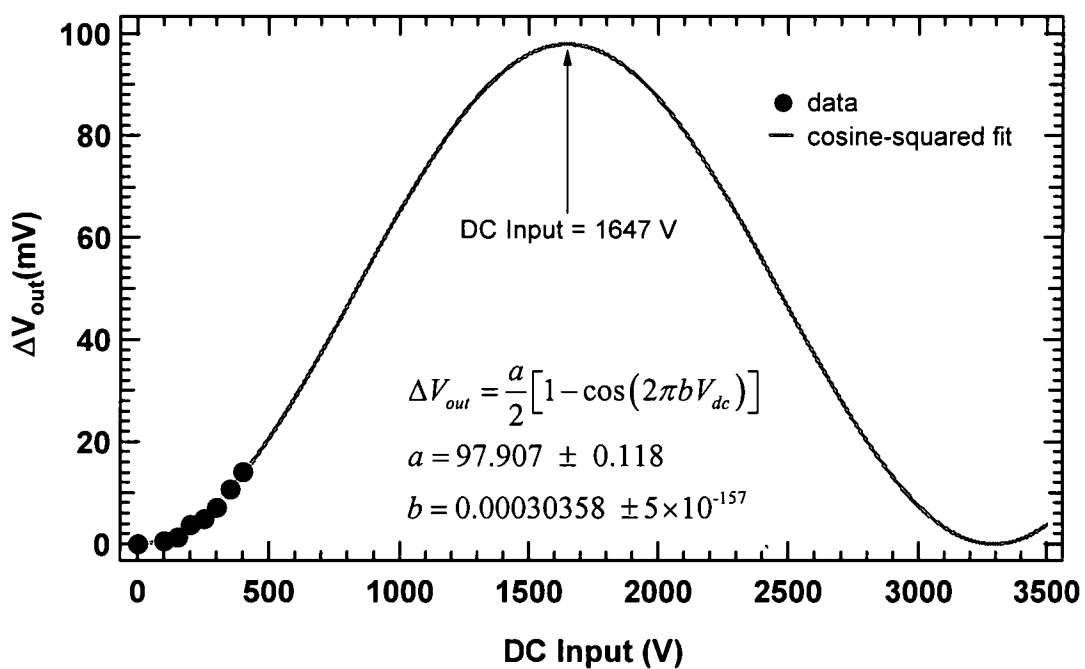


Fig. 7.14. DC modulation of an all-DNA-based EO modulator, extended view. A cosine-squared fit is used to find the DC input required for a  $\pi$  phase change.

### 7.3.4 AC Modulation

Once we confirmed that *W10* was a poled EO waveguide device, we modified the crossed-polarizer testing configuration to test the device for ac signal modulation. These measurements were performed on a different day from the data shown in Figs. 7.13-7.14 with a slightly different system alignment. A compensator was used in front of the polarization rotator to input elliptically polarized light into the device. The major axis of the elliptically polarized light was rotated  $10^\circ$  from the TE direction (to  $80^\circ$  with respect to the vertical) and the minor axis, therefore, was rotated  $10^\circ$  from the TM direction (to  $-10^\circ$  with respect to the vertical). The resulting input was a TE component with three times the magnitude of the TM component. This elliptically polarized light inputs light into both the TE and TM directions. When a voltage is applied to the device, therefore, it will induce a phase change between the two components.

The output analyzer was set to pass the TE component of the output signal only. If a dc-only voltage is applied to the modulator, no effect will be observed on the detector because there will be no change in the amplitude of the TE component due to this applied voltage. The change will only effect the relative phase between the TE and TM components. However, if an ac voltage is superimposed (added to) on the dc voltage, the relative phase change between the TE and TM components due to the dc voltage will be modulated by the ac voltage. In this case, an ac modulation should be evident on the detector.

An ac modulation was detected for this arrangement. A lock-in amplifier was used to detect the ac modulation, with the applied ac voltage serving as the lock-in reference. No chopper was used in this configuration. Figure 7.15 shows the detected ac

signal as a function of the applied ac voltage added to a constant dc voltage of 200 V.

Figure 7.16 shows the detected ac signal as a function of the applied dc voltage with a constant ac voltage of 7.0 V rms. The ac signal modulation was also captured with a LeCroy WaveRunner digital oscilloscope and is shown in Figure 7.17.

This same testing regime was attempted with an unpoled electrode on the same specimen *W10*. No signal modulation was detected with the unpoled electrode.

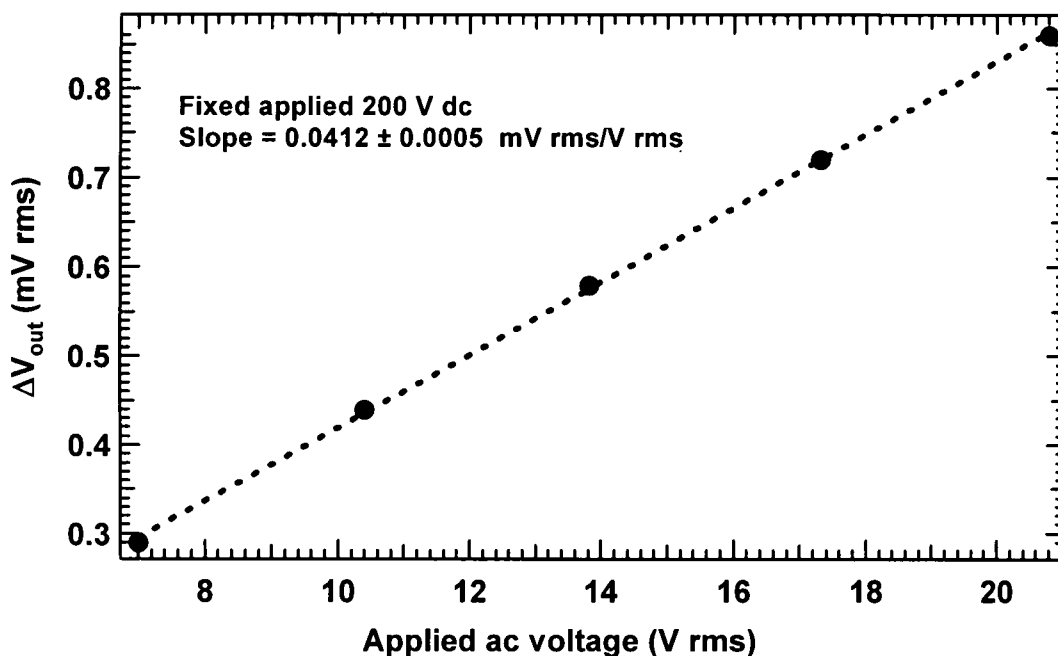


Fig. 7.15. Modulated TE signal for input elliptically polarized light for an applied 200 V dc as a function of the superimposed applied ac voltage.

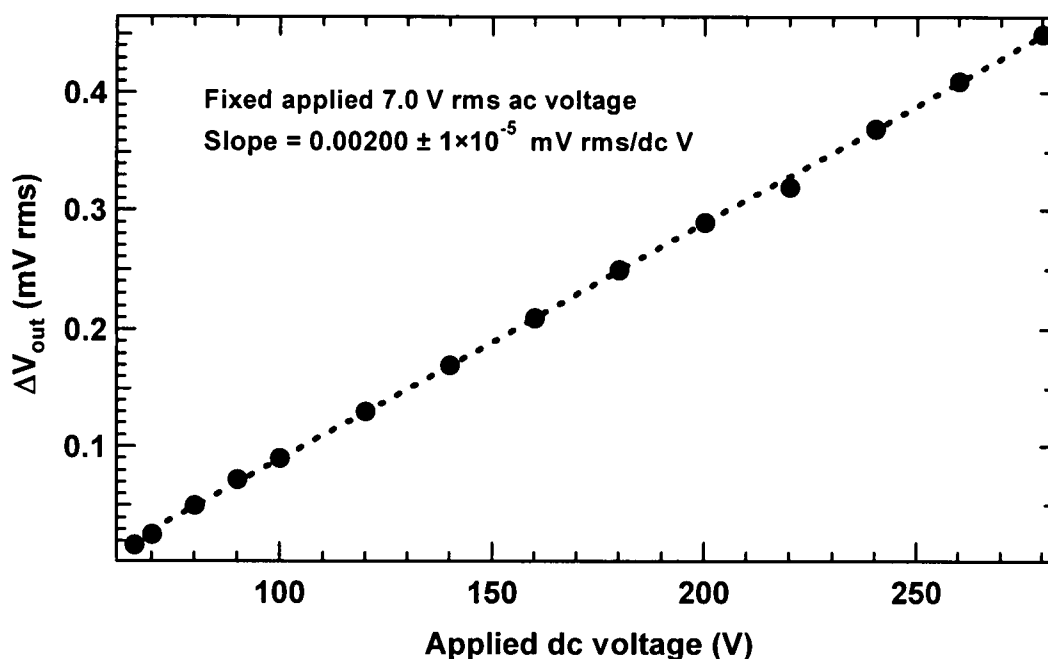


Fig. 7.16. Modulated TE signal for input elliptically polarized light for a fixed applied 7.0 V rms ac voltage as a function of the applied dc voltage.

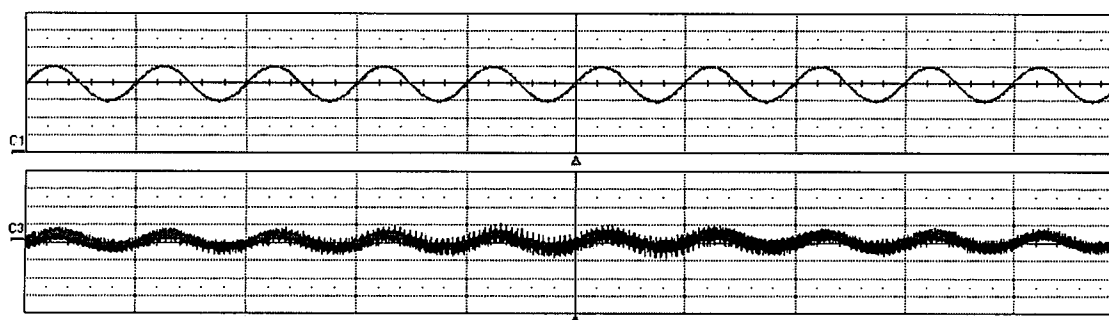


Fig. 7.17. Oscilloscope picture of ac modulation of all-DNA-based EO modulator. The top trace is the applied voltage of 200 V dc plus an ac component of 35 V rms. The modulated signal from the device is shown in the bottom trace with a value of 0.6 mV rms. The channel labels at the left (C1 and C3) indicate the zero voltage positions.

## CHAPTER 8

### SUMMARY AND CONCLUSIONS

#### 8.1 Contributions

DNA was successfully developed into a useful polymer material for application in an all-DNA-based EO waveguide modulator. This research demonstrated several *firsts* with this material: the *first* example of a poled DNA-based chromophore film was demonstrated, the *first* three-layer all-DNA-based waveguide was demonstrated, and the *first* three-layer all-DNA based EO modulating device was demonstrated. Additionally, many unique processing and fabrication techniques were developed specifically for integration of DNA into a photonics device. These include sonication techniques for lowering the molecular weight, recipes for fabricating crosslinked and noncrosslinked DNA-CTMA films of uniform thicknesses, and techniques for three-layer DNA-based waveguide fabrication. Several unique testing configurations were also developed in this research, including a prism-coupling system designed for easy launching of a laser beam into an optical waveguide, and a novel, external Mach Zehnder interferometer for testing an EO waveguide device without the need for 2-D waveguide channel fabrication.



This work has paved the way for future studies of integrating DNA as a new biopolymer for photonics devices. We have shown that DNA is well-suited for such an application and holds the potential to be a low-cost, non-fossil-fuel-based alternative to current polymer devices. We have demonstrated that the DNA-based biopolymer has many of the characteristics desired for such applications: losses  $<1$  dB/cm at the communications wavelengths, TGA evidence of temperature stability up to 200 °C, low dielectric constant  $\epsilon = 4$  for high bandwidth potential, and EO coefficients comparable to other poled polymers with DR1.

## 8.2 Future Work

Although this work has demonstrated that DNA can be successfully integrated into polymer-based devices for photonics applications, it has also brought to light the issue that while purified DNA is technically a polymer, it cannot and should not be treated as an ordinary polymer. Its double helical structure, varying chain lengths, and lack of an unambiguous  $T_g$  make DNA decidedly unique from other polymers.

This work emphasized the importance of consistent processing procedures in a clean, dust-free environment. Several of the problems experienced during this work, such as electrical shorts during poling and wavefront distortion of guided modes, could have been greatly reduced if the fabrication took place exclusively in a Class 1000 cleanroom. Although the facilities used were done in such an environment as much as possible (although the processing room was below Class 1000 cleanroom standards), key elements of the fabrication process such as chemical preparation, high temperature vacuum oven curing, and electrode deposition all took place outside of that environment due to equipment constraints. This exposed the samples to airborne particulates and

other contaminants, which are believed to be the cause of many of the problems experienced. Ideally, a true Class 1000 (or better yet, a Class 100) cleanroom environment should be used for every step of the processing – from chemical mixing and filtering, to spin-coating, to curing, to electrode deposition.

Further research must be done in fully characterizing this material before serious progress in device development can be made. Similar to the characterization studies required of silicon in the 1950-60s that were necessary to produce a semiconductor material that performed consistently, DNA must also be carefully characterized and analyzed from the materials and molecular engineering perspectives and include biochemical studies. Research should include microscopic and nanoscopic structural studies for determining the exact conformal character of the films and the method of intercalation of chromophore dye molecules into DNA. Organic chemistry studies are needed to determine the optimum surfactant and crosslinking chemicals. Additionally, enzymatic methods for precise control of the DNA strand-length should be investigated. The DNA strand-lengths used in this study varied from the mean by  $\pm 50\%$ . We believe that a uniform strand size is necessary for consistent results in device performance. Additionally, based on our poling results, DNA strand lengths of  $<100$  base pairs should be explored for EO coefficient optimization. If a DNA material with consistently uniform strand lengths of  $<100$  base pairs can be developed, then perhaps the behavior of DNA will more closely resemble that of typical polymers.

## APPENDIX A

### CALCULATIONS OF MOLAR CONCENTRATION AND MOLE PERCENT

Many of the calculations in this research are reported in terms of molar concentration and mole percent. While these are common calculations in chemistry, the purpose of this appendix is to refresh those who may not encounter this type of calculation on a daily basis. While weight percent is a convenient unit for everyday laboratory practices, we feel it is not an apposite unit to report in a publication. The units of molar concentration (M or mM) and mole percent (mol%) are more universal and less confusing than weight percent, which doesn't reveal any information in comparing two different types of materials that may have greatly different molecular weights.

For consistency, the molecular weight of DNA in terms of base-pairs (bp), 660 g/mol/bp, is used for all calculations of concentration (mM bp<sup>-1</sup>) and mol%. This is in contrast to using the actual molecular weight based on the lengths of the DNA strands (660g/mol/bp × number of bp = Da). The molecular weight reported in terms of the lengths of the DNA strands has an uncertainty of ± 50% due to the wide distribution of strand lengths from the sonication process. The base-pair molecular weight, however, remains constant regardless of the DNA strand lengths. Additionally, it is necessary to

refer to the molecular weight of the DNA-CTMA complex, for which there are two CTMA molecules for every DNA base pair (one CTMA cation for each DNA anion). Given that the molecular weight of CTMA is 319.75 g/mol, this yields a combined molecular weight of  $660 \text{ g/mol/bp} + 2(319.75 \text{ g/mol}) = 1299.5 \text{ g/mol/bp}$  for DNA-CTMA in terms of DNA base pairs. In all following calculations for molar concentration and mol%, this molecular weight of the DNA-CTMA complex, 1299.5 g/mol/bp, is used.

### A.1 Converting from Weight Percent to Molar Concentration

Molar concentration (M) is defined as moles of material dissolved in one liter of solution.

$$M = \frac{\text{moles of material}}{1 \text{ L of solution}} \quad (\text{A.1})$$

A common calculation is the molar concentration for an amount of DNA-CTMA dissolved in butanol. As mentioned above, the molecular weight of DNA-CTMA in terms of base pairs of DNA is calculated to be 1299.5 g/mol/bp. The density of butanol is 0.81 g/mL. Starting with one gram of DNA-CTMA, let's calculate the amount of butanol needed to have a 12 wt% solution of DNA-CTMA in butanol, meaning that of the total weight of the DNA-CTMA-butanol solution, 12% by weight is DNA-CTMA, and 88% by weight is butanol.

$$\frac{1 \text{ g DNA-CTMA}}{0.12} - 1 \text{ g DNA-CTMA} = 7.33 \text{ g Butanol} \quad (\text{A.2})$$

A 12 wt% solution that contains 1 g of DNA-CTMA would contain 7.33 g Butanol. We can now calculate the molar concentration for this same solution. First, we convert one gram of DNA-CTMA to moles of DNA-CTMA using the molecular weight of 1299.5 g/mol/bp:

$$\frac{1 \text{ g DNA-CTMA}}{1299.5 \text{ g/mol/bp}} = 7.695 \times 10^{-4} \text{ mol/bp} \quad (\text{A.3})$$

Next, we convert 7.33g of butanol to mL of butanol using butanol's density of 0.81 g/mL:

$$\frac{7.33 \text{ g butanol}}{0.81 \text{ g/mL butanol}} \times \frac{1 \text{ L}}{1000 \text{ mL}} = 0.00905 \text{ L butanol} \quad (\text{A.4})$$

Finally, molar concentration can be found by dividing the moles of DNA-CTMA (A.3) by the liters of butanol (A.4) to find

$$\text{Molar concentration} = \frac{7.695 \times 10^{-4} \text{ mol/bp DNA-CTMA}}{0.00905 \text{ L butanol}} = 0.0850 \text{ M} = 85 \text{ mM} \quad (\text{A.5})$$

## A.2. Converting from Weight Percent to Mole Percent

Mole percent is defined as the ratio of moles of material. This is useful when comparing the relative amounts of one type of material to another type of material in the same solution; for example, the amount of chromophore dye relative to the amount of DNA-CTMA. For this example, let's calculate the mole percent of the chromophore dye Disperse Red 1, DR1, ( $F_w = 314.34 \text{ g/mol}$ ) if we want 3 weight percent with respect to one gram of DNA. First, we need to calculate the amount of DR1 so that of the total combined weight of the DR1 and DNA-CTMA, 3% is DR1 and 97% is DNA-CTMA.

$$\frac{1 \text{ g DNA-CTMA}}{0.97} - 1 \text{ g DNA-CTMA} = 0.03093 \text{ g DR1} \quad (\text{A.6})$$

We know the number of moles/bp in one gram of DNA-CTMA from (A.3). Now, using the formula weight of DR1,  $F_w = 314.34 \text{ g/mol}$ , let's calculate the number of moles of DR1 in 0.03093 g of DR1:

$$\frac{0.03093 \text{ g DR1}}{314.34 \text{ g/mol DR1}} = 9.840 \times 10^{-5} \text{ mol DR1} \quad (\text{A.7})$$

Finally, we divide the moles of DR1 (A.7) by the moles of DNA-CTMA (A.3) to find the mole percent of DR1 to DNA-CTMA:

$$\frac{9.840 \times 10^{-5} \text{ mol DR1}}{7.695 \times 10^{-4} \text{ mol/bp DNA-CTMA}} \times 100 = 12.8 \text{ mol\%} \quad (\text{A.8})$$

## APPENDIX B

### MEASURING THE EO COEFFICIENT

As discussed in detail in Sec. 3.3, a modified ellipsometric technique is used to measure the electro-optic coefficient,  $r_{33}$ , of a poled polymer film.<sup>66,67</sup> The poling process induces a polar axis in the polymer film, which essentially is an infinite-fold rotational axis with an infinite number of mirror planes.<sup>46</sup> The molecules are distributed cylindrically about the z-axis and the symmetry is similar to that of a monoclinic system. The expression for  $r_{33}$  was presented in Sec. 3.3 without proof. The purpose of this appendix is to show how the  $r_{33}$  expression is derived. We begin by examining Fig. B.1, a schematic of a beam incident on a polymer film at an angle  $\theta$ .

When a modulating voltage  $V_m$  is applied to the polymer film, the *s*- and *p*-waves will have different path lengths due to the differences in their refractive indices. The *p*-wave will have an additional path length outside of the film of  $2t(\tan \alpha_o - \tan \alpha_p)\sin \theta$  as shown in Fig. B.1. The *s*-wave is only a function of the ordinary index, while the *p*-wave is a function of both the ordinary and extraordinary indices as described later due to

its dependence on the incident angle  $\theta$ . For this reason, the s-wave uses subscripts of “o” while we keep the subscript for the  $p$ -wave as a “p”.

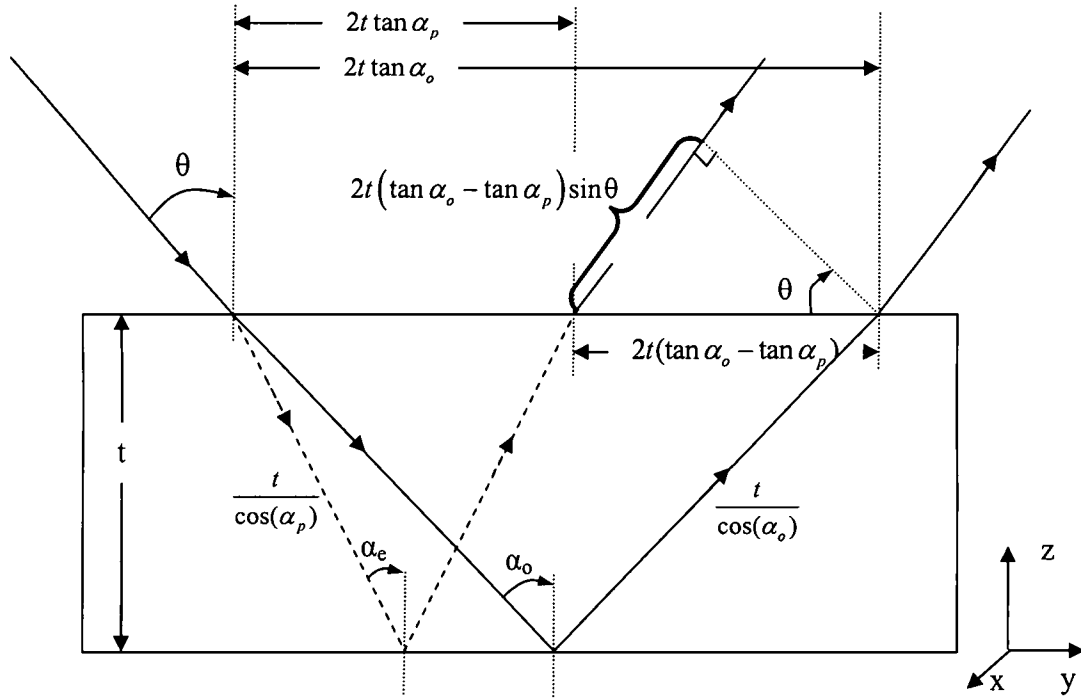


Fig. B.1. Ray paths of  $s$ -wave and  $p$ -wave within the polymer film.

First, note Snell's Law for the two waves

$$\begin{aligned} \sin \theta &= n_o \sin \alpha_o \\ \sin \theta &= n_p \sin \alpha_p \end{aligned} \quad (\text{B.1})$$

The path lengths  $S_s$  and  $S_p$  for the two waves are given as follows (Fig. B.1)

$$\begin{aligned} S_s &= \frac{2t}{\cos \alpha_o} \\ S_p &= \frac{2t}{\cos \alpha_p} + 2t(\tan \alpha_o - \tan \alpha_p) \sin \theta \end{aligned} \quad (\text{B.2})$$

The change in path length between the  $s$ - and  $p$ -waves,  $\partial \psi_{sp}$ , is then



$$\begin{aligned}
\partial\psi_{sp} &= \frac{2\pi}{\lambda} [S_p \partial n_p - S_s \partial n_s] \\
&= \frac{2\pi}{\lambda} \left[ \frac{2t}{\cos \alpha_p} n_p + 2t(\tan \alpha_o - \tan \alpha_p) \sin \theta - \frac{2t}{\cos \alpha_o} n_o \right] \\
&= \frac{4\pi t}{\lambda} \left[ \frac{n_p}{\cos \alpha_p} + \left( \frac{\sin \alpha_o}{\cos \alpha_o} - \frac{\sin \alpha_p}{\cos \alpha_p} \right) \sin \theta - \frac{n_o}{\cos \alpha_o} \right]
\end{aligned} \tag{B.3}$$

Note that the additional path length for the  $p$ -wave,  $2t(\tan \alpha_o - \tan \alpha_p) \sin \theta$ , is in air and therefore is not multiplied by  $n_p$ . Using Snell's Law, Eq. (B.1), we have

$$\begin{aligned}
\partial\psi_{sp} &= \frac{4\pi t}{\lambda} \left[ (n_p - \sin \alpha_p \sin \theta) \frac{1}{\cos \alpha_p} - (n_o - \sin \alpha_o \sin \theta) \frac{1}{\cos \alpha_o} \right] \\
&= \frac{4\pi t}{\lambda} \left[ (n_p - n_p \sin^2 \alpha_p) \frac{1}{\cos \alpha_p} - (n_o - n_o \sin^2 \alpha_o) \frac{1}{\cos \alpha_o} \right] \\
&= \frac{4\pi t}{\lambda} \left[ \frac{n_p}{\cos \alpha_p} (1 - \sin^2 \alpha_p) - \frac{n_o}{\cos \alpha_o} (1 - \sin^2 \alpha_o) \right]
\end{aligned} \tag{B.4}$$

Using trigonometric identities, Eq. (B.4) can be written as

$$\partial\psi_{sp} = \frac{4\pi t}{\lambda} [n_p \cos \alpha_p - n_o \cos \alpha_o] \tag{B.5}$$

The angular dependence of  $n_p$  is given by

$$n_p = \left[ \frac{\sin^2 \alpha_p}{n_e^2} + \frac{\cos^2 \alpha_p}{n_o^2} \right]^{-1} \tag{B.6}$$

From Eq. (B.1) we have

$$\sin \alpha_p = \frac{\sin \theta}{n_p} \tag{B.7}$$

Plugging Eq. (B.7) into Eq. (B.6), we find

$$\begin{aligned}
n_p &= \left[ \frac{\sin^2 \theta}{n_e^2 n_p^2} + \frac{\cos^2 \alpha_p}{n_o^2} \right]^{-\frac{1}{2}} \\
&= \left[ \frac{n_o^2 \sin^2 \theta + n_e^2 n_p^2 \cos^2 \alpha_p}{n_o^2 n_e^2 n_p^2} \right]^{-\frac{1}{2}} \\
&= n_p \left[ \frac{n_o^2 \sin^2 \theta + n_e^2 n_p^2 \cos^2 \alpha_p}{n_o^2 n_e^2} \right]^{-\frac{1}{2}}
\end{aligned} \tag{B.8}$$

We can rearrange this last expression to find

$$\begin{aligned}
1 &= \frac{n_o^2 \sin^2 \theta + n_e^2 n_p^2 \cos^2 \alpha_p}{n_o^2 n_e^2} \\
n_e^2 n_p^2 \cos^2 \alpha_p &= n_o^2 n_e^2 - n_o^2 \sin^2 \theta \\
n_p^2 \cos^2 \alpha_p &= n_o^2 - \frac{n_o^2}{n_e^2} \sin^2 \theta
\end{aligned} \tag{B.9}$$

Taking the square root of this last expression gives

$$n_p \cos \alpha_p = \left( n_o^2 - \frac{n_o^2}{n_e^2} \sin^2 \theta \right)^{\frac{1}{2}} \tag{B.10}$$

Using trigonometric identities, Eq. (B.1) can be rewritten as

$$\begin{aligned}
n_o \sin \alpha_o &= \sin \theta \\
n_o \sqrt{1 - \cos^2 \alpha_o} &= \sin \theta \\
n_o^2 \cos^2 \alpha_o &= n_o^2 - \sin^2 \theta
\end{aligned} \tag{B.11}$$

Taking the square root of this last expression gives

$$n_o \cos \alpha_o = \left( n_o^2 - \sin^2 \theta \right)^{\frac{1}{2}} \tag{B.12}$$

Now, plugging Eq. (B.10) and Eq. (B.12) into Eq. (B.5):

$$\partial\psi_{sp} = \frac{4\pi t}{\lambda} \left[ \left( n_o^2 - \frac{n_o^2}{n_e^2} \sin^2 \theta \right)^{\frac{1}{2}} - \left( n_o^2 - \sin^2 \theta \right)^{-\frac{1}{2}} \right] \quad (\text{B.13})$$

Let  $x = \frac{n_e^2 - n_o^2}{n_e^2} = 1 - \frac{n_o^2}{n_e^2}$  and rewrite Eq. (B.13) as

$$\partial\psi_{sp} = \frac{4\pi t}{\lambda} \left[ \left( n_o^2 - (1-x) \sin^2 \theta \right)^{\frac{1}{2}} - \left( n_o^2 - \sin^2 \theta \right)^{-\frac{1}{2}} \right] \quad (\text{B.14})$$

Doing a Taylor series expansion around  $x$  and noting that

$$\begin{aligned} \partial\psi(0) &= 0 \\ \partial\psi'(0) &= \frac{1}{2} \left[ n_o^2 - \sin^2 \theta \right]^{-\frac{1}{2}} \sin^2 \theta \end{aligned} \quad (\text{B.15})$$

Ignoring higher order terms, the Taylor series expansion gives

$$\partial\psi = \partial\psi(0) + \partial\psi'(0)x + \dots \quad (\text{B.16})$$

Plugging in the expressions in Eq. (B.15) into Eq. (B.16) gives

$$\partial\psi = \frac{4\pi t}{\lambda} \frac{\sin^2 \theta}{2\sqrt{n_o^2 - \sin^2 \theta}} \left( 1 - \frac{n_o^2}{n_e^2} \right) \quad (\text{B.17})$$

When a modulating voltage is applied, there is a change induced in the ordinary and extraordinary refractive indices. These can be written as

$$\begin{aligned} n_o &\rightarrow n_o + \Delta n_o \\ n_e &\rightarrow n_e + \Delta n_e \end{aligned} \quad (\text{B.18})$$

We can therefore rewrite the expression found in Eq. (B.17)

$$\begin{aligned}
1 - \frac{n_o^2}{n_e^2} &= 1 - \frac{(n_o + \Delta n_o)^2}{(n_e + \Delta n_e)^2} \\
&= 1 - \frac{n_o^2 \left(1 + \frac{\Delta n_o}{n_o}\right)^2}{n_e^2 \left(1 + \frac{\Delta n_e}{n_e}\right)^2}
\end{aligned} \tag{B.19}$$

In the weak poling limit, we can make the reasonable approximation that  $n_e \sim n_o \sim n$ .<sup>46</sup>

Using the binomial expansion, Eq. (B.19) can then be rewritten as

$$\begin{aligned}
1 - \frac{n_o^2}{n_e^2} &= 1 - \frac{1 + 2\frac{\Delta n_o}{n}}{1 + 2\frac{\Delta n_e}{n}} \\
&= \frac{1 + 2\frac{\Delta n_e}{n} - 1 - 2\frac{\Delta n_o}{n}}{1 + 2\frac{\Delta n_e}{n}} \\
&= 2\frac{\Delta n_e}{n} - 2\frac{\Delta n_o}{n} \\
&= \frac{2}{n}(\Delta n_e - \Delta n_o)
\end{aligned} \tag{B.20}$$

where we have assumed that  $2\Delta n_e / n \ll 1$ . The changes in the refractive indices can be written in terms of the EO coefficient (Sec. 3.1).

$$\begin{aligned}
\Delta n_e &= \frac{r_{33}n^3V_m}{2t} \\
\Delta n_o &= \frac{r_{13}n^3V_m}{2t}
\end{aligned} \tag{B.21}$$

Using Eq. (B.21) and that  $r_{33} \sim 3r_{13}$  for modest degrees of poling,<sup>46</sup> the expression in Eq. (B.20) can be written

$$1 - \frac{n_o^2}{n_e^2} = \frac{2}{3} \frac{n^2 V_m}{t} r_{33} \tag{B.22}$$

Finally, put the expression in Eq. (B.22) into the expression for  $\partial\psi$ , Eq. (B.17), to find

$$\partial\psi = \frac{4\pi t}{\lambda} \frac{\sin^2 \theta}{2\sqrt{n_o^2 - \sin^2 \theta}} \left[ \frac{2}{3} \frac{n^2 V_m}{t} r_{33} \right] \quad (\text{B.23})$$

As discussed in Sec. 3.3, the measurement is made at the half-intensity points,  $\pi/2$  and  $3\pi/2$ , where the curve is at its most linear region. Therefore, the ratio between the modulated ac voltage  $V_{ac}$  and the midpoint dc voltage  $V_{dc}$  can be approximated by

$$\partial\psi \approx \frac{V_{ac}}{V_{dc}} \quad (\text{B.24})$$

Using this expression in Eq. (B.23) and solving for  $r_{33}$  gives

$$r_{33} = \frac{3\lambda}{4\pi n^2} \frac{\sqrt{n^2 - \sin^2 \theta}}{\sin^2 \theta} \frac{V_{ac}}{V_m V_{dc}} \quad (\text{B.25})$$

As mentioned in Sec. 3.3, the modulation signal  $V_{ac}$  theoretically differs only in sign at the compensator points  $\pi/2$  and  $3\pi/2$  and should be zero at the point  $\pi$ . Realistically, however, this situation only occurs for a transparent film with a purely real EO coefficient.<sup>67</sup> If there is an overlap between the measuring wavelength and the absorption band of the material, the Teng and Man measurements will be dependent on the inflection point used due to the electro-absorption effect.<sup>73</sup> In this case, the absorption effects can essentially be averaged out by averaging the  $V_{ac}$  values from the two phases, allowing a reasonable value for the EO coefficient to be obtained.

The averaging routine to eliminate the electro-absorption effects is dependent on the relative sizes of the EO effect compared to the electro-absorption effect. If the EO effect is dominate, than the ac signal value at  $\pi/2$ ,  $V_{\pi/2}$ , will still have a positive phase and

the value at  $3\pi/2$ ,  $V_{3\pi/2}$ , will still have a negative phase, but the two will be different in amplitude. In this case, the value for  $V_{ac}$  will be

$$V_{ac} = \left| \frac{V_{\pi/2} - V_{3\pi/2}}{2} \right| \quad (\text{B.26})$$

where  $V_{3\pi/2}$  is negative. If the electro-absorption effect is dominate, than the two signals have the same phase (both positive) and different magnitudes. In this case, the expression for  $V_{ac}$  is still given by Eq. (3.20), but now  $V_{3\pi/2}$  is positive. Because the magnitude of the electro-absorption effect depends on the incident intensity, whereas the EO effect depends on the derivative of the incident intensity, this averaging routine effectively cancels out the electro-absorption effect.<sup>73</sup>

Many of the EO measurements in this study are done at 690 nm on films containing the chromophore dye Disperse Red 1 (DR1), which is reddish in color. This averaging routine, therefore, is essential to cancel the electro-absorption effects due to the slight overlap of the absorption bands of this dye with the 690 nm laser. The modified expression for the EO coefficient taking into account Eq. (3.20) can be written as

$$r_{33} = \frac{3\lambda}{4\pi n^2} \frac{\sqrt{n^2 - \sin^2 \theta}}{\sin^2 \theta} \frac{(V_{\pi/2} - V_{3\pi/2})/2}{V_m V_{dc}} \quad (\text{B.27})$$

It is essential to emphasize that this modified expression Eq. (B.27) can be used to remove the electro-absorption effects only if the measurement is far from the absorption band. If the measurement wavelength significantly overlaps the absorption band, the absorption effects will dominate the signal and this averaging routine will not be accurate.<sup>67</sup> Levy *et al.* have shown that this simplified approach breaks down for measurements close to the absorption band.<sup>67</sup>

Another consideration that must be taken into account when making these types of measurements is the effect of interferences arising from partial reflections at the surfaces and interfaces of the specimen (air-substrate and substrate-polymer interfaces). These multiple reflections are due to the interference between forward and backward propagating waves and can produce oscillations in the measured signal, causing inaccuracies in the measurement.<sup>67</sup> Because these fluctuations in the observed signal spread out for longer wavelengths and thinner films, the introduced errors become smaller for measurements on thinner films ( $\sim 2 \mu\text{m}$ ). For a thin film, these spurious reflections can be blocked by using a pinhole placed directly in front of the detector. For thicker electro-optic layers, it may be necessary to reduce the reflections by using a lens to focus the light on the film and another lens to image the correct reflection on the pinhole.<sup>73</sup>

## APPENDIX C

### CHEMICAL SUMMARY

All chemicals used in this work were obtained from Sigma Aldrich<sup>26</sup>, except CTMA, which was purchased from Fisher Scientific.<sup>107</sup> They were used without further purification. This contains a summary of the chemicals used, their pertinent properties, and chemical structures if appropriate.

Chemical Name and Formula	Acronym	Use	Formula Weight (g/mol)	Boiling Point (°C)	Density (g/mL)
<b>Hexadecyltrimethylammonium -chloride</b> $\text{CH}_3(\text{CH}_2)_{15}\text{N}(\text{Cl})(\text{CH}_3)_3$	CTMA	DNA Surfactant	319.75	N/A	N/A
<b>Disperse Red 1</b> $\text{C}_{16}\text{H}_{18}\text{N}_4\text{O}_3$	DR1	Chromophore Dye	314.34	N/A	N/A
<b>Disperse Red 13</b> $\text{NC}_6\text{H}_4\text{N}(\text{C}_2\text{H}_5)\text{CH}_2\text{CH}_2\text{OH}$	DR13	Chromophore Dye	348.79	N/A	N/A
<b>Poly(phenyl isocyanate)-co-formaldehyde</b> $[-\text{C}_6\text{H}_3(\text{NCO})\text{CH}_2-]_N$	PPIF	DNA Crosslinker	400	392	1.2
<b>Butanol</b> $\text{CH}_3(\text{CH}_2)_3\text{OH}$	N/A	DNA Solvent	74.12	116 – 118	0.81
<b>Dioxane</b> $\text{C}_4\text{H}_8\text{O}_2$	N/A	Chromophore Solvent	88.11	100 – 102	1.034



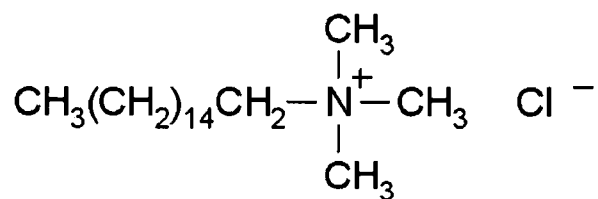


Fig. C.1. Chemical structure of CTMA.

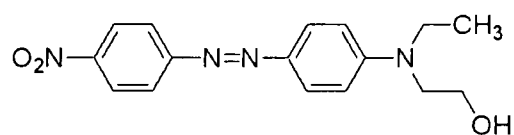


Fig. C.2. Chemical structure of DR1.

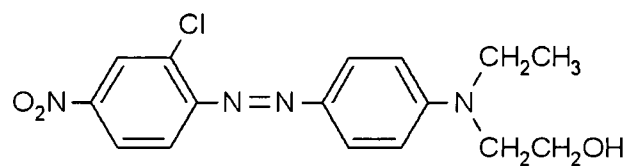


Fig. C.3. Chemical structure of DR13.

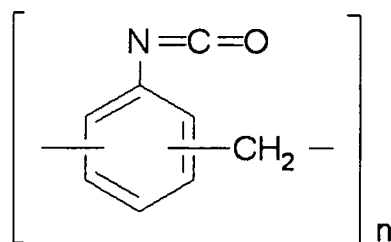


Fig. C. 4. Chemical structure of PPIF.

## APPENDIX D

### WAVEGUIDE DESIGN

As discussed in Chapter 7, the waveguide used in this research was designed to 1) ensure a guided mode could be launched easily and uniformly throughout the waveguide, and 2) to have minimum absorption and scattering losses across the 15 mm path length. The absorption and scattering losses were controlled by reducing the amounts of DR1 PPIF. However the index difference between the core and cladding layers is directly proportional to the amounts of DR1 and PPIF, which controls the confinement of the light in the waveguide structure. Additionally, reducing the amount of DR1 reduces the potential EO coefficient, and thus increases the resulting  $V_{\pi}$ . These considerations must be weighed, therefore, in choosing the appropriate waveguide materials. Many of these design considerations will be alleviated in future work by using a non-absorbing wavelength (for both DNA-CTMA and the chromophore dye), such as 1300 nm or 1500 nm, and using a high-quality chromophore, such as one of the Cheng-Larry-Dalton (CLD) chromophores. For this work, adequate supplies of CLD chromophores could not be obtained and the appropriate equipment for working at near IR wavelengths was not available.

It was found that at 690 nm, the ideal concentration of DR1 in the core layer should be  $\leq 4$  wt% to prevent significant absorption losses. To prevent scattering losses, the concentration of PPIF should be as low as possible. The lowest concentration of PPIF that was found to adequately crosslink the DNA-CTMA layer was 10 wt%. From these observations, two different core materials were tried: *core<sub>1</sub>* with 3 wt% DR1 and 20 wt% PPIF, and *core<sub>2</sub>* with 4 wt% DR1 and 10 wt% PPIF. The increased concentration of PPIF in *core<sub>1</sub>* was used to increase the index difference between the core and cladding materials because of the reduced concentration of DR1. The cladding material used for both designs was a crosslinked DNA-CTMA layer with 10 wt%. This gave the lowest possible scattering losses and lowest cladding layer index of refraction.

A schematic of the waveguide design process is shown in Fig. D.1. In the waveguide design, therefore, the primary consideration was the selection of waveguide materials that ensured that a waveguide mode could be coupled out of the device with a signal distinguishable from the noise level of the detector. Once these materials were identified, the index difference between the core and cladding layers was fixed. For both the *core<sub>1</sub>* and *core<sub>2</sub>* materials this index difference was 0.025 at 690 nm.

The material selection and the resulting fixed index difference imposed limits on the physical design of the waveguide, namely the thickness of the core layer. Although ideally, a single mode waveguide is desired for a modulating device, for an index difference of 0.025 at 690 nm, the conditions for a single mode waveguide are a core thickness  $0.9 \leq d \leq 1.1$   $\mu\text{m}$ . A BeamProp<sup>106</sup> simulation for a single mode waveguide with a core thickness of 1.0  $\mu\text{m}$  at 690 nm with an index difference of 0.025 is shown in Fig. D.2. Although the mode structure is well preserved as it propagates the length of a 4 mm

waveguide, the evanescent tail spreads considerably into the cladding layers. This results in a significant amount of power loss in the core region, only 70% of the initial input power is confined to the core. One of our main considerations for a working device was to get maximum power output through the waveguide. Therefore, a single mode waveguide structure was not feasible. Additionally, the core layer is deposited through spin-coating, which does not permit control of the thickness of the core layer with the precision required for a single mode waveguide. In our experience, we can predict the thickness of a spin-coated film based on solution viscosity and spin parameters to within  $\pm 0.4 \mu\text{m}$ , and thickness variations within a film are typically  $\pm 0.1 \mu\text{m}$ . The thickness window for a single-mode waveguide is only  $0.2 \mu\text{m}$ . It was, therefore, highly unlikely that we could spin a waveguide with the exact thickness required for a single mode waveguide. Additionally, it was more likely that in attempting to fabricate a single mode waveguide, we would undershoot the thickness and have  $d < 0.9 \mu\text{m}$ , which would support no guided modes. Because time and materials were at a premium, we could not afford to risk fabricating a waveguide that would support no guided modes. For these reasons, a single mode waveguide was not attempted.

The mode structure and power confinement for waveguides with core thicknesses of  $2.0 \mu\text{m}$  and  $3.8 \mu\text{m}$  (the actual thickness of *W10*) are shown in Figs. D.3 and D.4. The waveguide with  $d = 2.0 \mu\text{m}$  supports two guided TE modes and has a power confinement (assuming no losses) of 94% compared to the initial power input. The waveguide with  $d = 3.8 \mu\text{m}$  supports 4 guided TE modes and has a power confinement of 99% (also assuming no losses). A better design for *W10* would have been for  $d = 2 - 2.5 \mu\text{m}$  to limit the waveguide to two TE modes. However, based on previous experience this *was*

the thickness range of the core layer for which we had aimed. The thickness data we had collected, however, was for films spin-coated on a plain glass or Si substrate, not on a cladding layer. The cladding layer greatly changes the expected thickness. A DNA-based waveguide with more precise control over the core layer is possible; however, it requires extensive research and data collection for film thicknesses spin-coated on a pre-existing cladding layer with a variety of solution concentrations and spin parameters. This stage of the development of an all-DNA-based waveguide did not warrant such a time-intensive endeavor. The primary objective was to demonstrate that such a device was simply feasible. Now that this has been demonstrated, a more thorough design of the waveguide is appropriate.

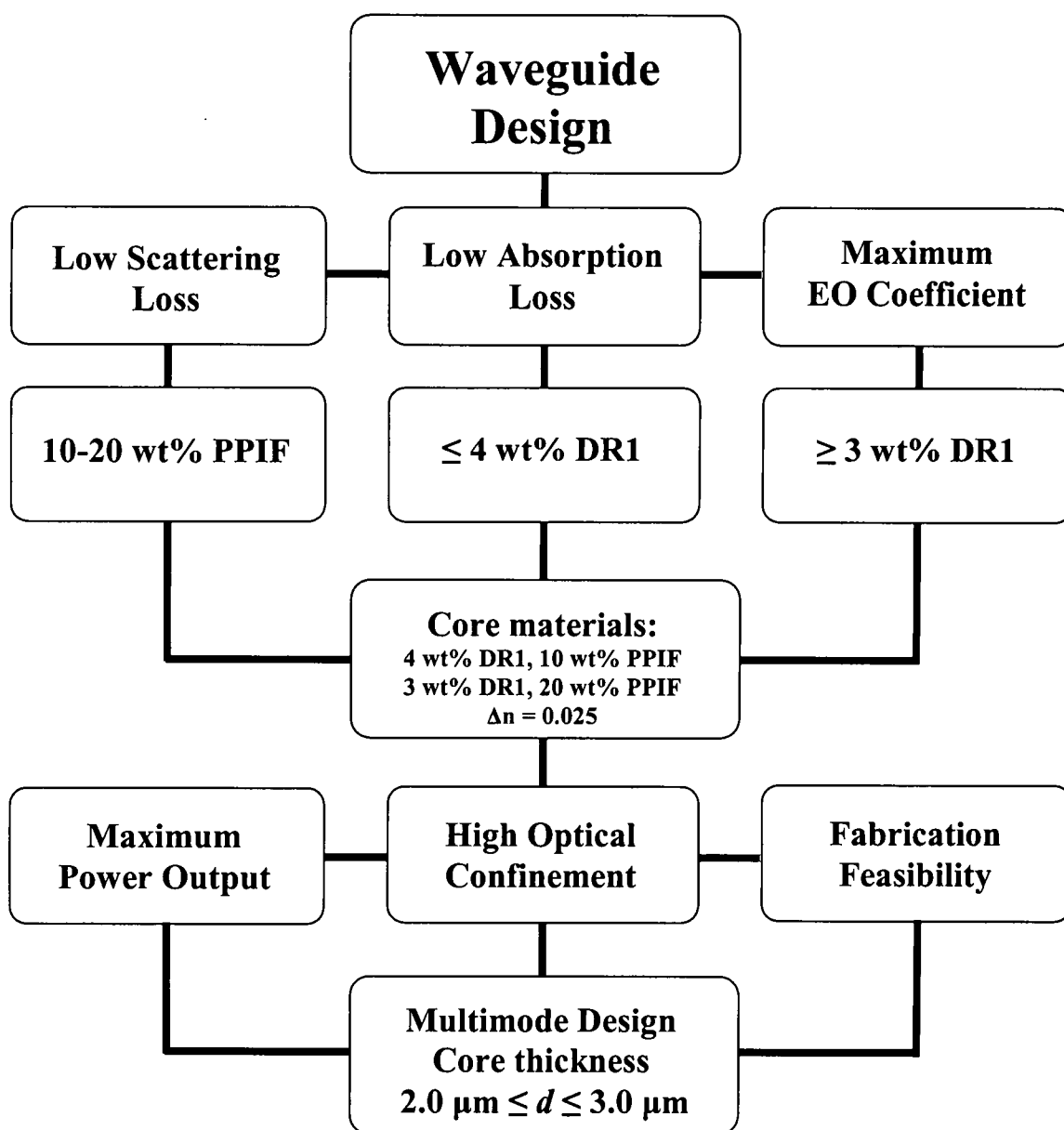


Fig. D.1. Flowchart of waveguide design considerations.

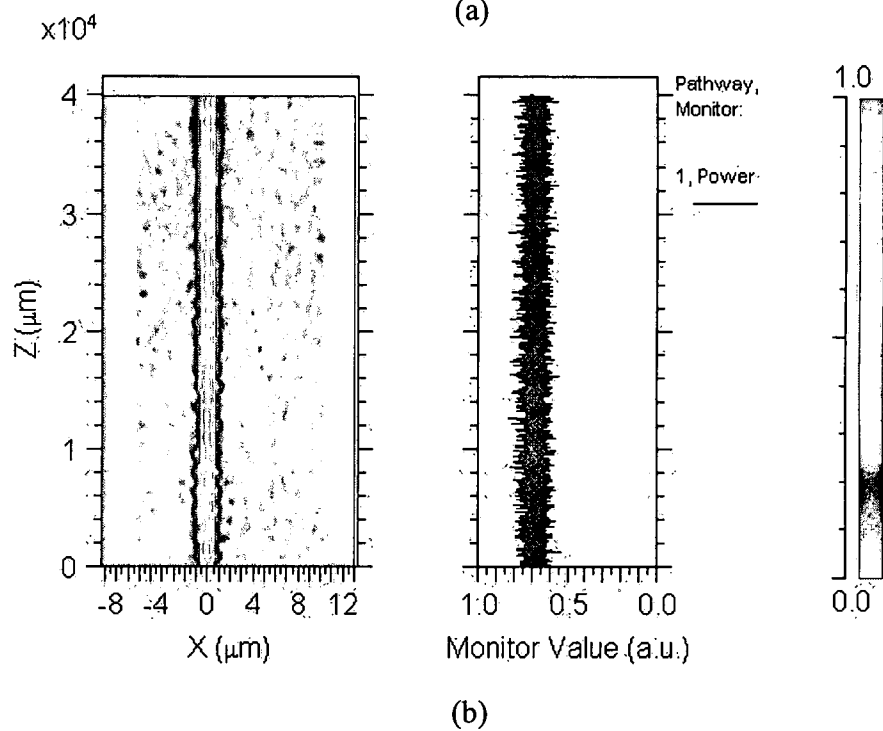
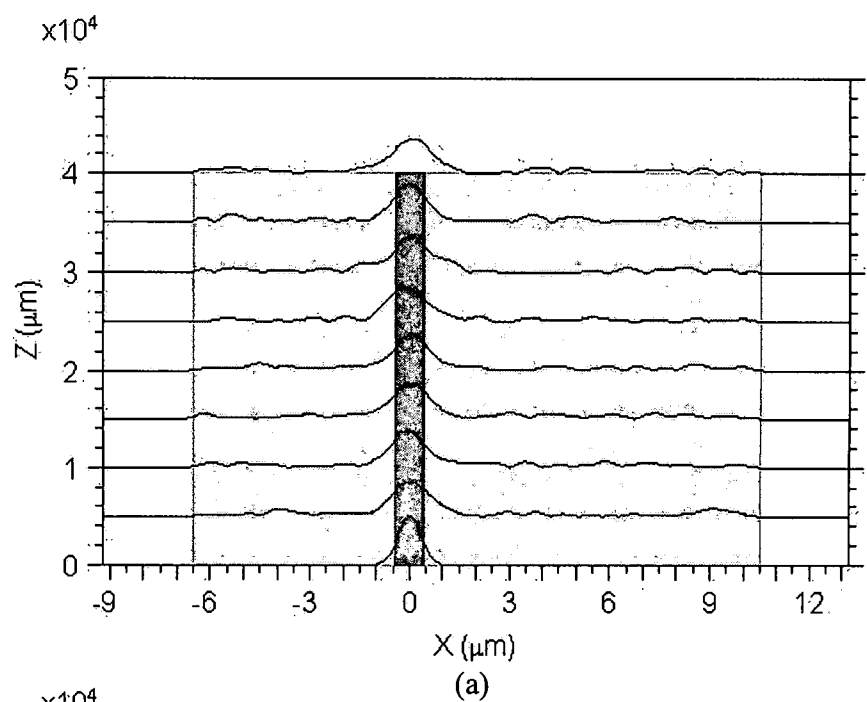


Fig. D.2. (a) Mode propagation and (b) power confinement of a three-layer single-mode waveguide. The core thickness is 1.0  $\mu\text{m}$ , and the index difference is 0.025. [From Reference No. 106]

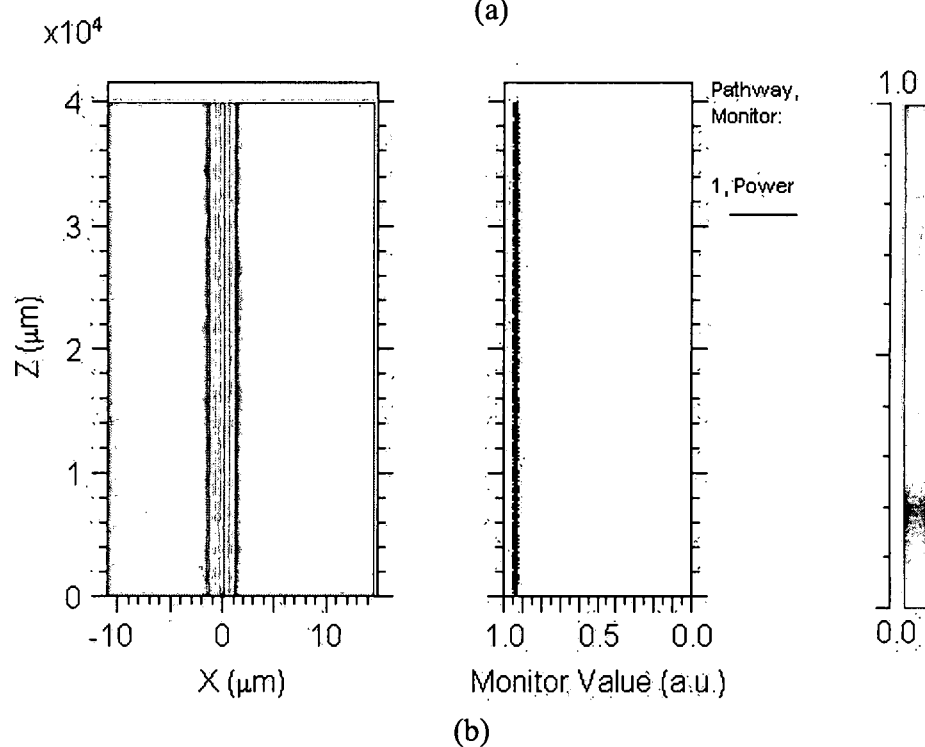
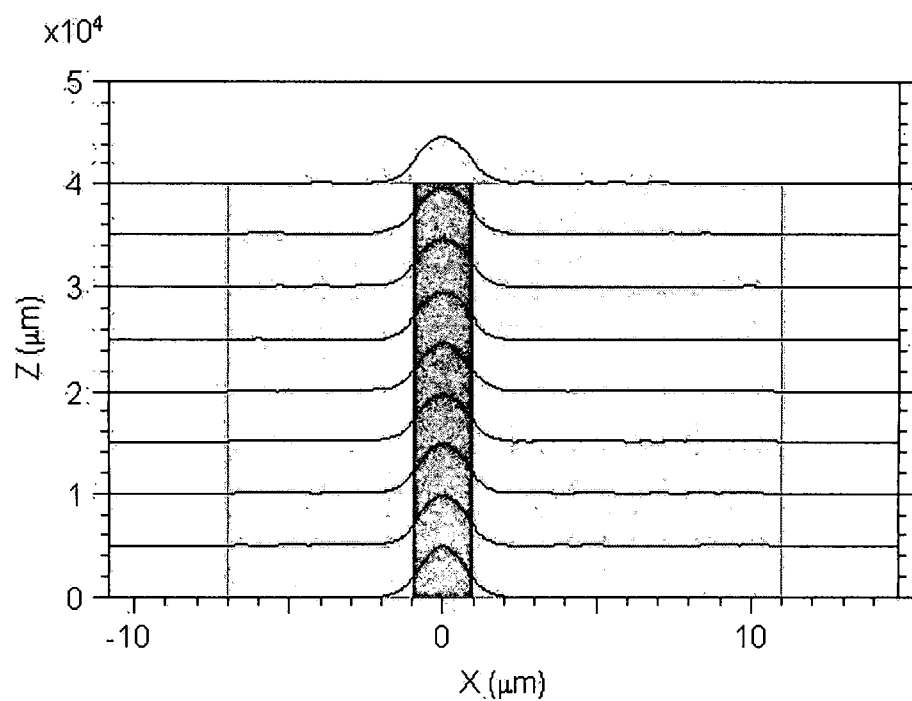


Fig. D.3. (a) Mode propagation and (b) power confinement of a three-layer multi-mode waveguide. The core thickness is  $2.0 \mu\text{m}$ , and the index difference is 0.025. [From Reference No. 106]



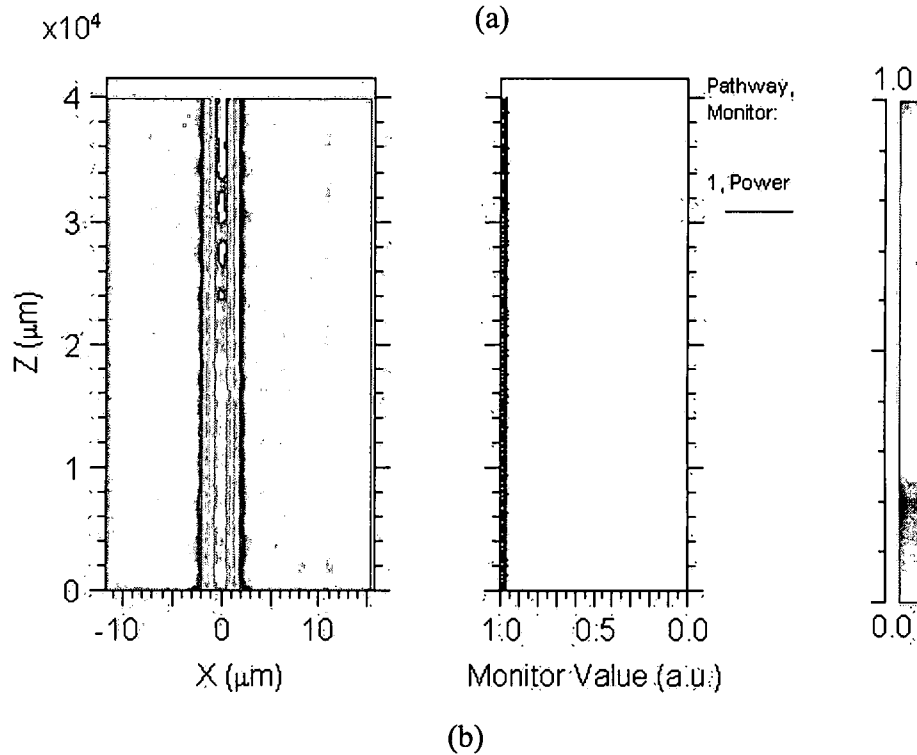
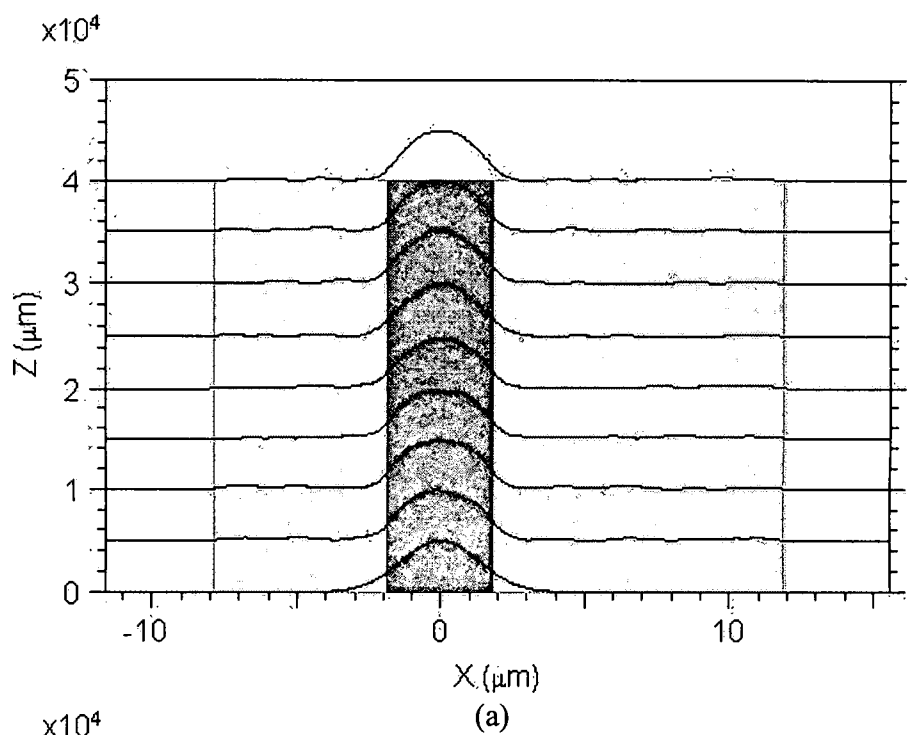


Fig. D.4. (a) Mode propagation and (b) power confinement of a three-layer multi-mode waveguide. The core thickness is  $3.8 \mu\text{m}$ , and the index difference is 0.025. [From Reference No. 106]

**BIBLIOGRAPHY**

1. I. Tomeno and S. Matsumura, "Dielectric constants of LiNbO<sub>3</sub>", *Properties of Lithium Niobate*, London: INSPEC/Institution of Electrical Engineers, pp. 129 – 130, 2002.
2. L. R. Dalton, "Rational design of organic electro-optic materials," *J. Phys: Condens. Matter*, **15**, pp. R897 – R934, 2003.
3. L. R. Dalton, "Realization of sub 1 V polymeric EO modulators through systematic definition of material structure/function relationships," *Synthetic Metals*, **124**, p. 3 – 7, 2001.
4. B. Robinson and L. Dalton, "Defining performance limits for polymeric eo modulators," *Proc. SPIE*, **4279**, pp. 1 – 9, 2001.
5. L.R. Dalton, A.K.Y. Jen, W.H. Steier, B.H. Robinson, S.H. Jang, O. Clot, H.C. Song, Y.H. Kuo, C. Zhang, P. Rabiei, S.W. Ahn, and M.C. Oh, "Organic electro-optic materials: some unique opportunities," *Proc. SPIE*, **5351**, pp. 1-15, 2004.
6. B.H. Robinson and L.R. Dalton, "Monte Carlo statistical mechanical simulations of the competition of intermolecular electrostatic and pooling-field interactions in defining macroscopic electro-optic activity for organic chromophore/polymer materials," *J. Phys. Chem.*, **104**, pp. 4785-4795, 2000.
7. S.S. Lee, A.H. Udupa, H. Erlic, H. Zhang, Y. Chang, C. Zhang, D.H. Chang, D. Bhattacharya, B. Tsap, W.H. Steier, L.R. Dalton, and H.R. Fetterman, "Demonstration of a photonically controlled RF phase shifter," *IEEE Microwave and Guided Wave Letters*, **9**, pp. 357-359, 1999.
8. L. Sun, J.H. Kim, C.H. Jang, J.J. Maki, D. An, Q. Zhou, X. Lu, J.M. Taboada, R.T. Chen, S. Tang, H. Zhang, W.H. Steier, A.S. Ren, and L.R. Dalton, "Beam Deflection with electro-optic polymeric waveguide prism array," *Proc. SPIE*, **3950**, pp. 98-107, 2000.
9. H.H. Kim, L. Sun, C.H. Jang, D. An, J.M. Taboada, Q. Zhou, X. Lu, R.T. Chen, B. Li, X. Han, S. Tang, H. Zhang, W.H. Steier, A.S. Ren, and L.R. Dalton, "Polymeric waveguide beam deflector for electrooptic switching," *Proc. SPIE*, **4279**, 2001.
10. A. Donval, E. Toussaere, R. Hierle, and J. Zyss, "Polymer based polarization insensitive amplitude modulator: conception, technology, and demonstration," *J. Appl. Phys.*, **87**, pp. 3258-3262, 2000.

11. D. An, S. Tang, Z. Shi, L. Sun, J.M. Taboada, Q. Zhou, X. Lu, R.T. Chen, H. Zhang, W.H. Steier, A. Ren, and L.R. Dalton, "1x2 Y-fed directional coupler modulator based on electro-optic polymer," *Proc. SPIE*, **3950**, pp. 90-97, 2000.
12. D. An, Z. Shi, L. Sun, J.M. Taboada, Q. Zhou, X. Lu, R.T. Chen, S. Teng, H. Zhang, W.H. Steier, A. Ren, and L.R. Dalton, "Polymeric electro-optic modulator based on 1x2 Y-fed directional coupler," *Appl. Phys. Lett.*, **76**, pp. 1972-1974, 2000.
13. E. Tomme, P. Daele, R. Baets, G. FL Mohlmann, M. B. J. Diemeer, "Guided wave modulators and switches fabricated in electro-optic polymers," *J. Appl. Phys.*, **69**(9), pp. 6273-6276, 1991.
14. J. Kim, L. Sun, C. Jang, D. An, J. Taboada, Q. Zhou, X. Lu, R. Chen, B. Li, X. Han, S. Tang, H. Zhang, W. Steier, A. Ren, and L.R. Dalton, "Polymeric waveguide beam deflector for eo switching," *Proc. SPIE*, **4279**, pp. 37-44, 2001.
15. M. Lee, H. Katz, C. Erben, D. Gill, P. Gopalan, J. Heber, and D. McGee, "Broadband modulation of light by using an electro-optic polymer," *Science*, **298**, p. 140, 2002.
16. W. Steier, A. Chen, S. Lee, S. Garner, H. Zhang, V. Chuyanov, L. Dalton, F. Wang, A. Ren, C. Zhang, G. Todorova, A. Harper, H. Fetterman, D. Chen, A. Udupa, D. Bhattacharya, and B. Tsap, "Polymer electro-optic devices for integrated optics," *Chem. Phys.*, **245**, pp. 487-506, 1999.
17. L.R. Dalton, "Polymeric electro-optic materials: optimization of electro-optic activity, minimization of optical loss, and fine-tuning of device performance," *Opt. Eng.*, **39**(3), pp. 589-595, 2000.
18. Y. Shi, W. Lin, D.J. Olson, J.H. Bechtel, H. Zhang, W.H. Steier, C. Zhang, and L.R. Dalton, "Electro-optic polymer modulators with 0.8 V half-wave voltage," *Appl. Phys. Lett.*, **77**, pp. 1-3, 2000.
19. Y. Shi, W. Lin, D. Olson, J. Bechtel, H. Zhang, W. Steier, C. Zhang, L.R. Dalton, "Low (Sub-1-Volt) Halfwave Voltage Polymeric Electro-optic Modulators Achieved by Controlling Chromophore Shape," *Science*, **288**, p. 119, 2000.
20. S. Ermer, D. Girton, L.S. Dries, R.E. Taylor, W. Eades, T.E. Van Eck, A.S. Moss, W.W. Anderson, "Low-voltage electro-optic modulation using amorphous polycarbonate host material," *Proc. SPIE*, **3949**, 2000.
21. H. Zhang, M. Oh, A. Szep, W. Steiera, C. Zhang, L.R. Dalton, H. Erlig, Y. Chang, D. Chang, and H. Fetterman, "Push-pull electro-optic polymer

- modulators with low half-wave voltage and low loss at both 1310 and 1550 nm," *Appl. Phys. Lett.*, **78**(20), pp. 3136-3138, 2001.
22. D. Chen, H.R. Fetterman, A. Chen, W.H. Steier, L.R. Dalton, W. Wang, Y. Shi, *Appl. Phys. Lett.*, **70**, p. 3335, 1997.
  23. X. Zheng, A. Sinyukov, M. Leahy-Hoppa, and L. Hayden, "Application of poled electro-optic polymer films in a gap-free, broadband terahertz system," *Proc. SPIE*, **5935**, 59350N, 2005.
  24. J. Hagen, J. Grote, J. Zetts, D. Diggs, R. Nelson, F. Hopkins, P. Yaney, A. Jen, and L.R. Dalton, "Effects of the electric field poling procedure on eo coefficient for guest-host nonlinear optic polymers," *Proc. SPIE*, **5724**, pp. 217-223, 2005.
  25. X. Zhang, X. Lu, L. Wu, and R. Chen, "Contact Poling of the nonlinear optical film for polymer-based electro-optic modulator," *Proc. SPIE*, **4653**, pp. 87-95, 2002.
  26. Sigma-Aldrich, PO Box 14508, St. Louis, MO 63178 USA, 1-800-325-3010, <http://www.sigmaaldrich.com>.
  27. G. Zhang, L. Wang, J. Yoshida, and N. Ogata, "Optical and Optoelectronic Materials Derived from Biopolymer, Deoxyribonucleic Acid (DNA)," *Proc. SPIE*, **4580**, pp. 337 – 346 2001.
  28. G. Zhang, H. Takahashi, L. Wang, J. Yoshida, S. Kobayahi, S. Horinouchi, and N. Ogata, "Nonlinear Optical Materials Derived from Biopolymer (DNA)-Surfactant-Azo Dye Complex," *Proc. SPIE*, **4905**, pp. 375–380, 2002.
  29. J. Grote, E. Heckman, J. Hagen, P. Yaney, G. Subramanyam, S. Clarson, D. Diggs, R. Nelson, J. Zetts, F. Hopkins and Naoya Ogata, "Deoxyribonucleic acid (DNA) based optical materials," *Proc. SPIE*, **5621**, pp. 16-22, 2004.
  30. J. Grote, J. Hagen, J. Zetts, R. Nelson, D. Diggs, M. Stone, P. Yaney, E. Heckman, C. Zhang, W. Steier, A. Jen, L. Dalton, N. Ogata, M. Curley, S. Clarson, and F. Hopkins, "Investigation of Polymers and Marine-Derived DNA in Optoelectronics," *J. Phys. Chem. B*, **108**, pp. 8584-8591, 2004.
  31. J. Grote, N. Ogata, J. Hagen, E. Heckman, M. Curley, P. Yaney, M. Stone, D. Diggs, R. Nelson, J. Zetts, F. Hopkins, L. Dalton, "Deoxyribonucleic Acid (DNA)-Based Nonlinear Optics," *Proc. SPIE*, **5211**, pp. 53-62, 2003.
  32. G. Subramanyam, E. Heckman, J. Grote, F. Hopkins, "Microwave Dielectric Properties of DNA Based Polymers Between 10 and 30 GHz," *IEEE Microwave and Wireless Components Letters*, **15**(4), pp. 232-234, 2005.

33. L. Wang, J. Yoshida, N. Ogata, S. Sasaki, and T. Kajiyama, "Self-Assembled Supramolecular Films Derived from Marine Deoxyribonucleic Acid (DNA)-Cationic Surfactant Complexes: Large-Scale Preparation and Optical and Thermal Properties", *Chemistry of Materials*, **13**(4), pp. 1273-1281, 2001.
34. Y. Kawabe, L. Wang, T. Koyama, S. Horinouchi, and N. Ogata, "Light amplification in dye doped DNA-surfactant complex films," *Proc. SPIE*, **4106**, pp. 369-376, 2000.
35. E. Heckman, P. Yaney, J. Grote, F. Hopkins, "Poling and optical studies of DNA NLO waveguides," *Proc. SPIE*, **5934**, 593408, 2005.
36. E. Heckman, P. Yaney, J. Grote, F. Hopkins, and M. Tomczak, "Development of an All-DNA-Surfactant Electro-Optic Modulator," *Proc. SPIE*, **6117**, 2006.
37. E. Heckman, J. Hagen, P. Yaney, J. Grote, and F. Hopkins, "Processing techniques for deoxyribonucleic acid: Biopolymer for photonics applications," *App. Phys. Lett.*, **87**, 211115, 2005.
38. J. Grote, N. Ogata, D. Diggs, and F. Hopkins, "Deoxyribonucleic acid (DNA) cladding layers for nonlinear optic polymer based electro-optic devices," *Proc. SPIE*, **4991**, pp. 621-625, 2003.
39. J. Hagen, "Investigation of marine derived DNA for use as a cladding layer in electro-optic devices", M.S. Thesis, University of Cincinnati, Cincinnati, Ohio, (2003).
40. J. Hagen, W. Li, J. Grote, and A. Steckl, "Red/blue electroluminescence from europium-doped organic light emitting diodes," *Proc. SPIE*, **6117**, 61170O, 2006.
41. D. Diggs, J. Hagen, Z. Yu, E. Heckman, F. Hopkins, J. Grote, and A. Steckl, "Molecular Binding and Enhanced Photoluminescence of Bromocresol Purple in Marine Derived DNA," *Proc. SPIE*, **5934**, 593407, 2005.
42. P. Yaney, E. Heckman, D. Diggs, J. Grote, and F. Hopkins, "Development of chemical sensors using polymer optical waveguides fabricated with DNA," *Proc. SPIE*, **5724**, pp. 224 – 233, 2005.
43. D. Diggs, J. Grote, A. Davis, C. H. Zhang, J. Zetts, R. Nelson, L. R. Dalton, P. Yaney, F. Hopkins, "Materials Characterization for Nonlinear Optic Polymer Waveguide Modulator Design," *Proc. SPIE*, **4813**, pp. 94 – 102, 2002.
44. S. Bauer, "Poled polymers for sensors and photonic applications," *J. Appl. Phys.*, **80**, pp. 5531 – 5558, 1996.

45. Z. Liu and D. Zhu, "A low loss electro-optic waveguide polymer modulator and its optimization design," *Optical and Quantum Electronics*, **37**, pp. 949 – 963, 2005.
46. P. Prasad and D. Williams, *Introduction to nonlinear optical effects in molecules and polymers*, Wiley: New York, 1991.
47. J. Zetts, "Investigation of poling dynamics for multi-layer polymer electro-optic materials," *Proc. SPIE*, **5554**, pp. 1-14, 2004.
48. L.R. Dalton, *Electrical and Optical Polymer Systems: Fundamentals, Methods, and Applications*, D.L. Wise, T.M. Cooper, J.D. Gresser, D.L. Trantolo, and G.E. Wnek, Eds., World Scientific: Singapore, pp. 609 – 611, 1998.
49. L.R. Dalton, W.H. Steier, B.H. Robinson, C. Zhang, A. Ren, S. Garner, A. Chen, T. Londergan, L. Irwin, B. Carlson, L. Fifield, G. Phelan, C. Kincaid, J. Amend, A. Jen, *J. Chem. Mater.*, **9**, p. 1905, 1999.
50. L.R. Dalton, A.W. Harper, A. Ren, F. Wang, G. Todorova, J. Chen, C. Zhang, M. Lee, *Ind. Chem. Res.*, **38**, p. 8, 1999.
51. D. M. Burland, R. D. Miller, C.A. Walsh, *Chem. Rev.*, **94**, p. 31, 1994.
52. L. R. Dalton, A.W. Harper, R. Ghosn, W.H. Steier, M. Ziari, H. Fetterman, Y. Shi, R.V. Mustacich, A.K.Y. Jen, K.J. Shea, *Chem. Mater.*, **7**, p. 1060, 1995.
53. P. Pretre, U. Meier, U. Stalder, C. Bosshard, P. Gunter, P. Kaatz, C. Weder, P. Neuenschwander, U.W. Suter, *Macromolecules*, **31**, p. 1947, 1998.
54. M. Dobler, C. Weder, O. Ahumada, P. Neuenschwander, U.W Suter, S. Follonier, C. Bosshard, P. Gunter, *Macromolecules*, **31**, p. 7676, 1998.
55. A.K.Y. Jen, Y. Liu, L. Zheng, S. Liu, K.J. Drost, Y. Zhang, L.R. Dalton, *Adv. Mater.*, **11**, p. 452, 1999.
56. H. Ma, A.K.Y. Jen, J. Wu, X. Wu, S. Liu, C.F. Shu, L.R. Dalton, S.R. Marder, S. Thayumanavan, *Chem. Mater.*, **11**, p. 2218, 1999.
57. H. Saadeh, L. Wang, L. Yu, *Macromolecules*, **33**, p. 2218, 2000.
58. M. Watson, P. Ashley, M. Abushagur, "Modeling of optical waveguide poling and thermally stimulated discharge (TSD) charge and current densities for guest/host electro-optic polymers," *IEEE Journal of Quantum Electronics*, **40** (11), pp. 1555 – 1561, 2004.

59. J. Grote, J. Zetts, R. Nelson, F. Hopkins, L. Dalton, C. Zhang, W. Steier, "Effect of Conductivity and Dielectric Constant on the Modulation Voltage for Optoelectronic Devices Based on Nonlinear Optical Polymers," *Optical Engineering*, **40**, pp. 2464 – 2473, 2001.
60. J. Chon and P. Comita, "Laser ablation of nonlinear-optical polymers to define low-loss optical channel waveguides," *Optics Letters*, **19**(22), pp. 1840 – 1842, 1994.
61. G. Martin, S. Ducci, R. Hierle, D. Josse, and J. Zyss, "Quasiphase matched second-harmonic generation from periodic optical randomization of poled polymer channel waveguides," *Appl. Phys. Lett.*, **83**(6), pp. 1086 – 1088, 2003.
62. M. B. J. Diemeer, F. M. M. Suyten, E. S. Trommel, A. McDonach, J. M. Copeland, L. W. Jenneskens, and W. H. G. Horsthuis, "Photoinduced channel waveguide formation in nonlinear optical polymers," *Electronics Letters*, **26**(6), pp. 379 – 380, 1990.
63. A. Chen, V. Chuyanov, S. Garner, W. Steier, J. Chen, Y. Ra, S. Mao, L. Guo, and L. Dalton, "Fast maskless fabrication of electrooptic polymer devices by simultaneous direct laser writing and electric poling of channel waveguides," *Conference Proceedings – LEOS*, **2**, pp. 250 – 251, 1997.
64. P. Kuchel and G. Ralston, *Schaum's Outline of Theory and Problems of Biochemistry*, McGraw-Hill: New York, pp. 198-220, 1998.
65. F. Stephenson, *Calculations in Molecular Biology and Biotechnology*, Academic Press: New York, p. 104, 2003.
66. C. C. Teng, H. T. Man, "Simple Reflection Technique for Measuring the Electro-Optic Coefficient of Poled Polymers," *Applied Physics Letters*, **56**, pp. 1734 – 1736, 1990.
67. Y. Levy, M. Dumont, E. Chastaing, P. Robin, P. A. Chollet, G. Gadret, and F. Kajzar, "Reflection Method for Electro-optical Coefficient Determination in Stratified Thin Film Structures," *Mol. Cryst. Liq. Technol. – Sec. B*, **4**, pp. 1 – 19, 1993.
68. J. Schildkraut, "Determination of the electrooptic coefficient of a poled polymer film," *Applied Optics*, **29**(19), pp. 2839-2842, 1990.
69. F. Pedrotti and L. Pedrotti, *Introduction to Optics*, Prentice Hall: New Jersey, 1993.

70. A. Yariv and P. Yeh, *Optical Waves and Crystals*, Wiley & Sons: New York, 1984.
71. K.D. Singer, M. G. Kuzyk, and J.E. Sohn, *J. Opt. Soc. Am. B*, 4, p. 968, 1987.
72. W. Wang, D. Chen, H. Fetterman, Y. Shi, W. Steier, and L. Dalton, "Traveling wave electro-optic modulator using cross-linked nonlinear optical polymer," *Appl. Phys. Lett.*, **65** (8), pp. 929 – 931, 1994.
73. P. Yaney, E. Heckman, A. Davis, J. Hagen, C. Bartsch, G. Subramanyam, J. Grote, and F. Hopkins, "Characterization of NLO polymer materials for optical waveguide structures," *Proc. SPIE*, **6117**, 61170W- 2006.
74. C. Pollock, *Fundamentals of Optoelectronics*, Irwin: Chicago, 1994.
75. P.W. Atkins, *Physical Chemistry Fourth Ed.*, W.H. Freeman and Company: New York, 1990.
76. R. Hunsperger, *Integrated Optics Fifth Ed.*, Springer: New York, 2002.
77. S. Zamenhof, "Preparation and Assay of Deoxyribonucleic Acid from Animal Tissue," in *Methods in Enzymology*, S. Colowick and N. Kaplan, eds., New York: Academic Press, Inc., pp. 696 – 703, 1957.
78. Schott Glass Catalog, Schott North America, Inc., 400 York Ave, Duryea, PA 18642 USA, [http://www.us.schott.com/optics\\_devices/english/download/](http://www.us.schott.com/optics_devices/english/download/)
79. Sonics and Materials, Inc., "User's Guide 750 Watt Ultrasonic Processor," [http://www.sonicsandmaterials.com/Accessories/accessories\\_8/technical/VC%20505-VC750%20English.pdf](http://www.sonicsandmaterials.com/Accessories/accessories_8/technical/VC%20505-VC750%20English.pdf)
80. "Agarose gel electrophoresis," in *Short Protocols in Molecular Biology Fourth Ed.*, F. Ausubel, R. Brent, R. E. Kingston, D. Moore, J. G. Seidman, J. A. Smith, and K. Struhl, eds., New York: John Wiley & Sons, Inc., pp. 2-14 – 2-16, 1999.
81. Invitrogen, 1Kb DNA ladder. Invitrogen Corporation, 1600 Faraday Avenue, PO Box 6482, Carlsbad, CA 92008 USA, 1-760-603-7200, <http://www.invitrogen.com/downloads/713021539%20ReadyLoad%20Card.pdf>
82. R. H. Page, M.C. Jurich, B. Reck, A. Sen,t R. J. Twieg, J. D. Swalen, G.C. Bjorklund, and C.G. Willson, "Electrochromic and optical waveguide studies of corona-poled electro-optic polymer films," *J. Opt. Soc. Am. B*, 7(7), pp. 1239 – 1250, 1990.



83. *Structure and Dynamics of Biopolymers*, C. Nicolini, ed., Martinus Nijhoff Publishers: Boston, 1987.
84. *Electroanalytical Methods for Biological Materials*, A. Brajter-Toth and J. Chambers, eds., Marcel Dekker, Inc.: New York, 2002.
85. Packaging specifications from the Chitose Institute of Science and Technology, 758-65 Bibi, Chitose, Hokkaido, 066-8655, Japan, 81-123-27-6001.
86. "Nucleic Acid Purity Assessment Using A260/A280 Ratios," Application Note, Bio-Tek Instruments, Inc., [www.biotek.com](http://www.biotek.com)
87. A. Rodger and B. Norden, "DNA-Ligand Interactions," in *Circular Dichroism and Linear Dichroism*, New York: Oxford University Press, 1997, pp. 30 – 31.
88. I. Tinoco, K. Sauer, J. Wang, and J. Puglisi, "Circular Dichroism of Nucleic Acids and Proteins," in *Physical Chemistry: Principles and Applications in Biological Sciences*, Saddle River, NJ: Prentice Hall, Inc., 1995, pp. 585 – 588.
89. Igor Pro by WaveMetrics, Inc. P.O. Box 2088, Lake Oswego, OR 97035 USA, 503-620-3001.
90. R. Speyer, *Thermal Analysis of Materials*, Marcel Dekker, Inc.: New York, 1994.
91. W. Wrasidlo, *Thermal Analysis of Polymers*, Advances in Polymer Science, vol. 13, Springer: New York, 1974.
92. G.W.H. Höhne, W.F. Hemminger, H.-J. Flammersheim, *Differential Scanning Calorimetry Second Ed.*, Springer: New York, 2003.
93. Keithley Application Note 312, "High Resistance Measurements," Keithley Instruments, Inc., <http://www.keithley.com/support>.
94. Keithley Application Note 314, "Volume and Surface Resistivity Measurements of Insulating Materials Using the Model 6517A Electrometer/High Resistance Meter," Keithley Instruments, Inc., <http://www.keithley.com/support>.
95. A. Daire, "Improving the Repeatability of Ultra-High Resistance and Resistivity Measurements," Keithley White Paper, Keithley Instruments, Inc. (2004); <http://www.keithley.com/support>.
96. Z. Kutnjak, G. Lahajnar, Cene Filipiè, R. Podgornik, L. Nordenskiöld, N. Korolev, A. Rupprecht, "Electrical Conduction in Macroscopically Oriented deoxyribonucleic and Hyaluronic Acid Samples," *Physical Review E* 71, 041901 (2005).

R702032616

**The HF Group**

Indiana Plant

T 052546 F 28 00



6/8/2006

97. Z. G. Yu and Xueyu Song, "Variable Range Hopping and Electrical Conductivity along the DNA Double Helix," *Phys. Rev. Letters*, **86**, 6018-6021 (2001).
98. G. Subramanyam, E. Heckman, J. Grote, F. Hopkins, R. Neidhard, and E. Nykiel, *Microwave and Optical Technology Letters*, **46**, p. 278, 2005.
99. C.H. Zhang, G. Todorova, C. Wang, T. Londergan, L.R. Dalton, "Synthesis of new second-order nonlinear optical chromophores: Implementing lessons learned from theory and experiment," *Proc. SPIE*, **4114**, pp. 77-87, 2000.
100. Personal communication. Dr. James Grote, Air Force Research Laboratory, Wright Patterson Air Force Base, Dayton, Ohio, 2005.
101. L. Dalton, "Polymeric electro-optic materials: optimization of electro-optic activity, minimization of optical loss, and fine-tuning of device performance," *Opt. Eng.*, **39**(3), pp. 589 – 595, 2000.
102. See Appendix B.
103. C. Bosshard and P. Gunter, "Electro-optic Effects in Molecular Crystals and Polymers," in *Nonlinear Optics of Organic Molecules and Polymers*, H. Nalwa and S. Miyata, eds., CRC Press: New York, 1997.
104. K. Fox, "Drug-DNA Interaction Protocols," Humana Press: New Jersey, p. 245, 1997.
105. "Enzymatic Manipulation of DNA and RNA," in *Short Protocols in Molecular Biology Fourth Ed.*, F. Ausubel, R. Brent, R. E. Kingston, D. Moore, J. G. Seidman, J. A. Smith, and K. Struhl, eds., New York: John Wiley & Sons, Inc., pp. 3-1 – 3-46, 1999.
106. BeamPROP by RSoft, Inc., 200 Executive Blvd, Ossining, NY 10562, <http://www.rsoftinc.com/beamprop.htm>
107. Fisher Scientific, 1-800-766-7000, <http://www.fishersci.com>.